RESPONSES OF PHOTONIC CRYSTAL FIBRES TO PRESSURE, AXIAL STRAIN AND TEMPERATURE

PANG MENG

Ph.D

The Hong Kong Polytechnic University

2011

The Hong Kong Polytechnic University

Department of Electrical Engineering

RESPONSES OF PHOTONIC CRYSTAL FIBRES TO PRESSURE, AXIAL STRAIN AND TEMPERATURE

PANG MENG

A Thesis Submitted in partial fulfillment of the requirements for the degree of

Doctor of Philosophy

November 2010

CERTIFICATE OF ORIGINALITY

I hereby declare that this thesis is my own work and that, to the best of my knowledge and belief, it reproduces no material previously published or written, nor material that has been accepted for the award of any other degree or diploma, except where due acknowledgement has been made in the text.

_____ (Signed)

Pang Meng (Name of Student)

Abstract

Photonic crystal fibres (PCFs) show different elastic and optical properties from conventional silica fibres because they contain periodic transverse microstructures in their profiles. The responses of PCFs and conventional silica fibres to external measurands are also different, because of the same reason. With these special properties/responses, PCFs have the potential to be widely used in fibre-optic sensors and communication systems. However, to our knowledge, there is no explicit model so far that can simulate the responses of PCFs to axial strain, pressure and temperature.

In this dissertation, the microstructure cladding of PCF is regarded as a honeycomb structure which has inhomogeneous elastic properties. Both Young's modulus and Poisson's ratio of this region are anisotropic, and are the functions of the air-filling ratio of the microstructure cladding. Based on this assumption, three theoretical models for three types of PCFs (solid-core PCF, hollow-core photonic bandgap fibre and hybrid PCF) are constructed. These theoretical models can not only be used to simulate the optical properties/responses of existing PCFs to different measurands, but also be used to predict the performance of PCFs with various fibre designs. Thus when PCFs are used in fibre-optic sensors or devices, these theoretical models are very useful to guide the designs of such sensors or devices.

Using the theoretical models, the responses of PCFs to axial strain, acoustic pressure, temperature and lateral pressure are investigated respectively. The simulation results show that compared with conventional silica fibres, PCFs are predicted to have several novel or improved responses to external measurands, which can be used to

enhance the performance of the fibre sensors or construct new PCF-based devices.

The responses of both solid-core PCF and hollow-core photonic bandgap fibre (PBF) to axial strain are investigated theoretically and experimentally. For the solid-core PCF, the length term of its phase sensitivity to axial strain can be normalized to unit, and the index term is mainly determined by the strain-optic effect of the silica core. The experimental results show that the NL-3.3 fibre (one type of solid-core PCF) has the phase sensitivity of 0.7813±0.006 (ε^{-1}), which agree well with the theoretical prediction. For the hollow-core PBF in which most of light is confined in air, the index term of its phase sensitivity to axial strain is much smaller than the solid-core PCF, which is verified by the experimental results. In experiment, the phase sensitivity of HC-1550-02 fibre (one type of hollow-core PBF) is measured to be 0.9815±0.004 (ε^{-1}), which shows a good agreement with the theoretical prediction of ~0.9797 (ε^{-1}).

The normalized responsivities (NR) of PCFs to acoustic pressure are studied theoretically and experimentally. The simulation results show that: 1) NR of PCF to acoustic pressure is mainly determined by the air-filling ratio of PCF's profile. PCF with a higher percentage of air and lower percentage of silica in its profile is more flexible to acoustic pressure and thus has larger NR; 2) hollow-core PBFs tend to have higher NR than both conventional silica fibres and solid-core PCFs, because the index term of silica-core fibres has opposite sign with the length term, and this negative index term is greatly reduced in a hollow-core PBF in which most of the light is confined in air. In experiment, NR of HC-1550-02 fibre to acoustic pressure is measured to be ~-334.4 (dB re μPa^{-1}), which is about 15 dB higher than conventional fibres. The simulation results show that NR of the hollow-core PBF can be improved further by both decreasing the thickness of its silica outer cladding and

increasing the air-filling ratio of its microstructure inner cladding. Using proper fibre parameters, NR of the hollow-core PBF can reach as high as ~310 (dB re μPa^{-1}), which is about 35 dB higher than conventional fibres. The great improvement of NR is anticipated to have important practical benefits to simplify the sensor design of the fibre hydrophone, and increase the number of sensors that can be interrogated per optical source or the number of sensor channels that can be multiplexed onto a signal fibre.

The simulation shows that the lateral pressure can result in deformation of the hollow-core PBF's air core as well as its air-silica cladding, both of which induce linear birefringence of the hollow-core PBF. Applying pressures laterally to three segments of a HC-1550-02 fibre, a novel hollow-core PBF polarization controller (PC) can be constructed. By varying the magnitudes of the applied pressures in these three segments, the output state of polarization from the hollow-core PBF PC shows a good coverage of all the possible polarization states on the surface of the Poincare sphere, indicating a universal control of the polarization state can be achieved. Compared with former scheme for hollow-core PBF PC which makes use of the inherent birefringence of hollow-core PBF, the new scheme may be applicable to hollow-core PBFs with little or no inherent birefringence. Thus, a hollow-core PBF PC with broader bandwidth may be obtained by using this new scheme.

Hybrid PCF guides light by a novel guiding mechanism, which is a combination of index-guiding and bandgap-guiding. Because the guiding mechanisms of the hybrid PCF are different in two orthogonal directions, high birefringence property is expected. To our knowledge, there is no theoretical model that can simulate the birefringence properties of hybrid PCFs. In this dissertation, a theoretical model for hybrid PCFs is constructed to simulate the birefringence property of hybrid PCFs

and the responses of hybrid fibres' birefringence to axial strain and temperature. Using this theoretical model, the birefringence/responses of hybrid PCFs are predicted, as the functions of their design parameters. In experiment, the birefringence of one type of hybrid PCF and its responses to axial strain and temperature is measured. The experimental results agree well with the simulation results, which give us the confidence to use this theoretical model to guide the design of hybrid PCFs for many special applications.

Acknowledgements

I would like to thank my beloved family as well as my girlfriend, for their supports throughout my student career. It is them who give me the opportunity to finish my master and doctor degrees in the present world which is eager to quick success and instant benefit. I will never forget the unconditional supports of my parents to me in my academic career, and never forget the continuous understanding and support of my girlfriend to me, when I am young and lack of wealth.

I would like to thank my supervisor, Prof. Jin Wei, for his meaningful guidance and great help during the past three years. It is him who makes me know what scientific research is, and how to do excellent research work. Furthermore, he is also a model for me to learn from, as a professional researcher, good group leader, great professor as well as a nice man.

I would like to thank Dr. Xuan Haifeng, Dr. Ju Jian, Dr. Xiao Limin, Dr. Ho Hoi Lut, Dr. Liu Shujing, Dr. Shi Xin, Prof. Zhou Hongpu, Prof. Liao Yanbiao, Associate Prof. Zhang Min and many other research collaborators for their help to my work.

List of Publications

Journal Papers

1. **M. Pang** and W. Jin, "Detection of acoustic pressure with hollow-core photonic bandgap fiber", Opt. Express 17(13), 11088-11097 (2009).
2. **M. Pang**, H. F. Xuan, J. Ju and W. Jin, "Influence of strain and pressure to the effective refractive index of the fundamental mode of hollow-core photonic bandgap fibres", Opt. Express 18(13), 14041-15055 (2010).
3. **M. Pang**, W. Jin, "A hollow-core photonic bandgap fiber polarization controller," Opt. Lett. 36(1), 16-18 (2011).

Conference Papers

4. **M. Pang**, M. Zhang, L. W. Wang, W. Jin and Y. B. Liao, "A digital passive phase demodulation scheme using 3*3 coupler for fiber-optic interferometric sensors", 19th International Conference on Optical Fiber Sensors, Perth, Australia (2008).
5. **M. Pang** and W. Jin, "Phase sensitivity of hollow-core photonic bandgap fiber to acoustic pressure", 20th International Conference on Optical Fiber Sensors, Edinburgh, UK (2009).
6. **M. Pang**, W. Jin, and Y. H. Yang "A hollow-core photonic bandgap fiber polarization controller", 21th International Conference on Optical Fiber Sensors, Ottawa, Canada (2011).
7. 庞盟，靳伟，"基模有效折射率对空心光纤应变/声压传感器相位灵敏度的影响"，第五届光纤传感器发展与产业化论坛，最佳论文奖，中国广州，(2010).

Contents

List of Figures

List of Tables

Chapter 1

Introduction

1.1 Literature Review

1.1.1 Conventional Silica Fibre Sensors and Devices

The optical fibre sensor (OFS) is very diverse and employs many different techniques to sense a wide variety of measurands [1]. OFSs have certain advantages that include immunity to electromagnetic interference, lightweight, small size, high sensitivity, large bandwidth, and ease in implementing multiplexed or distributed sensors [2]. From its origin traceable to the mid 1970s, to today, diverse OFS techniques were developed, such as fibre interferometer, fibre grating, Faraday rotation, fibre scattering reflection, distributed sensing, and the multiplexing technique. OFSs can be used to monitor a wide range of measurands including strain, temperature, pressure, rotation, acoustic emission, humidity, vibration, current/voltage, specified chemicals or gases, and biomedical measurands. There have been excellent review books and articles on OFSs such as Refs. [3-10].

In the optical fibre sensor and communication systems, optical fibre devices (OFDs) are needed to provide specific functions. OFDs can be divided into passive and active OFDs. The passive devices are polarizers, directional couplers, filters and Faraday rotators, while active OFDs require external control or optical power and include modulators, polarization controllers, frequency shifters, and amplifers [10-20].

It is impossible to review all of the OFSs and OFDs in this chapter. In this part of the dissertation, only several types of OFSs and OFDs which are related to the research content of this dissertation are reviewed.

1.1.1.1 Optical Fibre Interferometers

There are several interferometric configurations that are commonly used in OFSs. Perhaps the simplest configuration is the Mach-Zehnder interferometer, shown in Fig. 1.1, where the light propagates in one direction from the source through the interferometer to the detectors. The two arms of the fibre interferometer are typically named the sensing and the reference arms. In many transducers the reference arm is shielded from the environment, and only the sensing arm is subjected to different measurands. The difference between the two paths lengths is measured at the output port of the interferometer.

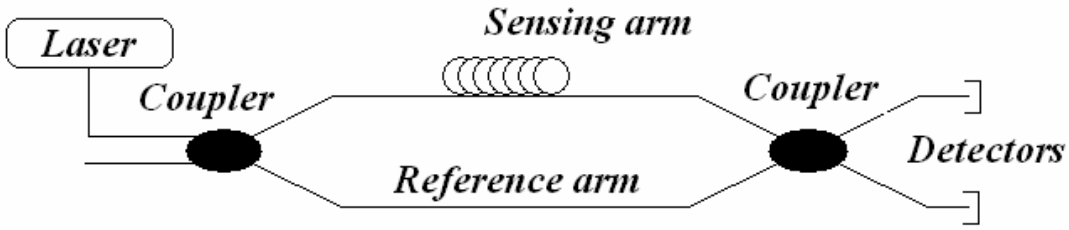

Fig. 1.1 Configuration of the Mach-Zehnder fibre interferometer

One application example of interferometric fibre sensors is the fibre interferometric acoustic sensor, which is widely used for military sonar systems, seismic and sonar systems for oil exploration, and inertial navigation systems [21]. The normalized responsivity (NR), which normalizes the sensor's responsivity by the total optical phase shift in sensing fibre, is used to evaluate different interferometric fibre sensors.

Effectively, this is the same as normalizing by the length of fibre on the transducer. For example, a good fibre-optic hydrophone design might have an NR of -300 dB re $1\mu Pa^{-1}$. If the transducer is interrogated by a laser at λ=1300nm the total optical phase in 1m of fibre is given by $\varphi=2\pi nL/\lambda$=137 dB re rad. Therefore the responsivity of the transducer would also be equivalent to (-300+137=-163) dB re rad μPa^{-1} [21].

Many studies are conducted to improve the NR of the interferometric fibre sensors, because developing an acoustic fibre sensor with a higher NR can effectively increase the number of sensors that can be interrogated per optical source or the number of sensor channels that can be multiplexed onto a single fibre [21]. In the first interferometric fibre acoustic sensor, the acoustic field interacted directly with the conventional silica fibre [22]. This early interferometric acoustic sensor based on conventional silica fibre had the NR of ~-340dB re ($1\mu Pa^{-1}$), which was sufficient to prove the concept, but it was clear that the improvement of the NR was required. The first attempts to increase the NR of the interferometric acoustic sensors were made by wrapping the conventional silica fibre around solid plastic mandrels [23]. The NR of this configuration can achieve to ~-325dB, a 15dB improvement in the sensor response over the bare conventional fibre. But it does not provide enough NRs of the interferometric fibre acoustic sensors for supporting large multiplexing [21].

In the mid-1980s investigators started using air-backed structures to further increase the NRs of the fibre acoustic sensors. The new designs included flexural disc configurations and air-backed mandrels (initially of metal tubes) [24]. The NR of the air-backed cylinder structure may be modified by changing the wall thickness of the tubes [25] and can achieve to ~-300dB. But, unlike the solid mandrel or the bare conventional fibre sensor designs, air-backed structures are sensitive to being crushed by the hydrostatic pressure and must be designed with a maximum pressure

(or depth) in mind [21].

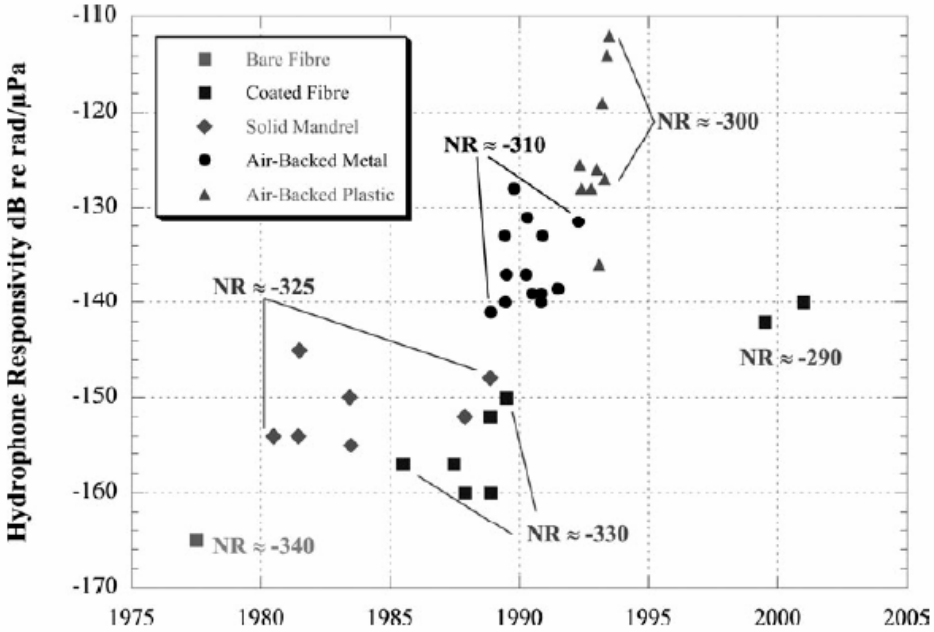

Fig. 1.2 Evolution of the NRs of the interferometric acoustic fibre sensors

Some results for coated fibre acoustic sensors use compliant coatings directly applied to the conventional silica fibre to increase their NR. This represents the simplest and potentially lowest cost acoustic sensor design as no additional components are needed and the coating can be extruded onto the fibre. Coated fibre acoustic sensors have been investigated over the last 25 years [26-30], with little improvement in NR, until recently. Air-included polymer coatings have recently been shown to increase the NR by as much as 40dB over the previous coated fibre acoustic sensors [31, 32]. The evolution of the NRs of the interferometric acoustic fibre sensors is shown in Fig. 1.2 [21].

1.1.1.2 High Birefringence Fibre sensors

The high-birefringence fibre (HBF) has been widely used in coherent optical-fibre communication systems and optical-fibre sensors [33]. In conventional HBFs, high-birefringence may be induced by two effects: 1) the geometric effect, which comes from the geometric asymmetry of the fibre's profile; 2) the built-in stress effect, which is induced by the doped regions near the fibre core. These doped regions have larger thermal expansion coefficients than the fibre's silica background, which induces high asymmetric built-in stress of the fibre core in its manufacture process. Thus the general expression of the fibre birefringence (B) can be expressed as:

$$B = B_g + B_{bi} \tag{1.1}$$

where B_g is the fibre birefringence induced by geometric asymmetry effect and B_{bi} is the contribution of built-in stress effect to the birefringence of the HBF. For conventional bow-tie and PANDA fibres [33], their doped regions in the fibre cladding cause both geometric asymmetries of the fibre's profiles and the built-in stress in the fibre cores. Thus for those two kind of HBFs, their high birefringence comes from both two effects of Eq. (1.1). For high-birefringence elliptical fibres (HBEF) mentioned in Ref. [34], its birefringence is induced by the elliptical shapes of the fibre's core and cladding. Thus the high-birefringence property of this HBEF comes mainly from the B_g, and the built-in stress in HBEF can be neglected.

When the HBFs are used for optical fibre strain and temperature sensors, in order to improve the sensor performances, the birefringence responses of the HBF to axial strain and temperature need to be investigated [36-38]. When the HBF is subjected to an axial strain (ε), the change of the fibre birefringence (ΔB) can be expressed as:

$$\frac{\Delta B}{\varepsilon} = \frac{\Delta B}{\Delta G}\frac{\Delta G}{\varepsilon} + \frac{\Delta B}{\Delta n_m}\frac{\Delta n_m}{\varepsilon} \tag{1.2}$$

where ΔG is the geometric deformation of the fibre and Δn_m is the index change of the fibre material induced by axial strain. In the right-hand side of Eq. (1.2), the first

term is a geometry-term that represents the contribution of strain-induced geometric deformation to the fibre birefringence. The second term is a material index-term that is associated only with the strain-induced index changes of the fibre materials.

When the HBF is subjected to a temperature variation (ΔT), its birefringence change can be expressed as:

$$\frac{\Delta B}{\Delta T} = \frac{\Delta B}{\Delta G}\frac{\Delta G}{\Delta T} + \frac{\Delta B}{\Delta n_m}\frac{\Delta n_m}{\Delta T} + \frac{\Delta B}{\Delta \varepsilon_{built-in}}\frac{\Delta \varepsilon_{built-in}}{\Delta T} \qquad (1.3)$$

where the first and second terms of the right-hand side of Eq. (1.3) represent the effects of temperature-induced geometric deformation of the fibre and contribution of the index changes of fibre materials to the fibre birefringence respectively. The third term is the built-in stress term, which represents the fact that the temperature variation releases part of the built-in stress in the fibre's core.

Table 1 Birefringence and birefringence sensitivities to axial strain and temperature variation for conventional PANDA fibre and HB-PCF at the wavelength of 1550 nm.

Fibre	PANDA fibre	HB-PCF
Birefringence (B)	~$5.11*10^{-4}$	~$8.7*10^{-4}$
Birefringence sensitivity to axial strain ($\Delta B/\varepsilon$)	~$8.3*10^{-3}$ (ε^{-1})	~$-7.4*10^{-4}$ (ε^{-1})
Birefringence sensitivity to temperature ($\Delta B/\Delta T$)	~$-3.11*10^{-7}$ (K^{-1})	~$-5.2*10^{-10}$ (K^{-1})

The birefringence and the birefringence sensitivities of high-birefringence PANDA fibre to axial strain and temperature, at the wavelength of 1550nm, are summarized in Table 1 [36]. It can be seen in Table 1 that the conventional PANDA fibre has large birefringence of ~10^{-4}. And the birefringence sensitivities of such PANDA fibre to axial strain and temperature are about $8.3*10^{-3}$ (ε^{-1}) and $-3.11*10^{-7}$ (K^{-1})

respectively.

1.1.1.3 In-fibre Polarization Controllers

The optical polarization controller (PC) has been widely used in fibre sensors and communication systems. Compared with their bulk counterparts, all-fibre in-line PCs have the advantages of easier alignment, smaller insertion loss, and full compatibility with optical fibre systems. Several techniques have been reported for building in-fibre PCs in conventional single mode fibres (SMFs), including bending the fibre into loops to control the state of polarization (SOP) [41]; using three surface pressing components with 45º between each other to produce elastic-optically induced birefringence on the fibre [42]; and using micro-heaters deposited on short section of polarization maintaining fibre to thermally induce differential phase changes between orthogonal polarizations [43].

1.1.2 Photonic Crystal Fibres and Their Applications

Photonic crystal fibres, fibres with a periodic transverse microstructure, have been in practical existence as low-loss waveguides since early 1996 [53]. It is now possible to manufacture the microstructure in air-glass PCF to accuracies of 10 nm on the scale of 1 μm, which allows remarkable control of key optical properties such as dispersion, birefringence, nonlinearity, and position and width of the photonic band gaps in the periodic cladding. The original motivation for developing PCFs was the creation of a new kind of dielectric waveguide, which guides light by means of two-dimensional photonic band gap. The first successful air-silica PCF structure was made by stacking 217 silica capillaries (eight layers outside the central capillary), and it had a solid central core surrounded by 216 air channels [54, and 55]. This led to the discovery of endless single-mode PCF, which led rapidly to a whole series of new types of PCFs: larger mode area PCF [56], dispersion controlled PCF [57],

hollow core PBF [58], high-birefringence PCF [59], and multi-core PCF [60].

Photonic crystal fibres come in two main classes, distinguished by their guiding mechanism. The first class is referred to as index-guiding PCFs, which includes solid-core PCF. These fibres guide light through a modified version of total internal reflection and behave very much like a step-index conventional fibre for single frequencies, but when considering wide-band applications, the highly dispersive cladding can produce optical properties not available from conventional silica fibre, such as endlessly single-mode operation. The second class of PCFs is referred to as photonic bandgap fibres, which includes hollow-core photonic bandgap fibre (hollow-core PBF). These fibres guide light by creating a band gap in their air-silica cladding surrounding a hollow core. The band gap structure acts as a reflective assembly that confines light to the hollow core of the fibre, which offers the potential for reduced scattering [61], lower nonlinearity [62], and potentially lower loss [63] than conventional silica fibres.

The diversity of new or improved features beyond conventional silica fibres means that PCFs are finding an increasing number of applications in many areas of science and technology. As for fibre-optical sensors and devices based on PCFs, the unique light-guiding mechanism and the holey geometry let PCFs explore many fields of applications including: 1) Fibre lasers based on PCFs [64, 65 and 66]; 2) PCF cutting and joining [67 and 68]; 3) PCF mode transformers [69]; 4) PCF polarizer [70 and 71]; 5) PCF wavelength filters [72, 73 and 74]; 6) Laser tweezers in hollow-core PCF [75, 76 and 77]; 7) Biomedical sensing based on PCF [78]; 8) Multi-core PCF for bend and shape sensing [79]; 9) Double-clad PCF in multi-photon fluorescence measurements [80]; 10) Solid-core PCF for hydrostatic pressure sensing [81]; 11) Hollow-core PBF gyroscope [82, 83]; and 12) Hollow-core PBF acoustic sensor [84].

1.1.2.1 High-birefringence Photonic Crystal Fibres

The high-birefringence photonic crystal fibre (HB-PCF) was demonstrated in 2001 [35]. The high birefringence of such fibre is induced by varying diameter of one pair of the cladding air-holes and there is no doped region in the fibre's profile, thus the high-birefringence of such fibre comes mainly from B_g, and the built-in stress term of equation (1.1) can be neglected.

The birefringence sensitivity of this HB-PCF to temperature ($\Delta B/\Delta T$) is much smaller than the value of conventional PANDA fibre. This is because in the cladding of the HB-PCF there is no doped region [35], and therefore no built-in stress generated during its manufacturing process. It can also been seen in Table 1 that the birefringence sensitivity ($\Delta B/\varepsilon$) to axial strain for the HB-PCF, is about ten times smaller than the value of PANDA fibre. This is because for the HC-PCF, the high-birefringence comes from varying the diameters of two cladding air-holes, thus the material index-term of Eq. (1.2) for this HB-PCF is much smaller than that of the conventional PANDA fibre, of which the high-birefringence is induced by two high-index doped regions in its cladding.

In recent years, a hybrid PCF guiding light by both index-guiding and bandgap-guiding simultaneously was demonstrated [39]. This hybrid PCF was composed of air-holes (arranged in a hexagonal pattern) and Ge-doped silica rods (replaced a single row of air holes along one of the hybrid PCF axes). Because the guiding mechanisms of the hybrid PCF are different in two orthogonal directions, high birefringence is expected [40]. However, the birefringence sensitivities of this hybrid PCF to strain and temperature are not investigated.

1.1.2.2 Hollow-core PBF Polarization Controller

Hollow-core photonic bandgap fibres (HC-PBFs), since their first demonstration of single-mode light guidance in 1999 [44], have been a subject of continuing interest over the past ten years. To realize the full potential of HC-PBFs, it is often necessary to splice HC-PBFs with conventional fibre components to form functional circuits or sub-systems. To this end, low loss and robust splicing between these fibres is important and has been a topic of considerable interest [45, 46, and 47]. Alternatively, in-line components may be built directly on the HC-PBF and this avoids the problems associated with splicing different types of optical fibres. There are active researchers along this line, HC-PBF based fibre polarizer [48], wavelength filter [49], and coupler [50 and 51] are demonstrated or proposed.

Terrel et al. reported a HC-PBF PC made by twisting three sections of a HC-PBF [52]. This PC makes use of the inherent birefringence of the HB-PBF and the lengths of the twisted sections are chosen to be the beat length of the HC-PBF. For the HC-PBF, it should be noted that the inherent birefringence is a residual effect due to manufacturing imperfection, and the HC-PBF is not intended to have any birefringence. The inherent birefringence of the fibre causes wavelength dependent delay between the two orthogonal SOPs, and for the same SOP at the input, lights out of the PC may have different SOPs for different wavelengths, and this narrows down the bandwidth of the PC.

1.2 Motivation and Significance of This Work

Because of the differences between PCFs and conventional silica fibres in both elastic structure and light-guiding mechanism, comparing with conventional silica fibres, PCFs show different responses to external measurands. Recently, more and more cases that use PCFs as the sensing elements to detect external measurands are reported or proposed. However, to our knowledge, general theoretical models for

analysing the responses of PCFs to strain, pressure and temperature have not been investigated.

In this dissertation, we construct general models for three types of PCFs, which can be used to simulate responses of those PCFs to different measurands, such as axial strain, acoustic pressure, lateral pressure, and temperature. The simulation results show that compared with conventional silica fibre, PCFs show some novel or improved responses to the external measurands, and those responses can be adjustable for different applications because the fibre parameters of PCFs are flexible. Those advantages give rise to several new PCF applications for sensors and devices.

1.3 Dissertation Outline

Chapter 2 We construct the elastic model for the solid-core PCF in Section 2.1. The deformations of the solid-core PCF due to axial strain, acoustic pressure and temperature are simulated with this elastic model in Section 2.2. In Section 2.3, the phase sensitivities of the solid-core PCF to axial strain, acoustic pressure and temperature are simulated respectively. Finally, a summary of Chapter 2 is presented in Section 2.4.

Chapter 3 We construct the elastic mode for the hollow-core PBF in Section 3.1. The deformations of the hollow-core PBF due to axial strain, acoustic pressure, temperature and lateral pressure are simulated with this elastic model in Section 3.2. In Section 3.3, the phase sensitivities of the hollow-core PBF to axial strain, acoustic pressure and temperature are calculated respectively. In Section 3.4, the birefringence change of the hollow-core PBF due to lateral pressure is simulated theoretically. Finally, a summary of Chapter 3 is presented in Section 3.5.

Chapter 4 We construct the elastic mode for the hybrid PCF in Section 4.1. The birefringence property of the hybrid PCF is simulated by using the theoretical model in Section 4.2. In Section 4.3, the birefringence responses of the hybrid PCF to axial strain and temperature are calculated respectively. Finally, a summary of Chapter 4 is presented in Section 4.4.

Chapter 5 The phase sensitivities of two types of PCFs, one type of solid-core PCF and one type of hollow-core PBF to axial strain are measured and the results are shown in Section 5.1. The phase sensitivity of one type of hollow-core PBF to acoustic pressure is measured experimentally and the results are shown in Section 5.2. Finally, a summary of Chapter 5 is presented in Section 5.3.

Chapter 6 The experimental setup and the working principle of a hollow-core PBF polarization controller based on lateral pressures are demonstrated in Section 6.1. The experimental results of this hollow-core PBF PC measured in Section 6.2. Finally, a summary of Chapter 6 is presented in Section 6.3.

Chapter 7 The experimental setup for the measurements of the birefringence properties of the hybrid PCF is demonstrated in Section 7.1. The birefringence responses of the hybrid PCF to axial strain and temperature are measured respectively in Section 7.2 and 7.3. In Section 7.4, a design of hybrid PCF and its applications are proposed. Finally, a summary of Chapter 7 is presented in Section 7.5.

Chapter 8 In the last chapter, we summarize the research work accomplished in this dissertation.

Chapter 2

Theoretical Modelling for Solid-core PCFs

2.1 Elastic Model of Solid-core PCFs

The model for simulating the conventional silica fibres were well described by Hocker, Lagakos and Budiansky [27, 28 and 29]. Unlike conventional silica which has only two regions (the silica region and the polymer jacket region) in its profile, the solid-core PCFs have a solid silica core, an air-silica microstructure inner cladding, a solid silica outer cladding, and an acrylete or other polymer jacket. The elastic model of solid-core PCFs may be modelled as a structure with four circular regions: Region 1 is the solid core with radius of a; Region 2 is the air-silica inner cladding with thickness of b-a; Region 3 is the silica outer cladding with the thickness of c-b; and finally they are coated with the Region 4: polymer jacket, to the radius of d; The cross-section of the solid-core PCF is shown in Fig. 2.1.

Each region in Fig. 2.1 is characterized by a certain elastic modulus E and Poisson's ratio of v. The materials of silica core, silica outer cladding and polymer jacket are homogeneous, and their Young's modulus and Poisson's ratios can be expressed as E_1, E_3, E_4, v_1, v_3, and v_4 respectively. The air-silica inner cladding of the solid-core PCF is an exception in that it is not a homogeneous material but behaves mechanically like a honeycomb [85, 86 and 87]. The Young's modulus and Poisson's ratio of this honeycomb cladding are anisotropic and are the function of its air-filling ratio η. For a hexagonal pattern of air holes in the air-silica cladding, their Young's modulus and Poisson's ratio can be expressed as Eqs. (2.1) and (2.2) [85].

$$\begin{cases} E_r = E_\theta = \dfrac{3}{2}(1-\eta)^3 E_0 = E_2^* \\ E_z = (1-\eta)E_0 = E_2 \end{cases} \tag{2.1}$$

$$\begin{cases} v_{r-\theta} = v_{\theta-r} = 1 \\ v_{z-\theta} = v_{z-r} = v_0 \\ v_{r-z} = v_{\theta-z} \approx 0 \end{cases} \tag{2.2}$$

In Eqs (2.1) and (2.2), E_0 is the Young's modulus of the silica material, v_0 is its Poisson's ratio. E_r, E_θ, and E_z are the Young's modulus of the air-silica honeycomb cladding in the three directions, and $v_{r\text{-}\theta}$, $v_{\theta\text{-}r}$, $v_{z\text{-}\theta}$, $v_{\theta\text{-}z}$, $v_{r\text{-}z}$, and $v_{z\text{-}r}$ are the six Poisson's ratios of the honeycomb cladding.

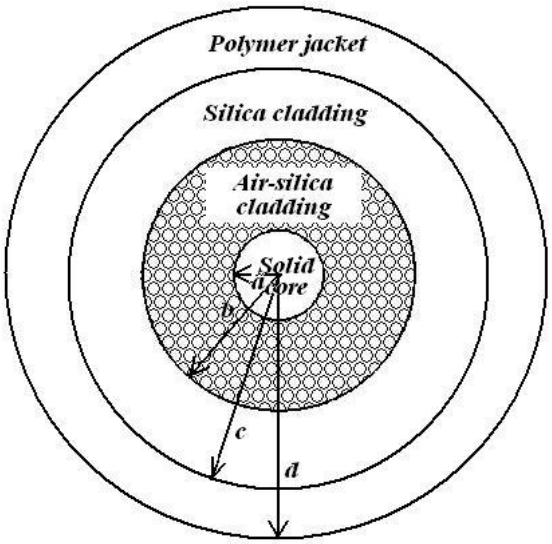

Fig. 2.1 Cross-section of a solid-core PCF with a solid silica core, an air-silica inner cladding, a silica outer cladding and a polymer jacket.

For discussing strains, stresses and displacements in all regions of the solid-core PBF due to external measurands, it is advantageous to use polar coordinates. Using the knowledge of the of elasticity [88], the stress equilibrium equations in each region of the solid-core PCF can be expressed as:

$$\begin{aligned}&\frac{\partial\sigma_r^i}{\partial r}+\frac{1}{r}\frac{\partial\tau_{r\theta}^i}{\partial\theta}+\frac{\sigma_r^i-\sigma_\theta^i}{r}=0\\&\frac{1}{r}\frac{\partial\sigma_\theta^i}{\partial\theta}+\frac{\partial\tau_{r\theta}^i}{\partial r}+\frac{2\tau_{r\theta}^i}{r}=0\end{aligned}\tag{2.3}$$

where σ_r^i is the normal stress component of region i in the radial direction, σ_θ^i is the normal stress component of region i in the tangential direction, and $\tau_{r\theta}^i$ is the shearing stress component of region i.

When the external measurands are symmetrical about the z-axis of the solid-core PCF and well-proportioned along the z-direction, the stress distribution of each region depends on r only, on this condition the solutions of Eq. (2.3) are shown as Eq. (2.4), where A_i, B_i, C_i, and D_i (i=*1*, *2*, *3* and *4*) are constants.

$$\begin{aligned}&\sigma_r^i=\frac{A_i}{r^2}+B_i(1+2\log r)+2C_i\\&\sigma_\theta^i=-\frac{A_i}{r^2}+B_i(3+2\log r)+2C_i\\&\tau_{r\theta}^i=0\\&\sigma_z^i=D_i\end{aligned}\tag{2.4}$$

For region 1 of the solid-core PCF, there is no hole at the origin, thus both A_1 and B_1 are zero [88]. The stress expressions of the first region can be written as Eq. (2.5).

$$\begin{cases}\sigma_r^1=2C_1\\\sigma_\theta^1=2C_1\\\sigma_z^1=D_1\end{cases}\tag{2.5}$$

For regions 2, 3, and 4, there are holes at their origins, thus in Eq. (2.4) only B_i are zeros [88]. The normal stress equation of those regions can be expressed as Eq (2.6).

$$\begin{aligned}
\sigma_r^i &= \frac{A_i}{r^2} + 2C_i \\
\sigma_\theta^i &= -\frac{A_i}{r^2} + 2C_i \qquad (i = 2,3,4) \\
\sigma_z^i &= D_i
\end{aligned} \tag{2.6}$$

Using Hooke's law, the strain tensors of different regions can be obtained. For the solid silica core region, the Young's modulus and Poisson's ratio are E_1 and v_1 respectively. The strain expression of this region can be written as Eq. (2.7).

$$\begin{cases}
\varepsilon_r^1 = \dfrac{1}{E_1}[2(1-v_1)C_1 - v_1 D_1] \\
\varepsilon_\theta^1 = \dfrac{1}{E_1}[2(1-v_1)C_1 - v_1 D_1] \\
\varepsilon_z^1 = \dfrac{1}{E_i}(D_1 - 4v_1 C_1)
\end{cases} \tag{2.7}$$

For the region of air-silica inner cladding, its Young's modulus and Poisson's ratio are shown in Eqs. (2.1) and (2.2). Using Hooke's law, the strain expression of the air-silica cladding can be written as Eqs. (2.8).

$$\begin{cases}
\varepsilon_r^2 = \dfrac{2A_2}{E_2^* r^2} - v_1 \dfrac{D_2}{E_2} \\
\varepsilon_\theta^2 = -\dfrac{2A_2}{E_2^* r^2} - v_1 \dfrac{D_2}{E_2} \\
\varepsilon_z^2 = \dfrac{D_2}{E_2} + \alpha_2 \Delta T
\end{cases} \tag{2.8}$$

For the two regions, the silica outer cladding and the polymer jacket of the solid-core PCF, their Young's modulus and Poisson's ratio can be written as E_3, E_4, v_3, and v_3 respectively. Using Hooke's law, the strain expression of those two regions can be obtained as Eq. (2.9).

$$\begin{cases} \varepsilon_r^i = \dfrac{1}{E_i}[(1+v_i)\dfrac{A_i}{r^2} + 2(1-v_i)C_i - v_i D_i] \\ \varepsilon_\theta^i = \dfrac{1}{E_i}[-(1+v_i)\dfrac{A_i}{r^2} + 2(1-v_i)C_i - v_i D_i] \qquad (i=3,4) \\ \varepsilon_z^i = \dfrac{1}{E_i}(D_i - 4v_i C_i) \end{cases} \tag{2.9}$$

2.2 Deformations of Solid-core PCFs Due to Different Measurands

In Section 2.1, we construct the elastic model for the solid-core PCF. The elastic model gives general stress and strain expressions of each region of the solid-core fibre, when the fibre is subjected to symmetrical and z-direction well-proportioned measurands. In this section, we will discuss the deformations of the solid-core PCF, when the fibre is subjected to axial strain, acoustic pressure and temperature. Because all of those three measurands are symmetrical and they are all well-proportioned along the z-direction, the stress and strain expressions discussed in Section 2.1 can be used to simulate the deformations of the solid-core PCF for those three types of measurands.

2.2.1 Axial Strain

In order to get deformations of the solid-core fibre due to axial strain (ε), the constants shown in Equation (2.4) should be determined by the boundary conditions and the stress and displacement continuities across the boundaries between different regions of the solid-core PCF. Under the plane approximation the boundary conditions due to axial strain and the expressions of the stress and displacement continuities may be expressed as Eq. (2.10).

$$
\begin{aligned}
&\sigma_r^1\Big|_{r=a} = \sigma_r^2\Big|_{r=a} && (a)\\
&\sigma_r^2\Big|_{r=b} = \sigma_r^3\Big|_{r=b} && (b)\\
&\sigma_r^3\Big|_{r=c} = \sigma_r^4\Big|_{r=c} && (c)\\
&u_r^1\Big|_{r=a} = u_r^2\Big|_{r=a} && (d)\\
&u_r^2\Big|_{r=b} = u_r^3\Big|_{r=b} && (e)\\
&u_r^3\Big|_{r=c} = u_r^4\Big|_{r=c} && (f)\\
&\sigma_r^4\Big|_{r=d} = 0 && (g)\\
&\varepsilon_z^1 = \varepsilon_z^2 = \varepsilon_z^3 = \varepsilon_z^4 = \varepsilon && (h)
\end{aligned}
\tag{2.10}
$$

In Eq. (2.10), u_r^i is the radial displacement in region i, which is related to radial strain by Eq. (2.11). Eqs. (2.10a), (2.10b) and (2.10c) describe radial stress continuity across the boundaries of the regions; Eqs. (2.10d), (2.10e) and (2.10f) describe the radial displacement continuity across the boundaries of the regions; Eq. (2.10g) means the region outside of the fibre is air; Eq. (2.10h) is for the plane approximation [88], which ignores the end effect.

$$u_r^i = \int \varepsilon_r^i dr \tag{2.11}$$

Substituting Eqs. (2.5), (2.6), (2.7), (2.8), (2.9), and (2.11) into the boundary conditions, the constants A_i, C_i and D_i (i=1, 2, 3, and 4), when the solid-core PCF subjected to axial strain, can be determined by the matrix equation (2.12). Solving this equation, the constants can be obtained, and thus the stress, strain and displacement distributions of each region of the solid-core PCF, when subjected to axial strain can be obtained.

$$
\begin{bmatrix}
2 & -2 & 0 & 0 & -\frac{1}{a^2} & 0 & 0 & 0 & 0 & 0 & 0 \\
0 & 2 & -2 & 0 & \frac{1}{b^2} & -\frac{1}{b^2} & 0 & 0 & 0 & 0 & 0 \\
0 & 0 & 2 & -2 & 0 & \frac{1}{c^2} & -\frac{1}{c^2} & 0 & 0 & 0 & 0 \\
\frac{2a(1-\nu_1)}{E_1} & 0 & 0 & 0 & \frac{2}{E_2^* a} & 0 & 0 & \frac{-\nu_1 a}{E_1} & \frac{\nu_2 a}{E_2} & 0 & 0 \\
0 & 0 & \frac{2b(1-\nu_3)}{E_3} & 0 & \frac{2}{E_2^* b} & \frac{-(1+\nu_3)}{E_3 b} & 0 & 0 & \frac{\nu_2 b}{E_2} & \frac{-\nu_3 b}{E_3} & 0 \\
0 & 0 & \frac{2c(1-\nu_3)}{E_3} & \frac{-2c(1-\nu_4)}{E_4} & 0 & \frac{-(1+\nu_3)}{E_3 c} & \frac{(1+\nu_4)}{E_4 c} & 0 & 0 & \frac{-\nu_3 c}{E_3} & \frac{\nu_4 c}{E_4} \\
\frac{-4\nu_1}{E_1} & 0 & 0 & 0 & 0 & 0 & 0 & \frac{1}{E_1} & 0 & 0 & 0 \\
0 & 0 & 0 & 0 & 0 & 0 & 0 & 0 & \frac{1}{E_2} & 0 & 0 \\
0 & 0 & \frac{-4\nu_3}{E_3} & 0 & 0 & 0 & 0 & 0 & 0 & \frac{1}{E_3} & 0 \\
0 & 0 & 0 & \frac{-4\nu_4}{E_4} & 0 & 0 & 0 & 0 & 0 & 0 & \frac{1}{E_4} \\
0 & 0 & 0 & 2 & 0 & 0 & \frac{1}{d^2} & 0 & 0 & 0 & 0
\end{bmatrix}
\begin{bmatrix} C_1 \\ C_2 \\ C_3 \\ C_4 \\ A_2 \\ A_3 \\ A_4 \\ D_1 \\ D_2 \\ D_3 \\ D_4 \end{bmatrix}
=
\begin{bmatrix} 0 \\ 0 \\ 0 \\ 0 \\ 0 \\ 0 \\ \varepsilon \\ \varepsilon \\ \varepsilon \\ \varepsilon \\ 0 \end{bmatrix}
\tag{2.12}
$$

The theoretical model is applied to calculate the deformation of one type of solid-core PCF (NL-3.3 fibre) [89], when it is subjected to axial strain. This fibre has a solid core and an air-silica cladding with air-filling ratio of ~84%. The air-silica cladding can be approximately considered as uniform honeycomb structure. The SEM photograph of NL-3.3 is shown in Fig. 2.2 and its physical parameters are listed in Table 2.1.

Table 2.1 Physical parameters of NL-3.3

	Pitch	*η*	*a*	*b*	*c*
Fibre	*3 (μm)*	*84%*	*1.65(μm)*	*15(μm)*	*75(μm)*
	d	$E_0=E_1=E_3$	E_4	$\upsilon_0=\upsilon_1=\upsilon_3$	υ_4
NL-3.3	*125(μm)*	*72(GPa)*	*0.5(GPa)*	*0.17*	*0.37*

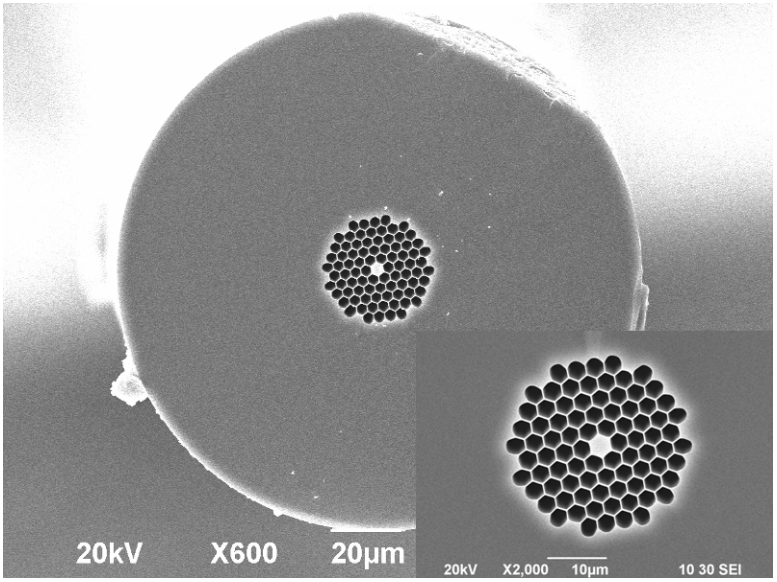

Fig 2.2 SEM photograph of one type of solid-core PCF (NL-3.3)

Using the physical parameters shown in Table 2.1, the deformation of the solid-core PCF (NL-3.3) due to axial strain can be calculated by using the theoretical model. For example, we plotted the radial displacements u_r^i of each region of the NL-3.3 fibre as the function of distance from the fibre centre in Fig. 2.3, when the fibre is subjected to axial strain of -10^{-3} (ε).

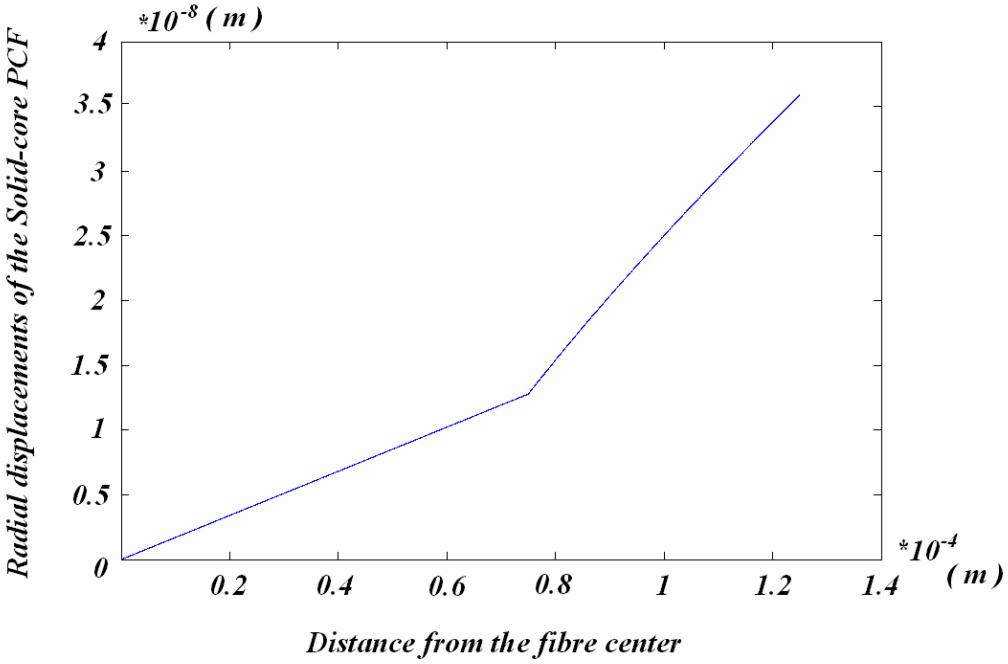

Fig. 2.3 Radial displacement as the function of distance from the fibre centre for the NL-3.3 fibre, when the fibre is subjected to axial strain of -10^{-3} (ε).

It can be seen in Fig. 2.3 that the radial displacements of the inner three regions increase linearly with the increasing of the distance from the fibre centre. It can be explained that the regions of solid silica core, air-silica inner cladding and silica outer cladding have the same material of silica. Thus when the fibre is subjected to axial strain, the radial strains of those three inner regions keep similar value. Compared with silica material, the material of the jacket is one type of polymer much more flexible than the silica, thus in this polymer jacket region the radial strain is larger than the other three regions.

2.2.2 Acoustic Pressure

The constants shown in Equation (2.4), when the solid-core PCF is subjected to acoustic pressure (*-dP*), are also determined by the boundary conditions and the stress and displacement continuities across the boundaries between different regions

of the solid-core PCF. Under the plane approximation the boundary conditions due to acoustic pressure and the expressions of the stress and displacement continuities may be expressed as Eq. (2.13).

$$
\begin{aligned}
&\sigma_r^1\big|_{r=a} = \sigma_r^2\big|_{r=a} && (a)\\
&\sigma_r^2\big|_{r=b} = \sigma_r^3\big|_{r=b} && (b)\\
&\sigma_r^3\big|_{r=c} = \sigma_r^4\big|_{r=c} && (c)\\
&u_r^1\big|_{r=a} = u_r^2\big|_{r=a} && (d)\\
&u_r^2\big|_{r=b} = u_r^3\big|_{r=b} && (e)\\
&u_r^3\big|_{r=c} = u_r^4\big|_{r=c} && (f)\\
&\sigma_r^4\big|_{r=d} = -(dP) && (g)\\
&\varepsilon_z^1 = \varepsilon_z^2 = \varepsilon_z^3 = \varepsilon_z^4 && (h)\\
&-(dP)d^2 = \sigma_z^1 a^2 + \sigma_z^2 (b^2 - a^2) &&\\
&+\sigma_z^3 (c^2 - b^2) + \sigma_z^4 (d^2 - c^2) && (i)
\end{aligned}
\qquad (2.13)
$$

Eqs. (2.13*a*), (2.13*b*) and (2.13*c*) describe radial stress continuity across the boundaries of the regions; Eqs. (2.13*d*), (2.13*e*) and (2.13*f*) describe the radial displacement continuity across the boundaries of the regions; Eq. (2.13*g*) and (2.13*i*) are the hydrostatic condition, and Eq. (2.13*h*) is for the plane approximation [88].

Substituting Eqs. (2.5), (2.6), (2.7), (2.8), (2.9), and (2.11) into the boundary conditions, the constants A_i, C_i and D_i (i=1, 2, 3, and 4), when the solid-core PCF subjected to acoustic pressure, can be determined by the matrix equation (2.14). Solving this equation, the constants can be obtained, and thus the stress, strain and displacement distributions of each region of the solid-core PCF, when subjected to acoustic pressure can be obtained.

$$
\begin{bmatrix}
2 & -2 & 0 & 0 & -\frac{1}{a^2} & 0 & 0 & 0 & 0 & 0 & 0 \\
0 & 2 & -2 & 0 & \frac{1}{b^2} & -\frac{1}{b^2} & 0 & 0 & 0 & 0 & 0 \\
0 & 0 & 2 & -2 & 0 & \frac{1}{c^2} & -\frac{1}{c^2} & 0 & 0 & 0 & 0 \\
\frac{2a(1-\nu_1)}{E_1} & 0 & 0 & 0 & \frac{2}{E_2^* a} & 0 & 0 & \frac{-\nu_1 a}{E_1} & \frac{\nu_2 a}{E_2} & 0 & 0 \\
0 & 0 & \frac{2b(1-\nu_3)}{E_3} & 0 & \frac{2}{E_2^* b} & \frac{-(1+\nu_3)}{E_3 b} & 0 & 0 & \frac{\nu_2 b}{E_2} & \frac{-\nu_3 b}{E_3} & 0 \\
0 & 0 & \frac{2c(1-\nu_3)}{E_3} & \frac{-2c(1-\nu_4)}{E_4} & 0 & \frac{-(1+\nu_3)}{E_3 c} & \frac{(1+\nu_4)}{E_4 c} & 0 & 0 & \frac{-\nu_3 c}{E_3} & \frac{\nu_4 c}{E_4} \\
0 & 0 & 0 & 2 & 0 & 0 & \frac{1}{d^2} & 0 & 0 & 0 & 0 \\
\frac{4\nu_1}{E_1} & 0 & 0 & 0 & 0 & 0 & 0 & -\frac{1}{E_1} & \frac{1}{E_2} & 0 & 0 \\
0 & 0 & \frac{4\nu_3}{E_3} & 0 & 0 & 0 & 0 & 0 & \frac{1}{E_2} & -\frac{1}{E_3} & 0 \\
0 & 0 & 0 & \frac{4\nu_4}{E_4} & 0 & 0 & 0 & 0 & \frac{1}{E_2} & 0 & -\frac{1}{E_4} \\
0 & 0 & 0 & 0 & 0 & 0 & 0 & a^2(b^2-a^2)(c^2-b^2)(d^2-c^2) & & &
\end{bmatrix}
\begin{bmatrix} C_1 \\ C_2 \\ C_3 \\ C_4 \\ A_2 \\ A_3 \\ A_4 \\ D_1 \\ D_2 \\ D_3 \\ D_4 \end{bmatrix}
=
\begin{bmatrix} 0 \\ 0 \\ 0 \\ 0 \\ 0 \\ 0 \\ -dP \\ 0 \\ 0 \\ 0 \\ -dPd^2 \end{bmatrix}
\tag{2.14}
$$

The deformations of the solid-core PCF (NL-3.3), when it is subjected to acoustic pressure, are calculated [89]. The parameters and the SEM photograph of this NL-3.3 fibre are shown in Table 2.1 and Fig. 2.2 respectively.

The radial displacements u_r^i of each region of the NL-3.3 as the function of distance from the fibre centre are shown in Fig. 2.4, when the fibre is subjected to acoustic pressure of -1 (Pa). It can be seen in Fig. 2.4 that the radial displacements of the inner three regions are much smaller than the displacement of the polymer jacket. This is because, comparing with silica material, the polymer is much more flexible.

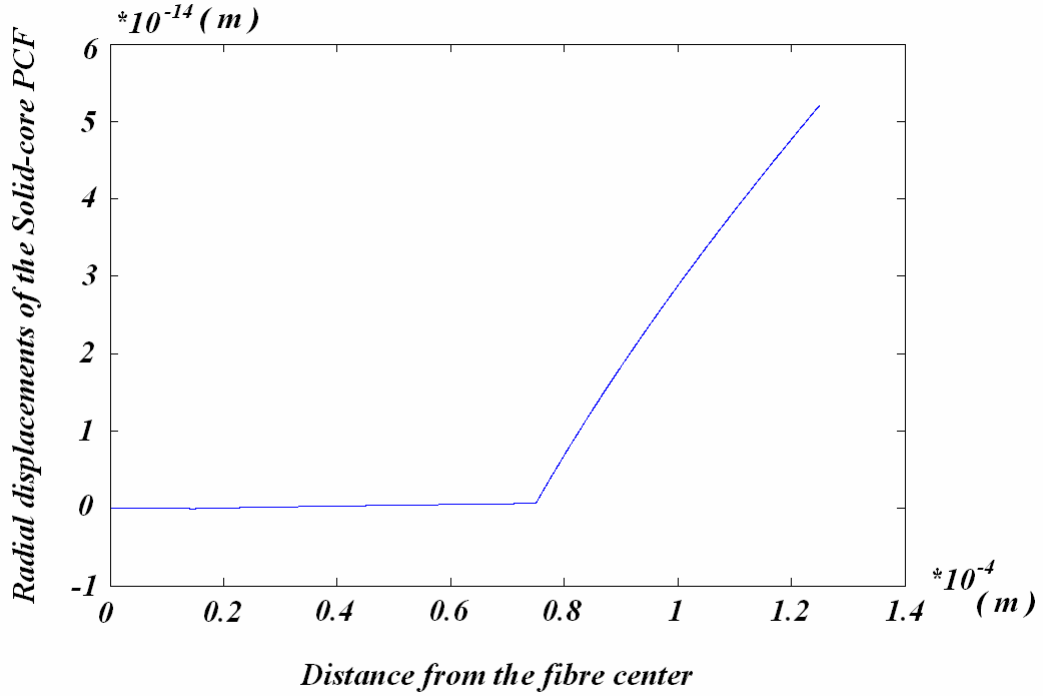

Fig. 2.4 Radial displacement as the function of distance from the fibre centre for the NL-3.3 fibre, when the fibre is subjected to acoustic pressure of -1Pa.

2.2.3 Temperature

When the solid-core PCF is subjected to temperature variation of (ΔT), the stress expressions of regions are also shown as Eqs. (2.5) and (2.6). However, the strain expressions of the solid-core PCF due to temperature variation are different with the strain equations due to axial strain or acoustic pressure. The thermal expansion terms ($\alpha_i \Delta T$) should be added into the strain expressions of each region as expressed as Eq. (2.15), where α_i (i=1, 2, 3 and 4) are the thermal expansion coefficients of the four regions.

$$\begin{cases} \varepsilon_r^1 = \dfrac{1}{E_1}[2(1-v_1)C_1 - v_1 D_1] + \alpha_1 \Delta T \\ \varepsilon_\theta^1 = \dfrac{1}{E_1}[2(1-v_1)C_1 - v_1 D_1] + \alpha_1 \Delta T \\ \varepsilon_z^1 = \dfrac{1}{E_i}(D_1 - 4v_1 C_1) + \alpha_1 \Delta T \end{cases} \qquad \begin{cases} \varepsilon_r^2 = \dfrac{2A_2}{E_2^* r^2} - v_2 \dfrac{D_2}{E_2} + \alpha_2 \Delta T \\ \varepsilon_\theta^2 = -\dfrac{2A_2}{E_2^* r^2} - v_2 \dfrac{D_2}{E_2} + \alpha_2 \Delta T \\ \varepsilon_z^2 = \dfrac{D_2}{E_2} + \alpha_2 \Delta T \end{cases} \tag{2.15}$$

$$\begin{cases} \varepsilon_r^i = \dfrac{1}{E_i}[(1+v_i)\dfrac{A_i}{r^2} + 2(1-v_i)C_i - v_i D_i] + \alpha_i \Delta T \\ \varepsilon_\theta^i = \dfrac{1}{E_i}[-(1+v_i)\dfrac{A_i}{r^2} + 2(1-v_i)C_i - v_i D_i] + \alpha_i \Delta T \qquad (i = 3, 4) \\ \varepsilon_z^i = \dfrac{1}{E_i}(D_i - 4v_i C_i) + \alpha_i \Delta T \end{cases}$$

$$\begin{aligned}
&\sigma_r^1\Big|_{r=a} = \sigma_r^2\Big|_{r=a} && (a)\\
&\sigma_r^2\Big|_{r=b} = \sigma_r^3\Big|_{r=b} && (b)\\
&\sigma_r^3\Big|_{r=c} = \sigma_r^4\Big|_{r=c} && (c)\\
&u_r^1\Big|_{r=a} = u_r^2\Big|_{r=a} && (d)\\
&u_r^2\Big|_{r=b} = u_r^3\Big|_{r=b} && (e)\\
&u_r^3\Big|_{r=c} = u_r^4\Big|_{r=c} && (f)\\
&\sigma_r^4\Big|_{r=d} = 0 && (g)\\
&\varepsilon_z^1 = \varepsilon_z^2 = \varepsilon_z^3 = \varepsilon_z^4 && (h)\\
&\sigma_z^1 a^2 + \sigma_z^2 (b^2 - a^2) + \sigma_z^3 (c^2 - b^2) \\
&+\sigma_z^4 (d^2 - c^2) = 0 && (i)
\end{aligned} \tag{2.16}$$

The constants are also determined by the boundary conditions and the stress and displacement continuities across the boundaries between different regions of the solid-core PCF. Under the plane approximation, the boundary conditions due to temperature variation and the expressions of the stress and displacement continuities may be expressed as Eq. (2.16).

Eqs. (2.16*a*), (2.16*b*) and (2.16*c*) describe radial stress continuity across the

boundaries of the regions; Eqs. (2.16*d*), (2.16*e*) and (2.16*f*) describe the radial displacement continuity across the boundaries of the regions; Eq. (2.16*g*) and (2.16*i*) mean the pressure out of the fibre is zero, and Eq. (2.16*h*) is for the plane approximation [88].

Substituting Eqs. (2.5), (2.6), (2.15) and (2.11) into the boundary conditions, the constants A_i, C_i and D_i (i=1, 2, 3, and 4), when the solid-core PCF subjected to temperature variation of ΔT, can be determined by the matrix equation (2.17). Solving this equation, the constants can be obtained, and thus the stress, strain and displacement distributions of each region of the solid-core PCF, when subjected to temperature variation can be obtained.

$$\begin{bmatrix}
2 & -2 & 0 & 0 & -\frac{1}{a^2} & 0 & 0 & 0 & 0 & 0 & 0 \\
0 & 2 & -2 & 0 & \frac{1}{b^2} & -\frac{1}{b^2} & 0 & 0 & 0 & 0 & 0 \\
0 & 0 & 2 & -2 & 0 & \frac{1}{c^2} & -\frac{1}{c^2} & 0 & 0 & 0 & 0 \\
\frac{2a(1-\nu_1)}{E_1} & 0 & 0 & 0 & \frac{2}{E_2^* a} & 0 & 0 & \frac{-\nu_1 a}{E_1} & \frac{\nu_2 a}{E_2} & 0 & 0 \\
0 & 0 & \frac{2b(1-\nu_3)}{E_3} & 0 & \frac{2}{E_2^* b} & \frac{-(1+\nu_3)}{E_3 b} & 0 & 0 & \frac{\nu_2 b}{E_2} & \frac{-\nu_3 b}{E_3} & 0 \\
0 & 0 & \frac{2c(1-\nu_3)}{E_3} & \frac{-2c(1-\nu_4)}{E_4} & 0 & \frac{-(1+\nu_3)}{E_3 c} & \frac{(1+\nu_4)}{E_4 c} & 0 & 0 & \frac{-\nu_3 c}{E_3} & \frac{\nu_4 c}{E_4} \\
0 & 0 & 0 & 2 & 0 & 0 & \frac{1}{d^2} & 0 & 0 & 0 & 0 \\
\frac{4\nu_1}{E_1} & 0 & 0 & 0 & 0 & 0 & 0 & -\frac{1}{E_1} & \frac{1}{E_2} & 0 & 0 \\
0 & 0 & \frac{4\nu_3}{E_3} & 0 & 0 & 0 & 0 & 0 & \frac{1}{E_2} & -\frac{1}{E_3} & 0 \\
0 & 0 & 0 & \frac{4\nu_4}{E_4} & 0 & 0 & 0 & 0 & \frac{1}{E_2} & 0 & -\frac{1}{E_4} \\
0 & 0 & 0 & 0 & 0 & 0 & 0 & a^2(b^2-a^2)(c^2-b^2)(d^2-c^2) & & &
\end{bmatrix}
\begin{bmatrix} C_1 \\ C_2 \\ C_3 \\ C_4 \\ A_2 \\ A_3 \\ A_4 \\ D_1 \\ D_2 \\ D_3 \\ D_4 \end{bmatrix}
=
\begin{bmatrix} 0 \\ 0 \\ 0 \\ (\alpha_2-\alpha_1)\Delta T a \\ (\alpha_2-\alpha_3)\Delta T b \\ (\alpha_4-\alpha_3)\Delta T c \\ 0 \\ (\alpha_1-\alpha_2)\Delta T \\ (\alpha_3-\alpha_2)\Delta T \\ (\alpha_4-\alpha_2)\Delta T \\ 0 \end{bmatrix} \quad (2.17)$$

The deformations of the solid-core PCF (NL-3.3), when it is subjected to temperature variation, are simulated by using this theoretical model. The parameters and the SEM photograph of this NL-3.3 fibre are shown in Table 2.1 and Fig. 2.2 respectively. The thermal expansion coefficients of silica material and polymer

material are $0.55*10^{-6}$ (ε/K) and $8*10^{-5}$ (ε/K) respectively.

The radial displacements u_r^i of each region of the NL-3.3 as the function of distance from the fibre centre are shown in Fig. 2.5, when the fibre is subjected to temperature variation of 1 (K). It can be seen in Fig. 2.5 that the radial displacement of the polymer jacket region is much larger than the displacements of the other three regions of the fibre. This is because the thermal expansion coefficient of the polymer material is much larger than that of the silica material.

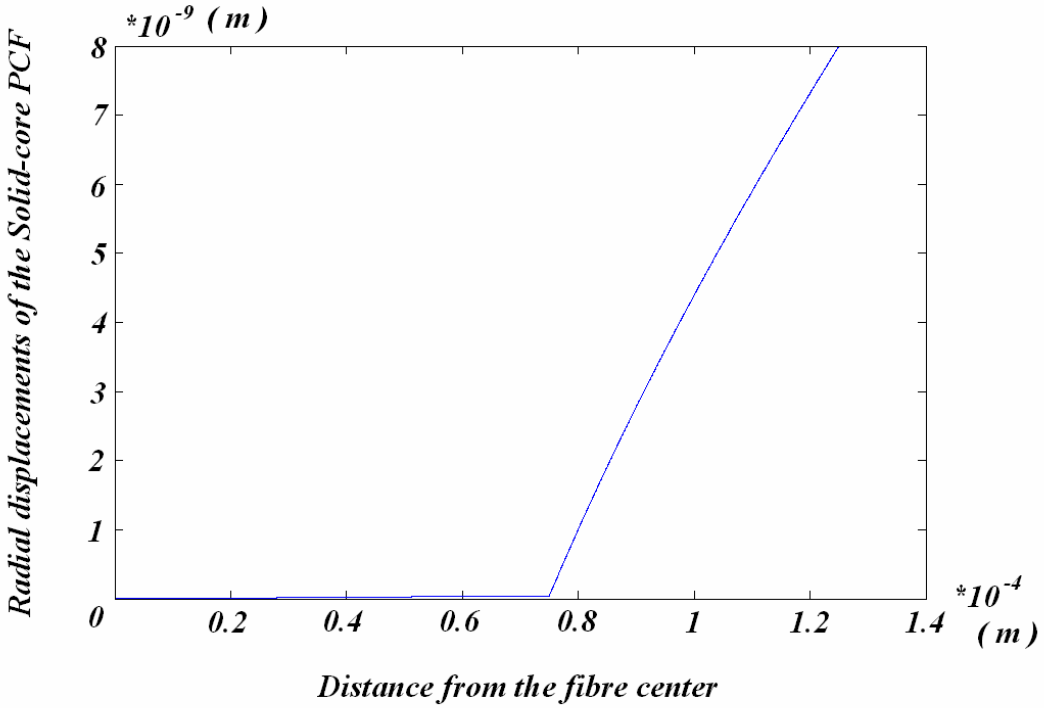

Fig. 2.5 Radial displacement as the function of distance from the fibre centre for the NL-3.3 fibre, when the fibre is subjected to temperature variation of 1 (K).

2.3 Phase Sensitivities of Solid-core PCFs to Different Measurands

In the fibre interferometric sensors, the external measurands result in the phase

differences between the sensing arm and the reference arm, which are measured in the output port of the interferometer. Assuming that the sensing fibre has a length of L, the effective index of fundamental mode is n_{eff}, and the operating light wavelength in vacuum is λ, the phase (φ) accumulated by the fundamental mode travelling through the sensing fibre is given by Eq. (2.18).

$$\varphi = \frac{2\pi}{\lambda} n_{eff} L \tag{2.18}$$

The normalized phase sensitivity of the fundamental mode to a measurand "X" may be generally expressed as:

$$S = \frac{1}{\varphi}\frac{d\varphi}{dX} = \frac{1}{L}\frac{dL}{dX} + \frac{1}{n_{eff}}\frac{dn_{eff}}{dX} = S_L + S_n \tag{2.19}$$

where "X" can be axial strain, acoustic pressure, and temperature. In the right-hand side of Eq. (2.19), the first term (S_L) is a length-term that represents the measurand-induced physical change of the fibre length, and the second term (S_n) is an index term representing the measurand-induced change of the effective refractive index of the fundamental mode.

For the solid-core PCF, the length-term of Eq. (2.19) can be obtained from the z-direction strain of the sensing solid-core fibre. The index-term of Eq. (2.19) is mainly induced by the strain-optic effect of the solid core, because most of light in the solid-core fibre travels through the solid silica core of the fibre.

2.3.1 Axial Strain

The normalized phase sensitivity of the solid-core PCF to axial strain may be expressed as Eq. (2.20).

$$S = \frac{1}{\varphi}\frac{d\varphi}{\varepsilon} = \frac{L}{\varphi}\frac{d\varphi}{dL} = 1 + \frac{L}{n_{eff}}\frac{dn_{eff}}{dL} = 1 + \frac{1}{n_{eff}}\frac{dn_{eff}}{\varepsilon} = S_L + S_n \qquad (2.20)$$

For the normalized phase sensitivity to axial strain, the length term of Eq. (2.20) is one, and the index term of Eq. (2.20) is determined by the strain-optic effect of the solid silica core. The index change of the core material can be expressed as Eq. (2.21), where n_0 is the initial material index of the silica core, p_{11} and p_{12} are the elements of the strain-optic tensors of silica.

$$\begin{aligned}
\Delta n_r^1 &= -\frac{1}{2} n_0^3 (p_{11}\varepsilon_r^1 + p_{12}\varepsilon_\theta^1 + p_{12}\varepsilon_z^1) \\
\Delta n_\theta^1 &= -\frac{1}{2} n_0^3 (p_{12}\varepsilon_r^1 + p_{11}\varepsilon_\theta^1 + p_{12}\varepsilon_z^1) \\
\Delta n_z^1 &= -\frac{1}{2} n_0^3 (p_{12}\varepsilon_r^1 + p_{12}\varepsilon_\theta^1 + p_{11}\varepsilon_z^1)
\end{aligned} \qquad (2.21)$$

Then the index term of the phase sensitivity of the solid-core PCF to axial strain can be expressed as Eq. (2.22).

$$S_n = \frac{1}{n_{eff}}\frac{dn_{eff}}{\varepsilon} = \frac{\Delta n_r^1}{n_0 \varepsilon} \qquad (2.22)$$

For the NL3.3 fibre, the initial material index of the silica core is n_0=1.444, and its p_{11} and p_{12} are 0.121 and 0.27 respectively. The S_n of this solid-core PCF (NL-3.3) to axial strain can be calculated to be ~-0.2119. And thus the normalized phase sensitivity of NL-3.3 to axial strain can be predicted to be S = ~0.7881.

2.3.2 Acoustic Pressure

The normalized phase sensitivity of the solid-core PCF to acoustic pressure may be expressed as Eq. (2.23).

$$S = \frac{1}{\varphi}\frac{d\varphi}{dP} = \frac{1}{L}\frac{dL}{dP} + \frac{1}{n_{eff}}\frac{dn_{eff}}{dP} = \frac{\varepsilon}{dP} + \frac{1}{n_{eff}}\frac{dn_{eff}}{dP} = S_L + S_n \qquad (2.23)$$

For the normalized phase sensitivity to acoustic pressure, the length term of Eq. (2.23) can be calculated by using the *z*-direction strain (ε_r^1) discussed in Section 2.2.2, and the index term of Eq. (2.23) is mainly caused by the strain-optic effect of the solid silica core. The index change of the core material can be expressed as Eq. (2.21) and the index term of the phase sensitivity of solid-core PCF to axial strain can be expressed as Eq. (2.24).

$$S_n = \frac{1}{n_{eff}}\frac{dn_{eff}}{dP} = \frac{\Delta n_r^1}{n_0 dP} \qquad (2.24)$$

For the NL-3.3 fibre, S_L to acoustic pressure can be calculated to be ~-1.683*10^{-11} (ε/Pa) and S_n to acoustic pressure can be calculated to be ~1.168*10^{-11} (1/Pa). And thus the normalized phase sensitivity of NL-3.3 fibre to acoustic pressure can be predicted to be S = -5.15*10^{-12} (1/Pa).

2.3.3 Temperature

The normalized phase sensitivity of the solid-core PCF to temperature may be expressed as Eq. (2.25).

$$S = \frac{1}{\varphi}\frac{d\varphi}{dT} = \frac{1}{L}\frac{dL}{dT} + \frac{1}{n_{eff}}\frac{dn_{eff}}{dT} = \frac{\varepsilon}{dT} + \frac{1}{n_{eff}}\frac{dn_{eff}}{dT} = S_L + S_n \qquad (2.25)$$

For the normalized phase sensitivity to temperature, the length term of Eq. (2.20) can be calculated by using the z-direction strain (ε_r^1) discussed in Section 2.2.3, and the index term of Eq. (2.25) is determined by two effects: 1) the thermal-optic effect of the fibre core, which is shown in Eq. (2.26), and 2) the strain-optic effect of the fibre

core, as shown in Eq. (2.21), where γ is the thermo-optic coefficient of the core material.

$$\Delta n^1 |_{\Delta T} = \gamma \Delta T \tag{2.26}$$

Thus the index term of the phase sensitivity of solid-core PCF to temperature can be expressed as Eq. (2.27).

$$S_n = \frac{1}{n_{eff}} \frac{dn_{eff}}{dT} = \frac{\Delta n^1 \Big|_{\Delta T} + \Delta n_r^1}{n_0 dT} \tag{2.27}$$

For the NL-3.3 fibre, γ of the silica material is $7.8*10^{-6}$ (K^{-1}). The S_L of this solid-core PCF (NL-3.3) to temperature variation can be calculated to be ~$1.14*10^{-6}$ (K^{-1}), and S_n of the NL-3.3 fibre to temperature variation can be calculated to be ~$4.998*10^{-6}$ (K^{-1}). And thus the normalized phase sensitivity of NL-3.3 fibre to temperature can be predicted to be $S = 6.138*10^{-6}$ (K^{-1}).

2.4 Summary

We have constructed the theoretical model for solid-core PCFs. This model can be used to simulate the physical deformations and the effective index changes of the solid-core PCF, when the fibre is subjected to different measurands. One type of solid-core PCF (NL-3.3 fibre) is simulated by using this general model for solid-core PCF. The simulation results show that the NL-3.3 fibre has the normalized phase sensitivity to axial strain of ~0.7881, normalized phase sensitivity to acoustic pressure of ~$-5.15*10^{-12}$ (Pa^{-1}), and normalized phase sensitivity to temperature of ~$6.138*10^{-6}$ (K^{-1}).

Chapter 3

Theoretical Modelling for Hollow-core PBFs

3.1 Elastic Model of hollow-core PBFs

Unlike the solid-core PCF which has a solid core in its profile, the core of the hollow-core PBF is air, and thus the elastic model of the hollow-core PBF may be modelled as a structure with four circular regions: Region 1 is the air core with radius of *a*; Region 2 is the honeycomb inner cladding with thickness of *b*-*a*; Region 3 is the silica outer cladding with the thickness of *c*-*b*; and finally they are coated with the Region 4: polymer jacket, to the radius of *d*; The cross-section of the hollow-core PBF is shown in Fig. 3.1.

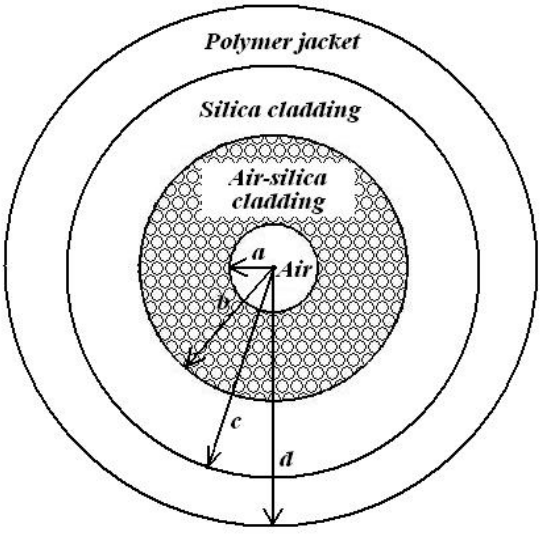

Fig. 3.1 Cross-section of a hollow-core PBF with an air core, an air-silica inner cladding, a silica outer cladding and a polymer jacket.

Regions 2, 3, and 4 in Fig. 3.1 can be characterized by a certain elastic modulus E and Poisson's ratio of v. The materials of silica outer cladding and polymer jacket are homogeneous, and their Young's modulus and Poisson's ratios can be expressed as E_3, E_4, v_3, and v_4 respectively. The air-silica inner cladding of the solid-core PCF is an exception in that it is not a homogeneous material but behaves mechanically like a honeycomb [85, 86 and 87]. The Young's modulus and Poisson's ratio of this honeycomb cladding are anisotropic and are thus the function of its air-filling ratio η. For a hexagonal pattern of air holes in the air-silica cladding, their Young's modulus and Poisson's ratio can be expressed as Eqs. (2.1) and (2.2) [85].

As discussion in Chapter 2, all of the air-silica inner cladding, silica outer cladding and the polymer jacket have holes at their origins. When the fibre is subjected to symmetric measurands, such as axial strain, acoustic pressure and temperature variation, the stress expressions of those regions 2, 3 and 4 can be written as Eq. (3.1).

$$\begin{aligned} \sigma_r^i &= \frac{A_i}{r^2} + 2C_i \\ \sigma_\theta^i &= -\frac{A_i}{r^2} + 2C_i \qquad (i = 2,3,4) \\ \sigma_z^i &= D_i \end{aligned} \tag{3.1}$$

Using Hooke's law, the strain tensors of those three regions can be obtained and shown in Eq. (3.2).

$$\begin{cases} \varepsilon_r^2 = \dfrac{2A_2}{E_2^* r^2} - v_1 \dfrac{D_2}{E_2} \\ \varepsilon_\theta^2 = -\dfrac{2A_2}{E_2^* r^2} - v_1 \dfrac{D_2}{E_2} \\ \varepsilon_z^2 = \dfrac{D_2}{E_2} + \alpha_2 \Delta T \end{cases} \qquad \begin{cases} \varepsilon_r^i = \dfrac{1}{E_i}[(1+v_i)\dfrac{A_i}{r^2} + 2(1-v_i)C_i - v_i D_i] \\ \varepsilon_\theta^i = \dfrac{1}{E_i}[-(1+v_i)\dfrac{A_i}{r^2} + 2(1-v_i)C_i - v_i D_i] \qquad (i = 3,4) \\ \varepsilon_z^i = \dfrac{1}{E_i}(D_i - 4v_i C_i) \end{cases} \tag{3.2}$$

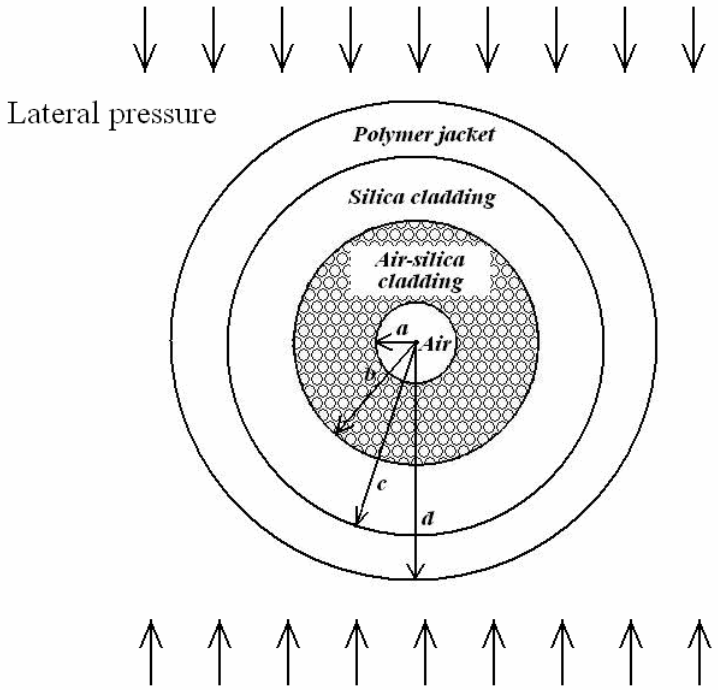

Fig. 3.2 Hollow-core PBF subjected to asymmetric lateral pressure

When the fibre is subjected to the lateral pressure, which is an asymmetric measurand, as shown in Fig. 3.2, using the knowledge of theory of elasticity, the stress expressions of the regions 2, 3 and 4 of the hollow-core PBF in the polar coordinates can be written as Eq. (3.3) [88].

$$\begin{cases} \sigma_r^i = \dfrac{F_i}{r^2} + 2G_i - (2A_i + \dfrac{6C_i}{r^4} + \dfrac{4D_i}{r^2})\cos(2\theta) \\ \sigma_\theta^i = -\dfrac{F_i}{r^2} + 2G_i + (2A_i + 12B_i r^2 + \dfrac{6C_i}{r^4})\cos(2\theta) \qquad (i = 2,3,4) \\ \tau_{r\theta}^i = (2A_i + 6B_i r^2 - \dfrac{6C_i}{r^4} - \dfrac{4D_i}{r^2})\sin(2\theta) \end{cases} \quad (3.3)$$

In Eq. (3.3), F_i, G_i, A_i, B_i, C_i and D_i are constants which are determined by the boundary conditions and stress and displacement continuities across the boundaries between different regions. Using the Hooke's law, we obtain the strain tensors and

displacements of the three regions given as Eq. (3.4), where u_r^i and v_θ^i represent the radial and tangential components of displacements in region i.

$$\begin{cases} \varepsilon_r^2 = \dfrac{1}{E_2^*}(\sigma_r^2 - \sigma_\theta^2) \\ \varepsilon_\theta^2 = \dfrac{1}{E_2^*}(\sigma_\theta^2 - \sigma_r^2) \\ u_r^2 = \int \varepsilon_r^2 dr \\ v_\theta^2 = \int (r\varepsilon_\theta^2 - u_r^2) d\theta \end{cases} \qquad \begin{cases} \varepsilon_r^i = \dfrac{1}{E_i}(\sigma_r^i - v_3\sigma_\theta^i) \\ \varepsilon_\theta^i = \dfrac{1}{E_3}(\sigma_\theta^i - v_3\sigma_r^i) \\ u_r^i = \int \varepsilon_r^i dr \\ v_\theta^i = \int (r\varepsilon_\theta^i - u_r^i) d\theta \end{cases} \quad (i = 3, 4) \qquad (3.4)$$

3.2 Deformations of Hollow-core PBFs Due to Different Measurands

In Section 3.1, we construct a elastic model for the hollow-core PBF. This elastic model gives general stress and strain expressions of each region of the solid-core fibre, when the fibre is subjected to symmetrical and asymmetrical measurands. In this section, we will discuss the physical deformations of the hollow-core PBF, when the fibre is subjected to different measurands such as axial strain, acoustic pressure, temperature and lateral pressure. In the four types of measurands, axial strain, acoustic pressure, and temperature variation are symmetrical measurands and they are all well-proportioned along the z-direction, while lateral pressure is an asymmetrical measurand but is also well-proportioned along the z-direction.

3.2.1 Axial Strain

In order to get deformations of the hollow-core PBF due to axial strain (ε), the constants shown in equations (3.1) and (3.2) should be determined by the boundary conditions and the stress and displacement continuities across the boundaries between different regions of the hollow-core PBF. Under the plane approximation

the boundary conditions due to axial strain and the expressions of the stress and displacement continuities may be expressed as Eq. (3.5).

$$\begin{aligned}
&\sigma_r^2\big|_{r=b} = \sigma_r^3\big|_{r=b} && (a)\\
&\sigma_r^3\big|_{r=c} = \sigma_r^4\big|_{r=c} && (b)\\
&u_r^2\big|_{r=b} = u_r^3\big|_{r=b} && (c)\\
&u_r^3\big|_{r=c} = u_r^4\big|_{r=c} && (d)\\
&\sigma_r^2\big|_{r=a} = 0 && (e)\\
&\sigma_r^4\big|_{r=d} = 0 && (f)\\
&\varepsilon_z^2 = \varepsilon_z^3 = \varepsilon_z^4 = \varepsilon && (g)
\end{aligned} \tag{3.5}$$

In Eq. (3.5), u_r^i is the radial displacement in region i, which is related to strain by Eq. (2.11). Eqs. (3.5a) and (3.5b) describe radial stress continuity across the boundaries of the regions; Eqs. (3.5c) and (3.5d) describe the radial displacement continuity across the boundaries of the regions; Eq. (3.5e) and (3.5f) mean the regions both in the fibre core and out of the fibre are air; Eq. (3.5g) is for the plane approximation [88], which ignores the end effect.

Substituting Eqs. (3.1) and (3.2) into Eq. (3.5), the constants A_i, C_i and D_i (i=2, 3, and 4), when the hollow-core PBF subjected to axial strain, can be determined by the matrix equation (3.6). By solving this equation, the constants can be obtained, and thus the stress, strain and displacement distributions of each region of the solid-core PCF, when subjected to axial strain, can be obtained.

$$\begin{bmatrix} 2 & -2 & 0 & \frac{1}{b^2} & -\frac{1}{b^2} & 0 & 0 & 0 & 0 \\ 0 & 2 & -2 & 0 & \frac{1}{c^2} & -\frac{1}{c^2} & 0 & 0 & 0 \\ 0 & \frac{2b(1-\nu_3)}{E_3} & 0 & \frac{2}{E_2^* b} & \frac{-(1+\nu_3)}{E_3 b} & 0 & \frac{\nu_2 b}{E_2} & \frac{-\nu_3 b}{E_3} & 0 \\ 0 & \frac{2c(1-\nu_3)}{E_3} & \frac{-2c(1-\nu_4)}{E_4} & 0 & \frac{-(1+\nu_3)}{E_3 c} & \frac{(1+\nu_4)}{E_4 c} & 0 & \frac{-\nu_3 c}{E_3} & \frac{\nu_4 c}{E_4} \\ 0 & 0 & 0 & 0 & 0 & 0 & \frac{1}{E_2} & 0 & 0 \\ 0 & \frac{-4\nu_3}{E_3} & 0 & 0 & 0 & 0 & 0 & \frac{1}{E_3} & 0 \\ 0 & 0 & \frac{-4\nu_4}{E_4} & 0 & 0 & 0 & 0 & 0 & \frac{1}{E_4} \\ 2 & 0 & 0 & \frac{1}{a^2} & 0 & 0 & 0 & 0 & 0 \\ 0 & 0 & 2 & 0 & 0 & \frac{1}{d^2} & 0 & 0 & 0 \end{bmatrix} \begin{bmatrix} C_2 \\ C_3 \\ C_4 \\ A_2 \\ A_3 \\ A_4 \\ D_2 \\ D_3 \\ D_4 \end{bmatrix} = \begin{bmatrix} 0 \\ 0 \\ 0 \\ 0 \\ \varepsilon \\ \varepsilon \\ \varepsilon \\ 0 \\ 0 \end{bmatrix} \tag{3.6}$$

We simulate one type of hollow-core PBF (HC-1550-02 fibre [89]) and calculate the deformation of this HC-1550-02 fibre to axial strain. This fibre has air core and an air-silica cladding with air-filling ratio of ~94%. The air-silica cladding can be approximately considered as uniform honeycomb structure. The SEM photograph of HC-1550-02 fibre is shown in Fig. 3.3 and its physical parameters are listed in Table 3.1.

Table 3.1 Physical parameters of HC-1550-02 fibre

	Pitch	*η*	*a*	*b*	*c*
Fibre	*3.8 (μm)*	*94%*	*5.45(μm)*	*35(μm)*	*60(μm)*
	d	$E_0=E_3$	E_4	$\upsilon_0=\upsilon_3$	υ_4
HC-1550-02	*110(μm)*	*72(GPa)*	*0.5(GPa)*	*0.17*	*0.37*

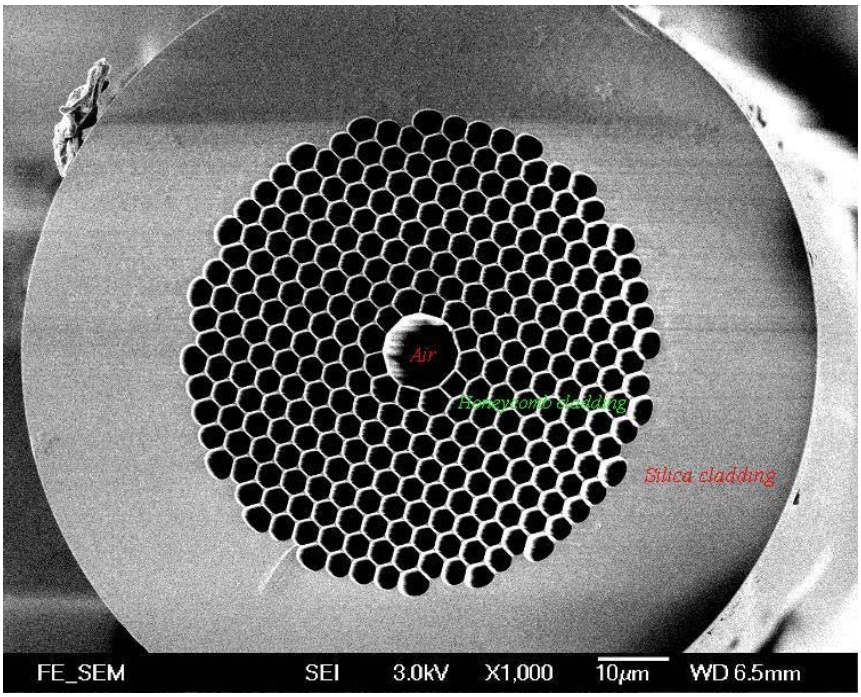

Fig 3.3 SEM photograph of one type of hollow-core PBF (HC-1550-02).

Using the physical parameters shown in Table 3.1, the deformation of hollow-core PBF (HC-1550-02) due to axial strain can be calculated by using this theoretical model. For example, we plotted the radial displacements u_r^i of each region of the HC-1550-02 as the function of distance from the fibre centre in Fig. 3.4, when the fibre is subjected to axial strain of -10^{-3} (ε).

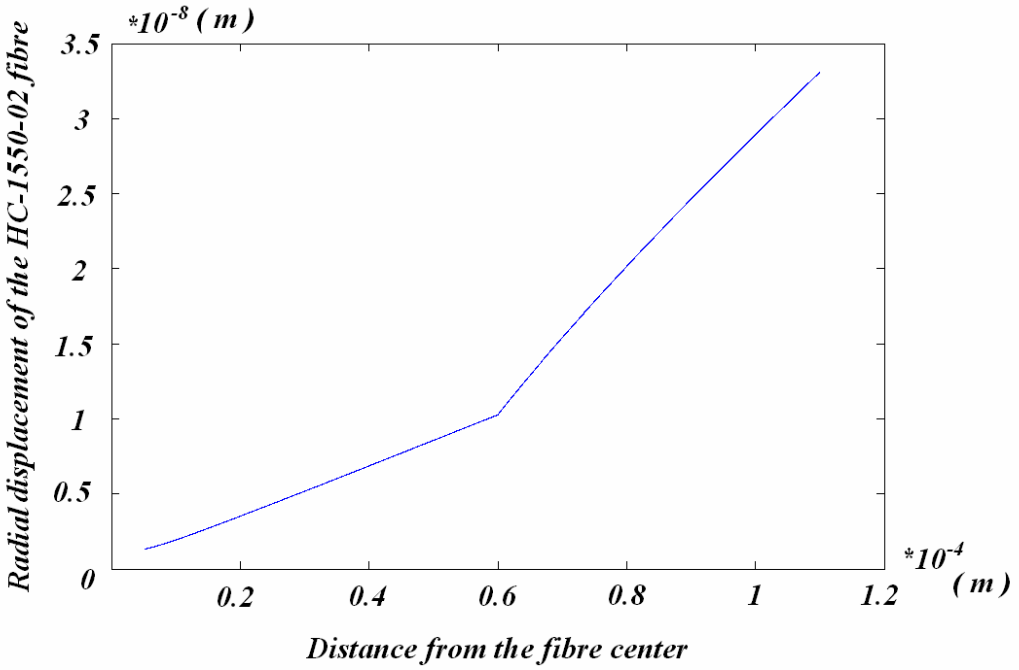

Fig. 3.4 Radial displacement as the function of distance from the fibre centre for the HC-1550-02 fibre, when the fibre is subjected to axial strain of -10^{-3} (ε).

It can be seen in Fig. 3.4 that the radial displacements of the fibre's air-silica inner cladding and silica outer cladding increase linearly with the increasing of the distance from the fibre centre. This is because those two regions have the same material of silica. Thus when the fibre is subjected to axial strain, the radial strains of the two regions keep a similar value. Compared with silica material, the material of the jacket is one type of polymers which is much more flexible than the silica, thus in this region of polymer jacket, the radial strain is larger than the other two regions.

3.2.2 Acoustic Pressure

The constants shown in Equations (3.1) and (3.2), when the fibre is subjected to acoustic pressure (*-dP*), are also determined by the boundary conditions and the stress and displacement continuities across the boundaries between different regions of the hollow-core PBF. Under the plane approximation the boundary conditions due

to acoustic pressure and the expressions of the stress and displacement continuities may be expressed as Eq. (3.7).

$$
\begin{aligned}
&\sigma_r^2\big|_{r=b} = \sigma_r^3\big|_{r=b} && (a)\\
&\sigma_r^3\big|_{r=c} = \sigma_r^4\big|_{r=c} && (b)\\
&u_r^2\big|_{r=b} = u_r^3\big|_{r=b} && (c)\\
&u_r^3\big|_{r=c} = u_r^4\big|_{r=c} && (d)\\
&\sigma_r^2\big|_{r=a} = 0 && (e)\\
&\sigma_r^4\big|_{r=d} = -dP && (f)\\
&\varepsilon_z^2 = \varepsilon_z^3 = \varepsilon_z^4 && (g)\\
&-(dP)d^2 = \sigma_z^2(b^2 - a^2) && \\
&+\sigma_z^3(c^2 - b^2) + \sigma_z^4(d^2 - c^2) && (h)
\end{aligned}
\qquad (3.7)
$$

Eqs. (3.7*a*) and (3.7*b*) describe radial stress continuity across the boundaries of the regions; Eqs. (3.7*c*) and (3.7*d*) describe the radial displacement continuity across the boundaries of the regions; Eq. (3.7*e*) means the core of the fibre is air, Eqs. (3.7*f*) and (3.7*h*) are the hydrostatic conditions, and Eq. (3.7*g*) is for the plane approximation [88].

Substituting Eqs. (3.1), (3.2) and (2.11) into the boundary conditions, the constants A_i, C_i and D_i (i=2, 3, and 4), when the hollow-core PBF subjected to acoustic pressure, can be determined by the matrix equation (3.8). By solving this equation, the constants can be obtained, and thus the stress, strain and displacement distributions of each region of the hollow-core PBF, when subjected to acoustic pressure, can be obtained.

$$\begin{bmatrix} 2 & -2 & 0 & \frac{1}{b^2} & -\frac{1}{b^2} & 0 & 0 & 0 & 0 \\ 0 & 2 & -2 & 0 & \frac{1}{c^2} & -\frac{1}{c^2} & 0 & 0 & 0 \\ 0 & \frac{2b(1-\nu_3)}{E_3} & 0 & \frac{2}{E_2^* b} & \frac{-(1+\nu_3)}{E_3 b} & 0 & \frac{\nu_2 b}{E_2} & \frac{-\nu_3 b}{E_3} & 0 \\ 0 & \frac{2c(1-\nu_3)}{E_3} & \frac{-2c(1-\nu_4)}{E_4} & 0 & \frac{-(1+\nu_3)}{E_3 c} & \frac{(1+\nu_4)}{E_4 c} & 0 & \frac{-\nu_3 c}{E_3} & \frac{\nu_4 c}{E_4} \\ 0 & \frac{4\nu_3}{E_3} & 0 & 0 & 0 & 0 & \frac{1}{E_2} & -\frac{1}{E_3} & 0 \\ 0 & 0 & \frac{4\nu_4}{E_4} & 0 & 0 & 0 & \frac{1}{E_2} & 0 & -\frac{1}{E_4} \\ 0 & 0 & 0 & 0 & 0 & 0 & (b^2-a^2)(c^2-b^2)(d^2-c^2) & & \\ 2 & 0 & 0 & \frac{1}{a^2} & 0 & 0 & 0 & 0 & 0 \\ 0 & 0 & 2 & 0 & 0 & \frac{1}{d^2} & 0 & 0 & 0 \end{bmatrix} \begin{bmatrix} C_2 \\ C_3 \\ C_4 \\ A_2 \\ A_3 \\ A_4 \\ D_2 \\ D_3 \\ D_4 \end{bmatrix} = \begin{bmatrix} 0 \\ 0 \\ 0 \\ 0 \\ 0 \\ 0 \\ -dPd^2 \\ 0 \\ -dP \end{bmatrix} \tag{3.8}$$

The deformations of one type of hollow-core PBF (HC-1550-02 fibre), when it is subjected to acoustic pressure, are calculated. The parameters and the SEM photograph of this HC-1550-02 fibre are shown in Table 2.1 and Fig. 3.3 respectively.

The radial displacements u_r^i of each region of the HC-1550-02 as the function of distance from the fibre centre are shown in Fig. 3.5, when the fibre is subjected to acoustic pressure of -1 (Pa). It can be seen in Fig. 3.5 that the radial displacements of the air-silica inner cladding and the silica outer cladding are much smaller than the displacement of the polymer jacket. This is because, compared with silica material, polymer is much more flexible.

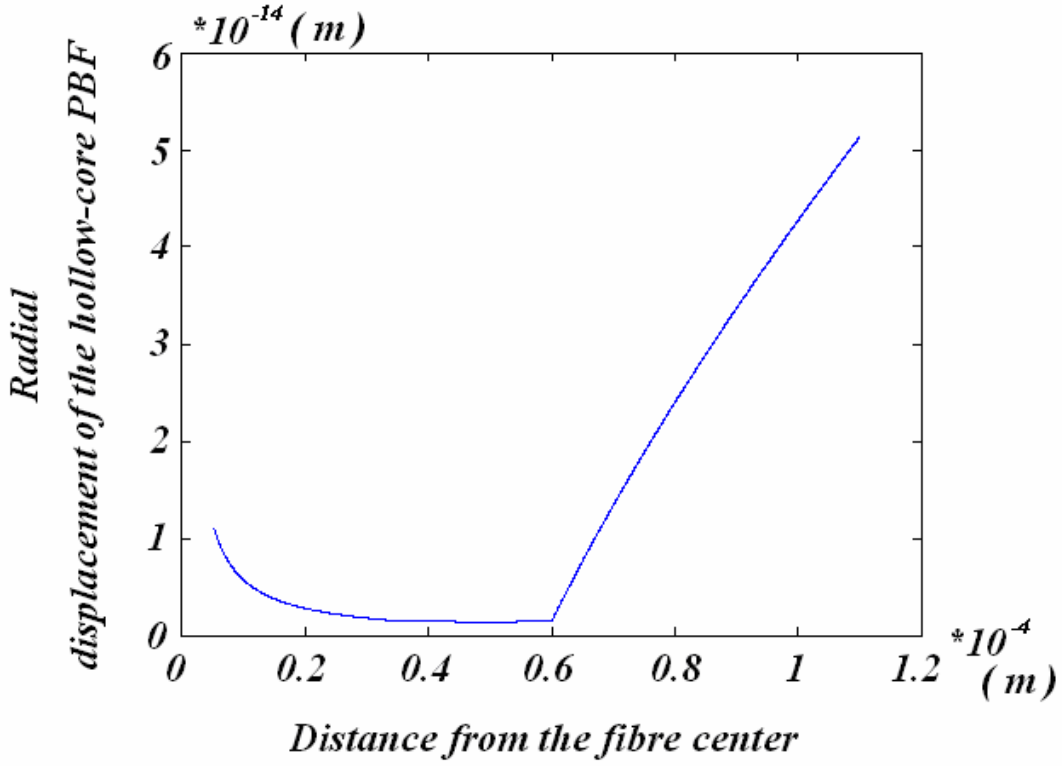

Fig. 3.5 Radial displacement as the function of distance from the fibre centre for the HC-1550-02 fibre, when the fibre is subjected to acoustic pressure of -1 (Pa).

3.2.3 Temperature

When the hollow-core PBF is subjected to temperature variations of (ΔT), the stress expressions of regions are also shown as Eqs. (3.1). However, the strain expressions of the hollow-core PBF due to temperature variations are different with the strain equations due to axial strain or acoustic pressure. The thermal expansion terms ($\alpha_i \Delta T$) should be added into the strain expression of each region as expressed as Eq. (3.9), where α_i (i=2, 3 and 4) are the thermal expansion coefficients of the three regions.

$$\begin{cases} \varepsilon_r^2 = \dfrac{2A_2}{E_2^* r^2} - v_2 \dfrac{D_2}{E_2} + \alpha_2 \Delta T \\ \varepsilon_\theta^2 = -\dfrac{2A_2}{E_2^* r^2} - v_2 \dfrac{D_2}{E_2} + \alpha_2 \Delta T \\ \varepsilon_z^2 = \dfrac{D_2}{E_2} + \alpha_2 \Delta T \end{cases} \tag{3.9}$$

$$\begin{cases} \varepsilon_r^i = \dfrac{1}{E_i}[(1+v_i)\dfrac{A_i}{r^2} + 2(1-v_i)C_i - v_i D_i] + \alpha_i \Delta T \\ \varepsilon_\theta^i = \dfrac{1}{E_i}[-(1+v_i)\dfrac{A_i}{r^2} + 2(1-v_i)C_i - v_i D_i] + \alpha_i \Delta T \qquad (i = 3,4) \\ \varepsilon_z^i = \dfrac{1}{E_i}(D_i - 4v_i C_i) + \alpha_i \Delta T \end{cases}$$

$$\begin{aligned} &\sigma_r^2\big|_{r=b} = \sigma_r^3\big|_{r=b} && (a) \\ &\sigma_r^3\big|_{r=c} = \sigma_r^4\big|_{r=c} && (b) \\ &u_r^2\big|_{r=b} = u_r^3\big|_{r=b} && (c) \\ &u_r^3\big|_{r=c} = u_r^4\big|_{r=c} && (d) \\ &\sigma_r^2\big|_{r=a} = 0 && (e) \\ &\sigma_r^4\big|_{r=d} = 0 && (f) \\ &\varepsilon_z^2 = \varepsilon_z^3 = \varepsilon_z^4 && (g) \\ &0 = \sigma_z^2(b^2 - a^2) \\ &+\sigma_z^3(c^2 - b^2) + \sigma_z^4(d^2 - c^2) && (h) \end{aligned} \tag{3.10}$$

The constants are also determined by the boundary conditions and the stress and the displacement continuities across the boundaries among different regions of the hollow-core PBF. Under the plane approximation, the boundary conditions due to temperature variations and the expressions of the stress and displacement continuities may be expressed as Eq. (3.10).

Eqs. (3.10*a*) and (3.10*b*) describe radial stress continuity across the boundaries of the regions; Eqs. (3.10*c*) and (3.10*d*) describe the radial displacement continuity across

the boundaries of the regions; Eq. (3.10*e*) expresses the core of the fibre is air, Eqs. (3.10*f*) and (3.10*h*) means the pressure outside the fibre is zero, and Eq. (2.10*g*) is for the plane approximation [88].

Substituting Eqs. (3.1), (3.9), and (2.11) into the boundary conditions, the constants A_i, C_i and D_i (i=2, 3, and 4), when the hollow-core PBF subjected to temperature variations of ΔT, can be determined by the matrix equation (3.11). By solving this equation, the constants can be obtained, and thus the stress, strain and displacement distributions of each region of the hollow-core PBF, when subjected to temperature variations, can be obtained.

$$\begin{bmatrix}
2 & -2 & 0 & \frac{1}{b^2} & -\frac{1}{b^2} & 0 & 0 & 0 & 0 \\
0 & 2 & -2 & 0 & \frac{1}{c^2} & -\frac{1}{c^2} & 0 & 0 & 0 \\
0 & \frac{2b(1-\nu_3)}{E_3} & 0 & \frac{2}{E_2^* b} & \frac{-(1+\nu_3)}{E_3 b} & 0 & \frac{\nu_2 b}{E_2} & \frac{-\nu_3 b}{E_3} & 0 \\
0 & \frac{2c(1-\nu_3)}{E_3} & \frac{-2c(1-\nu_4)}{E_4} & 0 & \frac{-(1+\nu_3)}{E_3 c} & \frac{(1+\nu_4)}{E_4 c} & 0 & \frac{-\nu_3 c}{E_3} & \frac{\nu_4 c}{E_4} \\
0 & \frac{4\nu_3}{E_3} & 0 & 0 & 0 & 0 & \frac{1}{E_2} & -\frac{1}{E_3} & 0 \\
0 & 0 & \frac{4\nu_4}{E_4} & 0 & 0 & 0 & \frac{1}{E_2} & 0 & -\frac{1}{E_4} \\
0 & 0 & 0 & 0 & 0 & 0 & (b^2-a^2)(c^2-b^2)(d^2-c^2) & & \\
2 & 0 & 0 & \frac{1}{a^2} & 0 & 0 & 0 & 0 & 0 \\
0 & 0 & 2 & 0 & 0 & \frac{1}{d^2} & 0 & 0 & 0
\end{bmatrix}
\begin{bmatrix} C_2 \\ C_3 \\ C_4 \\ A_2 \\ A_3 \\ A_4 \\ D_2 \\ D_3 \\ D_4 \end{bmatrix}
=
\begin{bmatrix} 0 \\ 0 \\ (\alpha_2-\alpha_3)\Delta T b \\ (\alpha_4-\alpha_3)\Delta T c \\ (\alpha_3-\alpha_2)\Delta T \\ (\alpha_4-\alpha_2)\Delta T \\ 0 \\ 0 \\ 0 \end{bmatrix} \tag{3.11}$$

The deformations of the hollow-core PBF (HC-1550-02), when it is subjected to temperature variation, are simulated by using this theoretical model. The parameters and the SEM photograph of this HC-1550-02 fibre are shown in Table 3.1 and Fig. 3.3 respectively. The thermal expansion coefficients of silica material and polymer material of HC-1550-02 fibre are $0.55*10^{-6}$ and $8*10^{-5}$ (ε/K) respectively.

The radial displacements u_r^i of each region of the HC-1550-02 as the function of distance from the fibre centre are shown in Fig. 3.6, when the fibre is subjected to temperature variation of 1 (K). It can be seen in Fig. 3.6 that the radial displacement of the polymer jacket region are much larger than the displacements of the other three regions of the fibre. This is because the thermal expansion coefficient of polymer material is much larger than silica material.

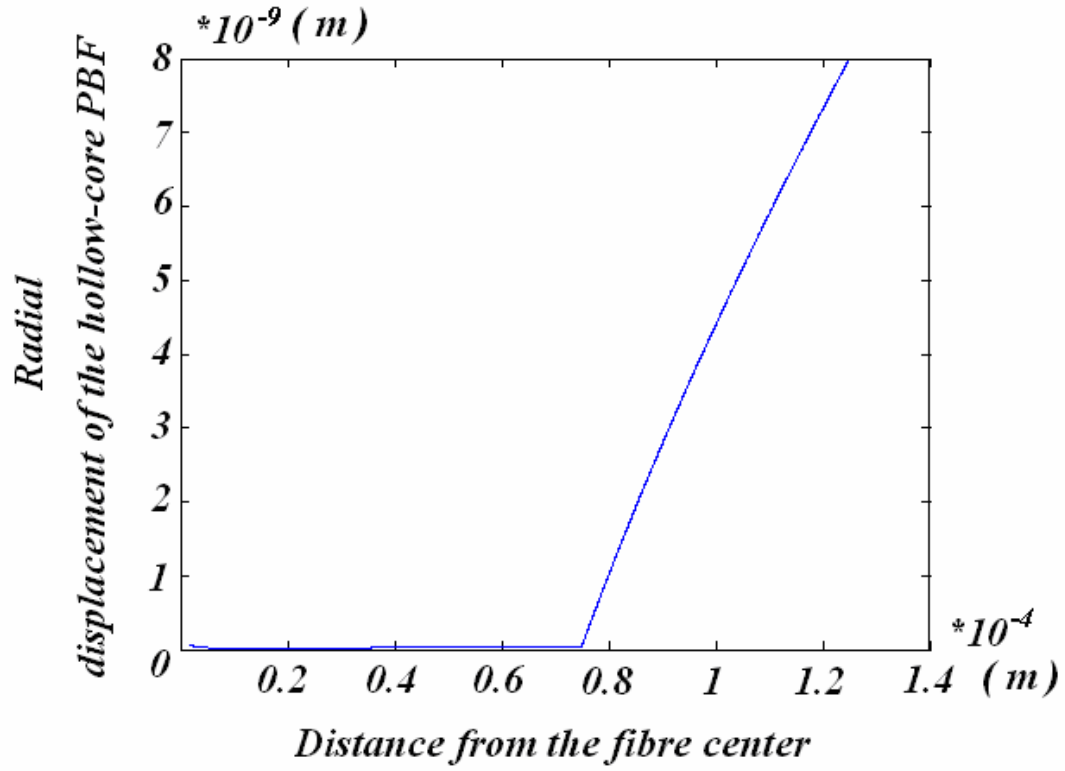

Fig. 3.6 Radial displacement as the function of distance from the fibre centre for the HC-1550-02 fibre, when the fibre is subjected to temperature variation of 1 (K).

3.2.4 Lateral Pressure

Unlike axial strain, acoustic pressure, and temperature, lateral pressure is an asymmetric measurand. Thus the stress and strain expressions of each region of the hollow-core PBF, when subjected to lateral pressure, can be written as equations (3.3) and (3.4).

The constants in equations (3.3) and (3.4) are also determined by the boundary conditions and the stress and the displacement continuities across the boundaries among different regions of the hollow-core PBF. Under the plane approximation, the boundary conditions due to lateral pressure and the expressions of the stress and displacement continuities may be expressed as Eq. (3.12), where v_θ^i is the tangential displacement of region *i* as shown in Eq. (3.11*m*) [88].

$$
\begin{aligned}
&\sigma_r^4\big|_{r=d} = P\cos^2\theta && (a)\\
&\sigma_\theta^4\big|_{r=d} = P\sin^2\theta && (b)\\
&\sigma_r^2\big|_{r=a} = 0 && (c)\\
&\tau_{r\theta}^2\big|_{r=a} = 0 && (d)\\
&\sigma_r^2\big|_{r=b} = \sigma_r^3\big|_{r=b} && (e)\\
&\sigma_r^3\big|_{r=c} = \sigma_r^4\big|_{r=c} && (f)\\
&\tau_{r\theta}^2\big|_{r=b} = \tau_{r\theta}^3\big|_{r=b} && (g)\\
&\tau_{r\theta}^3\big|_{r=c} = \tau_{r\theta}^4\big|_{r=c} && (h)\\
&u_r^2\big|_{r=b} = u_r^3\big|_{r=b} && (i)\\
&u_r^3\big|_{r=c} = u_r^4\big|_{r=c} && (j)\\
&v_\theta^2\big|_{r=b} = v_\theta^3\big|_{r=b} && (k)\\
&v_\theta^3\big|_{r=c} = v_\theta^4\big|_{r=c} && (l)\\
&v_\theta^i = \int (r\varepsilon_\theta^i - u_r^i)d\theta && (m)
\end{aligned}
\qquad (3.12)
$$

Eqs. (3.12*a*) and (3.12*b*) mean the fibre is subjected to lateral pressure; Eqs. (3.12*c*) and (3.12*d*) mean the core of the fibre is air; Eqs. (3.12*e*), (3.12*f*), (3.12*g*) and (3.12*h*) describe the radial and shear stress continuities across boundaries of the regions; and Eqs. (3.12*i*), (3.12*j*), (3.12*k*) and (3.12*l*) describe the radial and tangential displacement continuities across the boundaries of the regions.

Substituting Eqs. (3.3), (3.4), (2.11), and (3.11*m*) into the boundary conditions, the constants A_i, B_i, C_i, D_i, F_i, G_i (i=2, 3, and 4), when the hollow-core PBF subjected to lateral pressure, can be determined, thus the stress, strain and displacement distributions of each region of the hollow-core PBF, when subjected to lateral pressure, can be obtained.

3.3 Phase Sensitivities of hollow-core PCFs to Different Measurands

As discussed in Section 2.3, the phase sensitivities of the fibre to different measurands come from two terms: the first term (S_L) is a length-term that represents the measurand-induced physical change of the fibre length, and the second term (S_n) is an index term representing the measurand-induced change of the effective refractive index of the fundamental mode.

For the hollow-core PBF, the length term of Eq. (2.19) due to different measurands, can be calculated directly by using the z-direction stress of the fibre. Unlike the solid-core PCF, the index-term of hollow-core PBF can not be determined by the strain-optic effect of the fibre core, because in the hollow-core PBF most of light travels in air. However, the measurands applied to the hollow-core PBF will induce the deformation of the hollow-core PBF's air-silica cladding and thus modify the index of the fibre material, which affects the fundamental-mode effective index.

In Section 3.2, the strain, stress and displacement distributions of each region of the hollow-core PBF due to different measurands, can be obtained. In this section, we will calculate the detail deformation in the transverse profile of the microstructure

cladding and the change of the fibre material index by using the stress, strain, and displacement distributions obtained in Section 3.2. The profile and material index changes modify the waveguide structure and hence the effective index of fundamental mode of the hollow-core PBF.

Consider an arbitrary cell centred at (r, θ), as shown in Fig 3.7(1), the in-profile stresses acting on this cell may be written as σ_r^2, σ_θ^2 and $\tau_{r\theta}^2$, as shown in Fig. 3.7(2), Fig. 3.7(3) and Fig. 3.7(4) respectively. Using the knowledge of theory of elasticity, the stresses σ_r^2, σ_θ^2 and $\tau_{r\theta}^2$ in the polar coordinates may be composed into three stress components in the rectangular coordinates $\sigma^2|_x$, $\sigma^2|_y$, and $\tau^2|_{xy}$ as given by Eq. (3.13) [88].

$$\begin{cases} \sigma^1\big|_{\mathrm{x}} = \sigma_{\mathrm{r}}^2 \cos^2(\theta) + \sigma_\theta^2 \sin^2(\theta) - 2\tau_{r\theta}^2 \sin(\theta)\cos(\theta) \\ \sigma^1\big|_{\mathrm{y}} = \sigma_{\mathrm{r}}^2 \sin^2(\theta) + \sigma_\theta^2 \cos^2(\theta) + 2\tau_{r\theta}^2 \sin(\theta)\cos(\theta) \\ \tau^1\big|_{\mathrm{xy}} = (\sigma_{\mathrm{r}}^2 - \sigma_\theta^2)\sin(\theta)\cos(\theta) + \tau_{r\theta}^2[\cos^2(\theta) - \sin^2(\theta)] \end{cases} \tag{3.13}$$

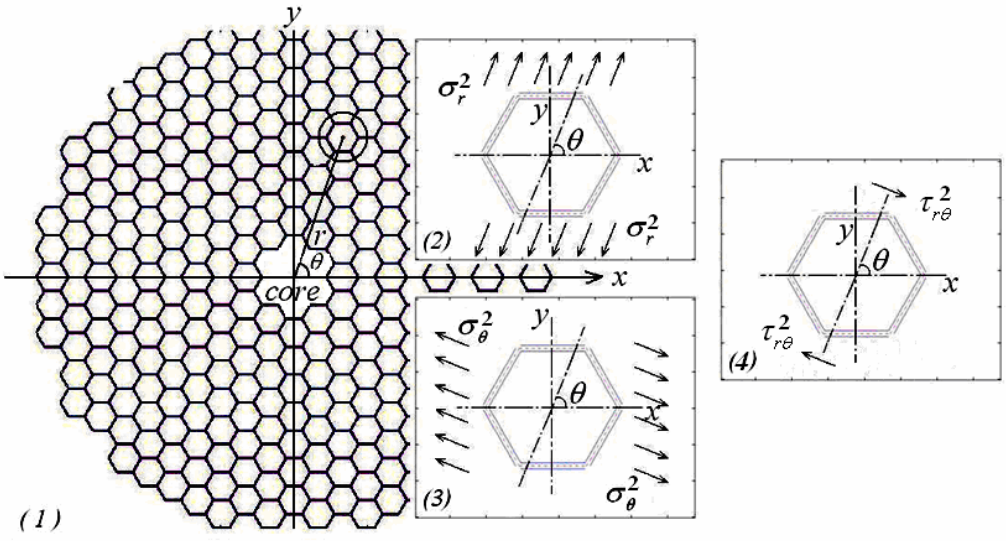

Fig. 3.7 (1) Profile configuration of the hollow-core PBF's air-silica inner cladding; (2) In-profile stress σ_r^2, on a cell of the microstructure cladding; (3) In-profile stress σ_θ^2 on a cell of the microstructure cladding; (4) In-profile shear stress $\tau_{r\theta}^2$ on a cell of the microstructure cladding

The deformation of the cell under the loads σ_r^2, σ_θ^2 and $\tau_{r\theta}^2$ is the sum of the deformations under loads $\sigma^2|_x$, $\sigma^2|_y$, and $\tau^2|_{xy}$, which can be calculated by using the knowledge of cellular solids [85]. The deformations of the cell walls (1~6) due to each of the load component are calculated respectively as follow [85]:

A. Deformation due to $\sigma^2|_x$

As Fig. 3.8 shows, when the cell under the load of $\sigma^2|_x$ deforms in a linear-elastic way, the cell walls 1 and 4 keep straight and the walls 2, 3, 5, and 6 bend by following a similar pattern. In the new set of coordinates $\{x', y'\}$, the moment of the wall 2 may be written as Eq. (3.14), where $W=(\sqrt{3}/2)el\sigma^2|_x$, l is the length of the cell wall and e is the unit depth in z-direction. The subscript "x" means the moment is caused by $\sigma^2|_x$. Then the deformation of cell wall 2 along the y' direction as the function of x' can then be obtained by double integration of Eq.(10) with respective to x' and with proper boundary conditions and expressed as Eq. (3.15)

$$M_x = -\frac{\sqrt{3}}{2} W x' \tag{3.14}$$

$$V_{y',x} = -\frac{\sqrt{3}W}{2E_0 I}\left[\frac{(x'+l/2)^3}{6} - \frac{l(x'+l/2)^2}{4} + \frac{l^3}{24}\right] \tag{3.15}$$

In equation (3.15), $I=et^3/12$, t is the thickness of the wall which is determined by the pitch and air-silica ratio of the microstructure cladding as shown in Eq. (3.16). The subscripts "y', x" means the displacement is along y'-direction and is caused by $\sigma^2|_x$.

$$t = pitch \times (1-\eta) \tag{3.16}$$

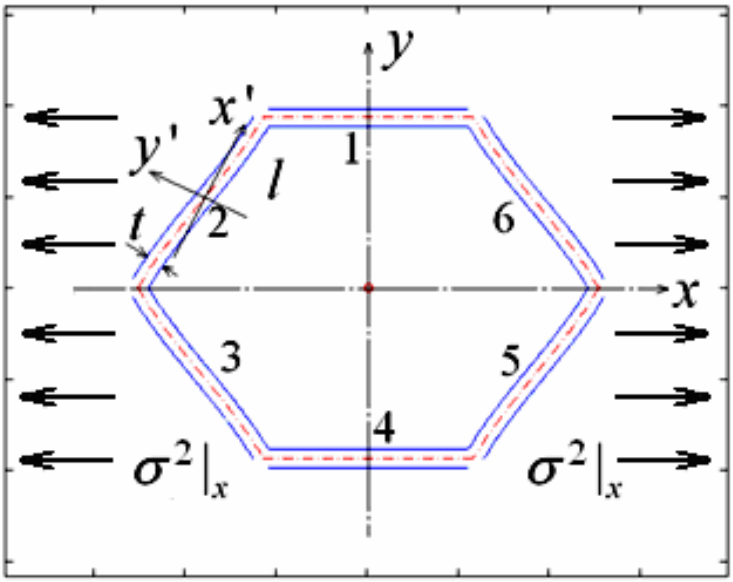

Fig. 3.8 Deformation of the cell under load $\sigma^2|_x$.

B. Deformation due to $\sigma^2|_y$

In Fig. 3.9, when the cell under the load of $\sigma^2|_y$ deforms in a linear-elastic way, the cell walls 1 and 4 keep straight and walls 2, 3, 5 and 6 bend in the similar pattern. In the new set of coordinates $\{x', y'\}$, the moment of the wall 2 can be written as Eq. (3.17), where $P=(3/2)el\sigma^2|_y$. The subscript "y" means the moment is caused by $\sigma^2|_y$. The deformation of cell wall 2 as the function of x' can be obtained from Eq. (3.17) and expressed as Eq. (3.18). In Eq. (3.18), the subscripts "y', y" means the deformation is along y'-direction and is caused by $\sigma^2|_y$.

$$M_y = \frac{1}{2}Px' \tag{3.17}$$

$$V_{y',y} = \frac{P}{2E_0 I}\left[\frac{(x'+l/2)^3}{6} - \frac{l(x'+l/2)^2}{4} + \frac{l^3}{24}\right] \tag{3.18}$$

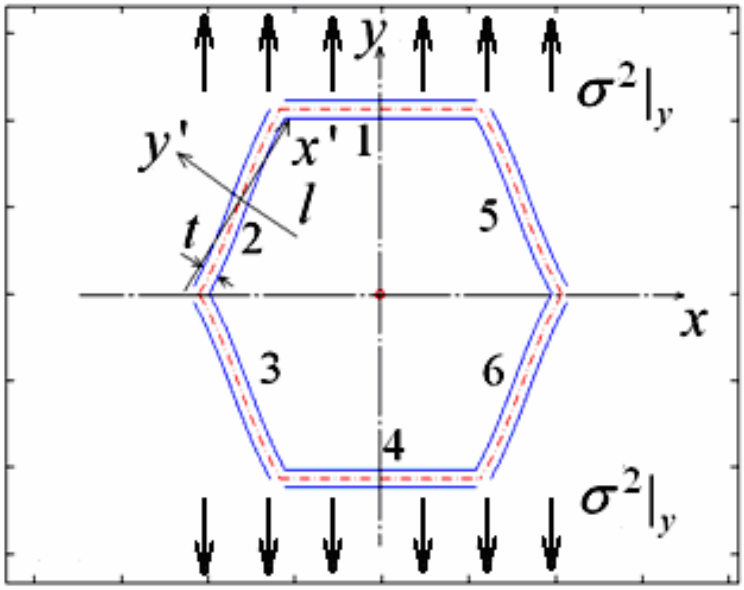

Fig. 3.9 Deformation of the cell under load $\sigma^2|_y$.

C. Deformation due to $\tau^2|_{xy}$

The deformation of the cell under shear $\tau^2|_{xy}$ is shown in Fig. 3.10. According to knowledge of cellular solids [85], when the honeycomb cell is sheared, all of cell walls bend, and walls 2, 3, 5, 6 will rotate compared with their original positions. The angle of rotation ($\Delta\psi$) can be written as Eq. (3.19)

$$\Delta\psi = \frac{Fl^2}{24E_0I} \tag{3.19}$$

In Eq. (3.19), $F=\sqrt{3}le\tau^2|_{xy}$. Because of symmetry, the cell walls 4 and 1, 5 and 2, 3 and 6 have similar bending patterns respectively. In their own new set of coordinates, the moments of walls 1, 2 and 6 can be written as Eq. (3.20).

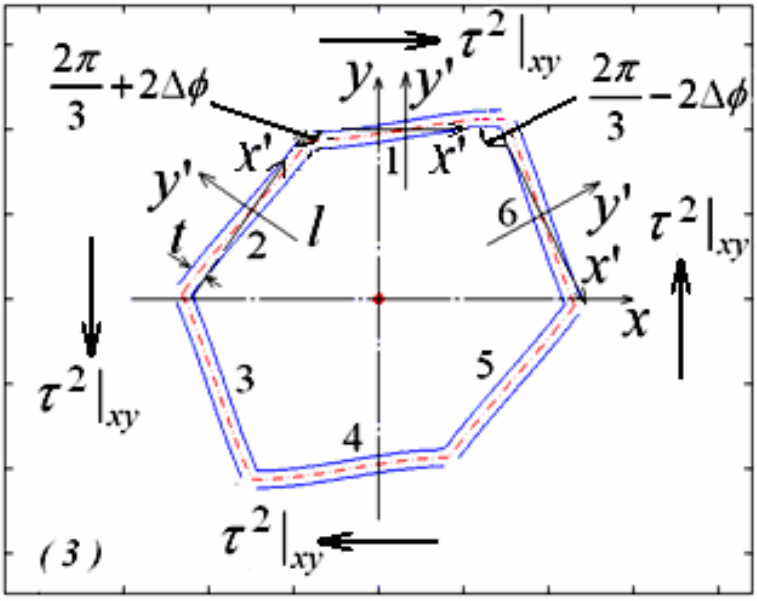

Fig. 3.10 Deformation of the cell under load $\tau^2|_{xy}$.

$$\begin{cases} M_{\tau 1} = Fx' \\ M_{\tau 2} = -\dfrac{F}{2}x' \\ M_{\tau 6} = -\dfrac{F}{2}x' \end{cases} \tag{3.20}$$

The deformations of walls 1, 2 and 6 in the *y'*-direction as the function of *x'* can be calculated from Eq. (3.20) and expressed as Eq. (3.21). The subscripts *"y', τ_i"* means the deformation is along *y'*-direction and is caused by the shear $\tau^2|_{xy}$ acting on the "i^{th}" wall. It should be emphasized that the coordinates $\{x', y'\}$ for different walls are different and the deformation for a particular wall is expressed in the coordinates of that wall.

$$V_{y',\tau 1} = \frac{F}{E_0 I}\left[\frac{(x'+l/2)^3}{6} - \frac{l(x'+l/2)^2}{4} + \frac{l^3}{24}\right]$$
$$V_{y'\tau 2} = \frac{F}{E_0 I}\left[\frac{(x'+l/2)^3}{6} - \frac{l(x'+l/2)^2}{4} + \frac{l^3}{24}\right] \quad (3.21)$$
$$V_{y',\tau 6} = \frac{F}{E_0 I}\left[\frac{(x'+l/2)^3}{6} - \frac{l(x'+l/2)^2}{4} + \frac{l^3}{24}\right]$$

Using Eqs. (3.15), (3.18) and (3.21), we can obtain the deformations of one single cell due to the loads $\sigma^2|_x$, $\sigma^2|_y$, and $\tau^2|_{xy}$. The total deformation of this cell to the measurand is the sum of those deformations, and the deformations of all the cells in the hollow-core PBF's microstructure cladding can be obtained by following a similar process. By using the displacement expressions of the air-silica cladding, the position of each cell centre can be obtained. With the deformations and centre positions of all the cells in the hollow-core PBF's microstructure cladding, we can plot the new transverse profile of the deformed fibre.

As shown in Fig. 3.7(1), all cells in the fibre's microstructure cladding, except the ones in the innermost ring, are regarded as ideal honeycomb hexagons. For the 12 cells near the core surround, 6 of them keep the original hexagonal shape while the other 6 are modified with the two sides of the hexagons are replaced by a straight line that connects the two corners of the original hexagons [90]. The core surround is approximated from the actual core shape shown in Fig. 3.3 and is formed by silica sandwiched in-between the sides of the innermost cells and a circle centered at the fibre axis and with a radius of $r=a+u_r^2|_{r=a}$. The strain and displacement of the core surround are calculated directly from Eqs. (3.1), (3.2), (3.3), (3.4), (2.11) and (3.12); while Eqs. (3.15), (3.18), and (3.21) are also needed to obtain the deformations of the cell walls.

In addition to the change of the hollow-core PBF's transverse geometry profile, the refractive index distribution of the material is also modified by the measurand through strain-optic effect. The strain distribution within the wall cross-section is complex due to the compression (elongation) and the bending of walls. For simplicity, we approximately regard the strain distribution is uniform along the direction normal to the wall (i.e., *y'*-axis) and equal to the strain along the centre-line of the wall (i.e., along *x'*-axis). The walls that form the core-surround are treated in the same way as the walls of a uniform hexagon in the air-silica cladding. The strain-optic effect appears as a change in the optical indicatrix of the silica material as shown in Eq. (3.22) [91].

$$\Delta\left(\frac{1}{n^2}\right)_i = \sum_{j=1}^{6} p_{ij} \begin{bmatrix} \frac{\sigma_r^2}{E_2} - v_0 \frac{\sigma_\theta^2}{E_2} - v_0 \varepsilon_z^2 \\ \frac{\sigma_\theta^2}{E_2} - v_0 \frac{\sigma_r^2}{E_2} - v_0 \varepsilon_z^2 \\ \varepsilon_z^2 \\ 0 \\ 0 \\ 0 \end{bmatrix} \tag{3.22}$$

In Eq. (3.22), p_{ij} is the strain-optic tensor, the subscripts are in the standard contracted notation, and n_0 is the original reflection index of the material. Silica material is a homogeneous isotropic medium and has only two numerical values p_{11} and p_{12}, thus the changes in the optical indices in the r, θ and z directions can be written as Eq. (3.23).

$$\Delta n_r = -\frac{1}{2} n_0^3 [(1-\nu_2) p_{12} \varepsilon_z^2 - \nu_2 p_{11} \varepsilon_z^2 + \frac{\sigma_r^2 - \nu_0 \sigma_\theta^2}{E_2} p_{11} + \frac{\sigma_\theta^2 - \nu_0 \sigma_r^2}{E_2} p_{12}]$$
$$\Delta n_\theta = -\frac{1}{2} n_0^3 [(1-\nu_2) p_{12} \varepsilon_z^2 - \nu_2 p_{11} \varepsilon_z^1 + \frac{\sigma_\theta^2 - \nu_0 \sigma_r^2}{E_2} p_{11} + \frac{\sigma_r^2 - \nu_0 \sigma_\theta^2}{E_2} p_{12}] \quad (3.23)$$
$$\Delta n_z = -\frac{1}{2} n_0^3 [\varepsilon_z^2 (p_{11} - 2\nu_2 p_{12}) + 2\frac{\sigma_r^2 - \sigma_\theta^2}{E_2} p_{12}]$$

Now, we have obtained the in-profile structure and material index distribution of the hollow-core PBF under difference measurands. The deformed profile and material index distribution are then imported into the finite element analysis solver to compute the fundamental mode profile and effective index of the hollow-core PBF [93 and 94].

3.3.1 Axial Strain

The normalized phase sensitivity of the hollow-core PCF to axial strain may be expressed as Eq. (2.20). For the normalized phase sensitivity to axial strain, the length term is one, and the index term of Eq. (2.20) is mainly caused by the geometric deformation of the air-silica cladding and the change of the silica material. The index term, when the hollow-core PBF is subjected to axial strain, can be written as Eq. (3.24).

$$S_n = \frac{1}{n_{eff}} \frac{dn_{eff}}{\varepsilon} \quad (3.24)$$

We simulated the effective index variation of the HC-1550-02 fibre when it is subjected to axial strain. Table 3.1 and Fig. 3.3 shows the physical parameters and the SEM photograph of the HC-1550-02 fibre respectively. We applied the model described in Section 3.2 and 3.3 to simulate the HC-1550-02 fibre, when it is subjected to axial strain of ε=0.3. The deformed transverse profile of the hollow-core

PBF is calculated and plotted in Fig. 3.11. In Fig. 3.11, the black pattern shows the deformed profile, while the red one shows the original profile of the hollow-core PBF.

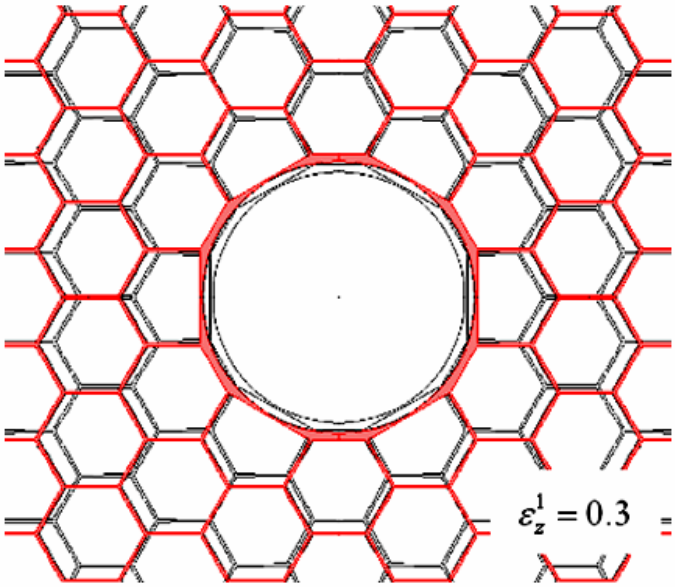

Fig. 3.11 Deformed profile (black) of the hollow-core PBF, when the fibre is under the axial strain of ε=0.3. For comparison, the original profile is shown in red.

Fig. 3.12 shows the calculated intensity profiles and refractive indices of the fundamental modes of HC-1550-02 under three different axial strain levels. The results shown in Fig. 3.12 are obtained from a model with four rings of air-silica cladding cells. No significant difference is found in the results from three and five rings models, because most of the light intensity is confined in the hollow-core and the cells near the core [92].

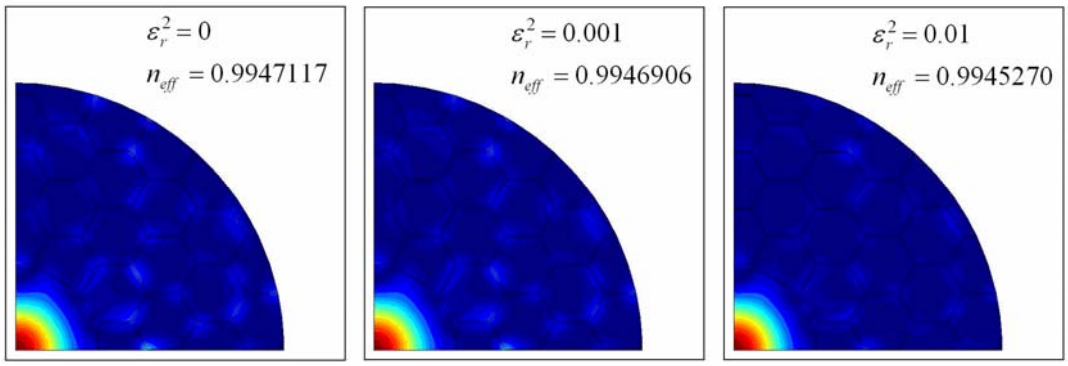

Fig. 3.12 Calculated intensity profiles and effective refractive indices of the fundamental mode of HC-1550-02 fibre under different axial strains.

The change of the fundamental mode index is attributed to two factors: 1) the contribution of the hollow-core PBF geometry deformation $(dn_{eff}/d\varepsilon)_D$; 2) the contribution of the hollow-core PBF material index modification $(dn_{eff}/d\varepsilon)_N$, as expressed in Eq. (3.25). Importing the model discussed in Section 3.2 and 3.3 into the finite element solver, the variation of the refractive index n_{eff} due to geometry deformation, material index, and their combination as the functions of the axial strain can be obtained. The results are shown in Fig. 3.13.

$$\frac{dn_{eff}}{n_{eff} d\varepsilon} = (dn_{eff} / d\varepsilon)_D + (dn_{eff} / d\varepsilon)_N \tag{3.25}$$

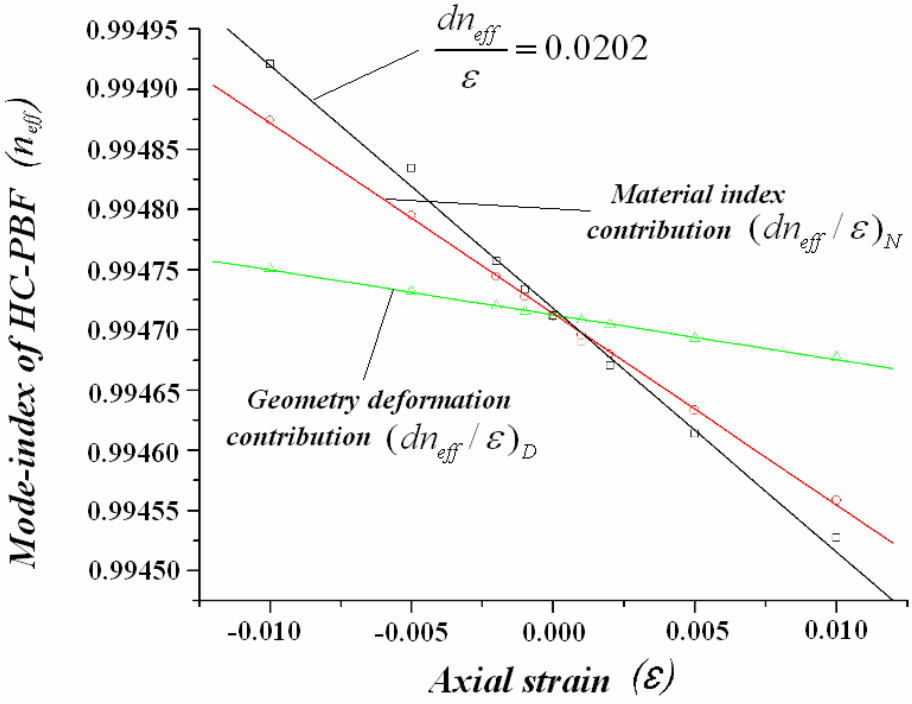

Fig. 3.13 Hollow-core PBF's fundamental mode effective index (n_{eff}) as the function of axial strain.

From Fig. 3.13, the slopes of the curves, i.e., $(dn_{eff}/d\varepsilon)_D$, $(dn_{eff}/d\varepsilon)_N$, and $dn_{eff}/d\varepsilon$, are calculated to be ~-0.0039 (ε^{-1}), ~-0.0162 (ε^{-1}), and -0.0202 (ε^{-1}), respectively. Obviously when the hollow-core PBF is subjected to axial strain, the material index contribution is dominant factor and $(dn_{eff}/d\varepsilon)_N$ is about 4 times larger than $(dn_{eff}/d\varepsilon)_D$. This is because the hollow-core PBF's in-profile deformation due to axial strain is considerable smaller than its axial deformation. The material index change is mainly due to the relatively large strain along the axial direction of the fibre. Fig. 3.14 shows the calculated ε_r^2 of the hollow-core PBF as the function of r, when the fibre is subjected to axial strain of 10^{-3} (ε).

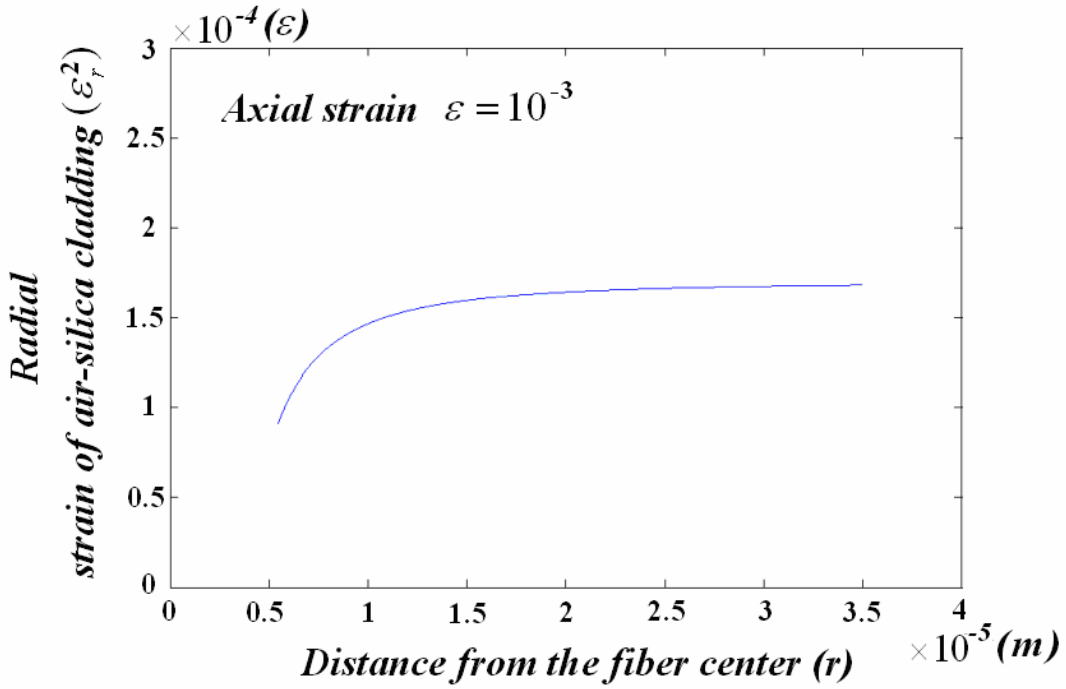

Fig. 3.14 Radial strain ε_r^2 in the hollow-core PBF microstructure cladding, when the fibre is subjected to axial strain of 10^{-3} (ε).

Substituting the calculated $dn_{eff}/d\varepsilon$ into Eq. (2.20), the S_L, S_n and S of HC-1550-02 fibre to axial strain can be estimated to be 1 (ε^{-1}), -0.0203 (ε^{-1}), and 0.9797 (ε^{-1}) respectively.

3.3.2 Acoustic Pressure

The normalized phase sensitivity of the hollow-core PCF to acoustic pressure may be expressed as Eq. (2.23). For the normalized phase sensitivity to axial strain, the length term of Eq. (2.23) can be calcualted directly by using the acoustic pressure-induced *z*-direction stress ε_z^2, which is obtained in Section 3.2.2. For the HC-1550-02 fibre, the length term can be obtained as $S_L = -2.68*10^{-11}$ (Pa^{-1}). The index term of Eq. (2.23) is mainly caused by the geometric deformation of the air-silica cladding and the change of the silica material. The index term, when the hollow-core PBF is subjected to acoustic pressure, can be written as Eq. (3.26).

$$S_n = \frac{1}{n_{eff}} \frac{dn_{eff}}{dP} \tag{3.26}$$

We simulated the phase sensitivity of the HC-1550-02 fibre when it was subjected to acoustic pressure. Table 3.1 and Fig. 3.3 shows the physical parameters and the SEM photograph of the HC-1550-02 fibre respectively. We applied the model described in Section 3.2 and 3.3 to simulate the HC-1550-02 fibre, when it was subjected to acoustic pressure of $dP = 10^8$ (Pa). The transverse profile of the hollow-core PBF was calculated and plotted in Fig. 3.15. In Fig. 3.15, the black pattern shows the deformed profile, while the red one shows the original profile of the hollow-core PBF.

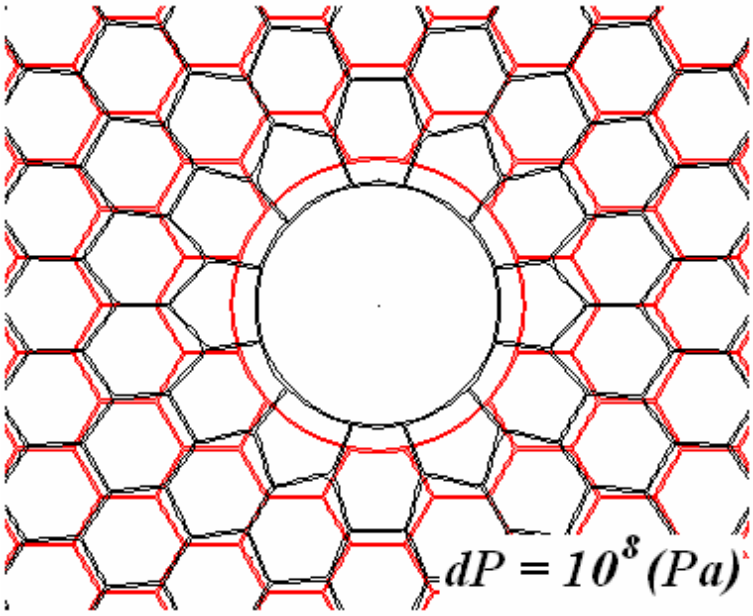

Fig. 3.15 Deformed profile (black) of the hollow-core PBF, when the fibre is under the acoustic pressure of $dP = 10^8$ (Pa). For comparison, the original profile is shown in red.

When subjected to acoustic pressure, the change of the fundamental mode index of the hollow-core PBF is attributed to two factors: 1) the contribution of the hollow-core PBF geometry deformation $(dn_{eff}/dP)_D$; 2) the contribution of the hollow-core

PBF material index modification $(dn_{eff}/dP)_N$, as expressed in Eq. (3.27). Importing the model discussed in Section 3.2 and 3.3 into the finite element solver, the variation of the refractive index n_{eff} due to geometry deformation, material index, and their combination as the functions of the acoustic pressure (dP) can be obtained. The results are shown in Fig. 3.16.

$$\frac{dn_{eff}}{n_{eff}dP} = (dn_{eff}/dP)_D + (dn_{eff}/dP)_N \tag{3.27}$$

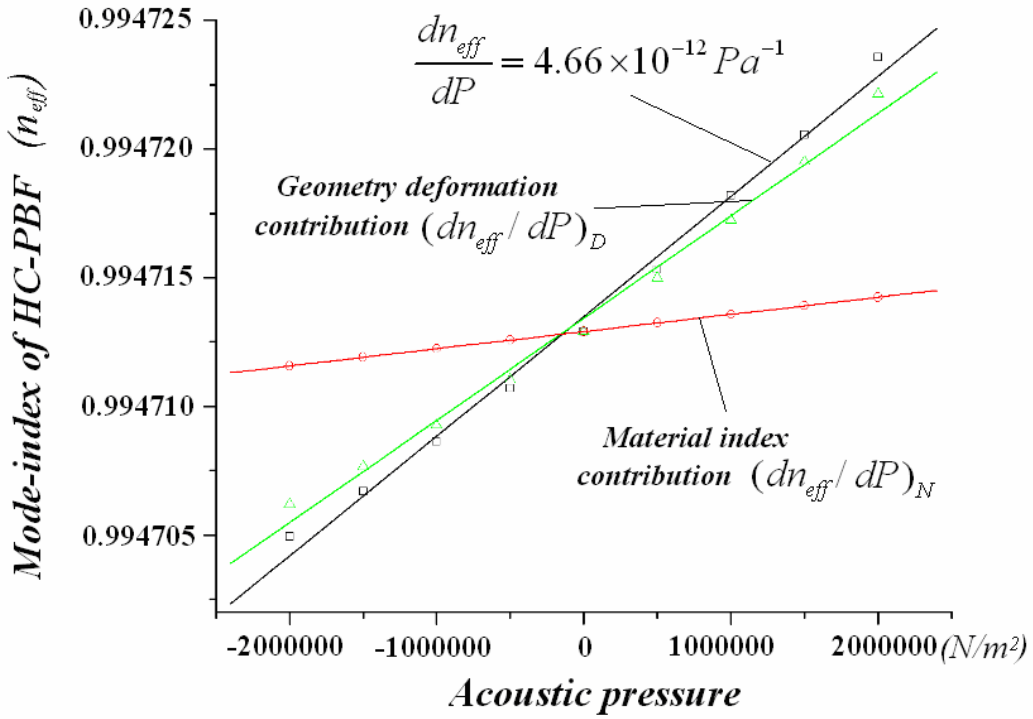

Fig. 3.16 Hollow-core PBF's fundamental mode effective index (n_{eff}) as the function of acoustic pressure (dP).

From Fig. 3.16, $(dn_{eff}/dP)_D$, $(dn_{eff}/dP)_N$ and $dn_{eff}/(n_{eff}dP)$ for HC-1550-02 fibre are estimated to be ~3.97*10^{-12} (Pa^{-1}), ~6.66*10^{-13} (Pa^{-1}) and ~4.64*10^{-12} (Pa^{-1}), respectively. The geometry deformation contribution $(dn_{eff}/dP)_D$ is dominant and is about 6 times larger than material index contribution $(dn_{eff}/dP)_N$. This is because that the acoustic pressure is applied to both axial and radial directions, and the simulation

shows that in the fibre's air-silica inner cladding, the radial strain (ε_r^2) increases as r decreases and reaches its maximum when approaching to the core-cladding interface. Fig. 3.17 shows ε_r^2 as function of r when the hollow-core PBF is subjected to acoustic pressure of $dP = 10^3$ (Pa). The large deformation near the core region of air-silica cladding makes the fibre have a high $(dn_{eff}/dP)_D$. And as discussed in Section 3.3, this large deformation in the fibre's air-silica inner cladding mainly comes from the bending of the honeycomb walls, but not the silica material strain. S, S_L and S_n can be calculated from Eq. (2.23) to be -2.216*10^{-11} (Pa^{-1}), -2.68*10^{-11} (Pa^{-1}) and 4.64*10^{-12} (Pa^{-1}), respectively.

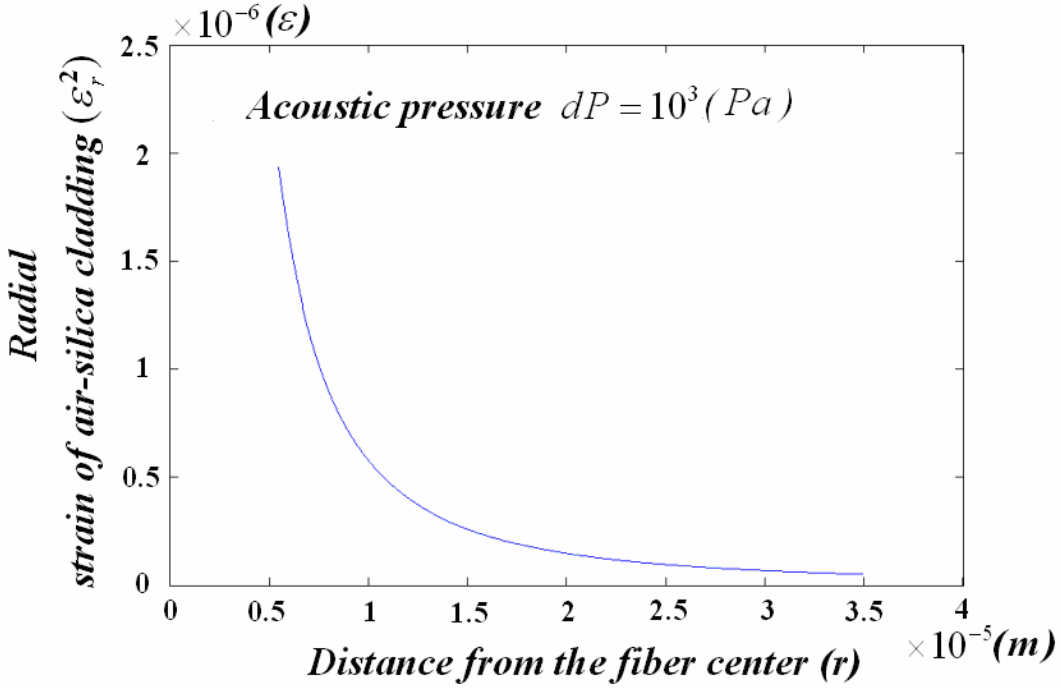

Fig. 3.17 Radial strain ε_r^2 in the hollow-core PBF microstructure cladding, when the fibre is subjected to axial strain of 10^{-3} (ε).

We further calculated the normalized phase responsivity (NR) to acoustic pressure and the relative contribution of S_L and S_n for the hollow-core PBF with the same outer diameter (including jacket), core size and air-filling ratio of 70 - 94% but with

the thickness of the outer silica cladding *(c-b)* increased from 1 to 30 (μm). The results are shown in Fig. 3.18 and Fig. 3.19 respectively. The results show that the NR of HC-PBF to acoustic pressure can be improved by optimizing the thickness of the fibre's silica cladding and the air-filling ratio; however the relative contribution of the refractive index, as compared to physical change of the fibre length, S_n/S_L remains around -15%.

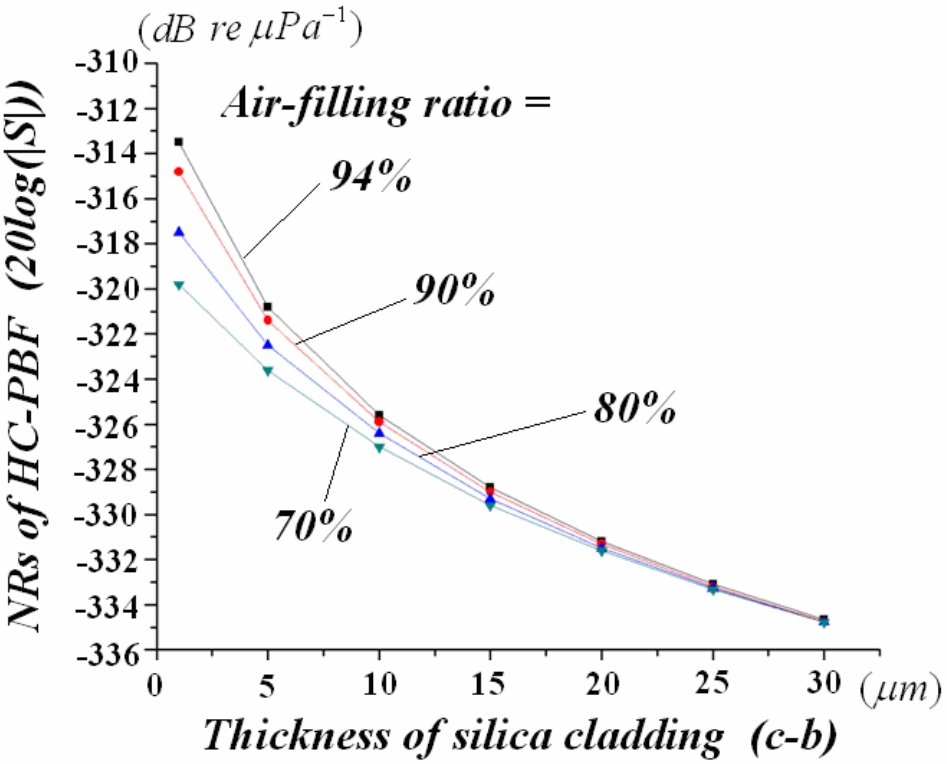

Fig. 3.18 NRs of the hollow-core PBF as function of the thickness of the silica cladding (*c-b*) for different air filling ratios.

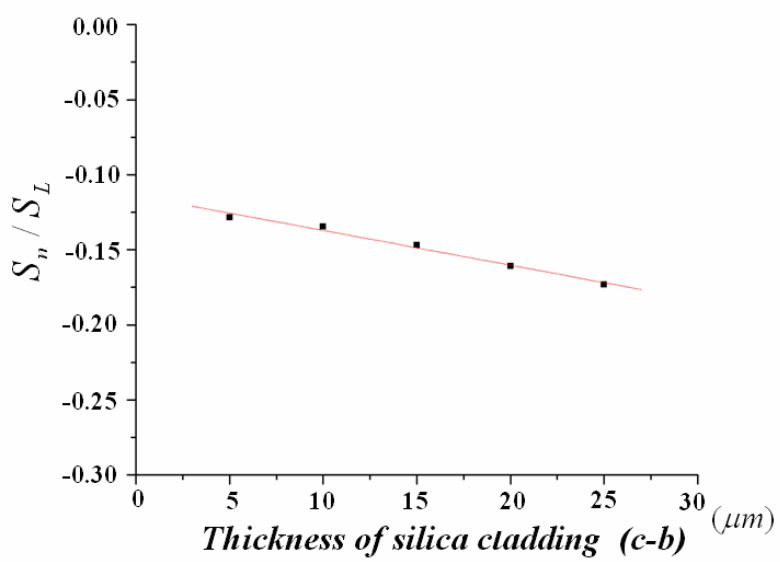

Fig. 3.19 Calculated S_n/S_L of the hollow-core PBF as the function of (c-b), while other parameters are fixed at a=5.45 (μm), b=35 (μm), d=110 (μm), and η=94%.

3.3.3 Temperature

The normalized phase sensitivity of the hollow-core PBF to temperature may be expressed as Eq. (2.24). For the normalized phase sensitivity to temperature, the length term of Eq. (2.24) can be calculated by using the z-direction strain (ε_r^2) discussed in Section 3.2.3. The index term of Eq. (2.24) is mainly caused by three effects as shown in Eq. (3.28): 1) the thermal-optic effect (S_{nto}) of the fibre's silica material. The relationship between the material index change of the silica and the temperature variation is shown in Eq. (3.29), where γ is the thermo-optic coefficient of the silica material; 2) the thermal-strain effect (S_{ntd}), which represents the physical deformation of the fibre's structure induced by the temperature variation; and 3) the strain-optic effect (S_{ntdo}), which represents the thermal-induced strain may modify the index of the silica material by strain-optic effect.

$$S_n = \frac{1}{n_{eff}} \frac{dn_{eff}}{dT} = S_{nto} + S_{ntd} + S_{ntdo} \tag{3.28}$$

$$\Delta n|_{\Delta T} = \gamma \Delta T \tag{3.29}$$

We simulated the phase sensitivity of the HC-1550-02 fibre when it is subjected to temperature variation. Table 3.1 and Fig. 3.3 show the physical parameters and the SEM photograph of the HC-1550-02 fibre respectively. For temperature variation, the length term of the HC-1550-02 fibre can be calculated to be ~2.1155*10^{-6} (1/K).

Importing the model discussed in Section 3.2 and 3.3 into the finite element solver, the variations of the refractive index n_{eff} due to the three effects: S_{nto}, S_{ntd}, and S_{ntdo} as the functions of the temperature variation (ΔT) can be obtained. The results are shown in Fig. 3.20.

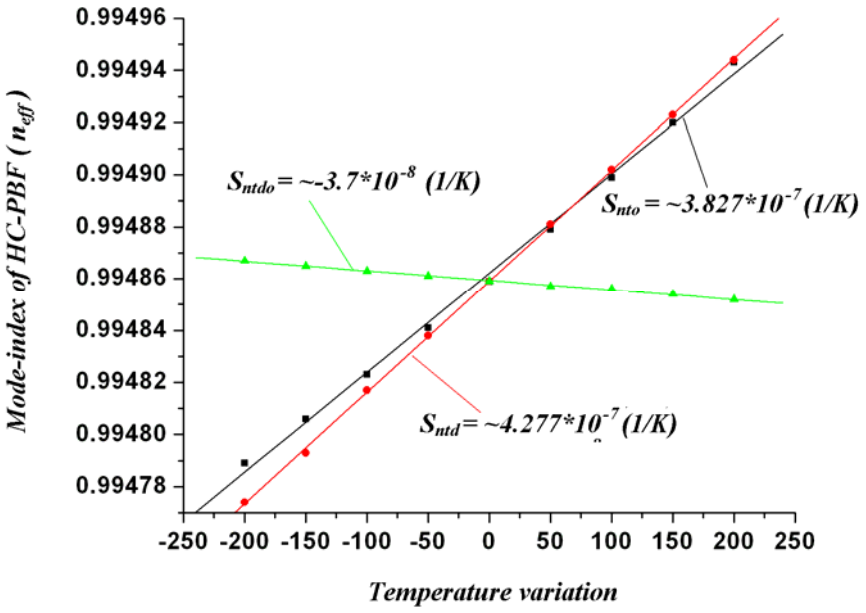

Fig. 3.20 Variations of the refractive index n_{eff} due to the three effects (S_{nto}, S_{ntd}, and S_{ntdo}) as the functions of the temperature variation (ΔT).

From Fig. 3.20, S_{nto}, S_{ntd}, and S_{ntdo} for HC-1550-02 fibre are estimated to be

~3.827*10^{-7} (K^{-1}), ~4.277*10^{-7} (K^{-1}) and ~-3.7*10^{-8} (K^{-1}), respectively. Thus the index term of the HC-1550-02 fibre is the sum of those three effects, and can be calculated to be S_n = 7.734*10^{-7} (K^{-1}). Thus as shown in Eq. (2.24), the phase sensitivity of the HC-1550-02 fibre is the sum of its length term and index term, and can be calculated to be S = ~2.89*10^{-6} (K^{-1}).

3.4 Birefringence of Hollow-core PBFs Due to Lateral Pressure

In Section 3.2 of this chapter, the deformations of the three regions in the hollow-core PBF, when the fibre is subjected to lateral pressure, are calculated. Using the same model discussed in Section 3.3, we can obtain the deformation of in-profile structure of the hollow-core PBF, when the fibre is subjected to lateral pressure. The simulation shows that the lateral pressure can result in deformation of the fibre's hollow core as well as the cells in the fibre's air-silica cladding, both of which may induce linear birefringence to the hollow-core PBF.

According the knowledge of cellular solids [85], most of the deformations of the core and air-silica cladding of the hollow-core PBF, when the fibre is subjected to lateral pressure, come from the bending of the cells in the fibre's air-silica cladding. Thus, when simulating the fibre birefringence induced by lateral pressure, we neglect the index change of the silica material due to lateral pressure.

We simulated the birefringence of the HC-1550-02 fibre when it was subjected to different lateral pressures. Table 3.1 and Fig. 3.3 shows the physical parameters and the SEM photograph of the HC-1550-02 fibre respectively. We applied the model described in Section 3.2 and 3.3 to simulate the HC-1550-02 fibre, when it was

subjected to lateral pressure of $LP = 10^8$ (Pa). The deformed transverse profile of the hollow-core PBF is calculated and plotted in Fig. 3.21. In Fig. 3.21, the red pattern shows the deformed profile, while the black one shows the original profile of the hollow-core PBF.

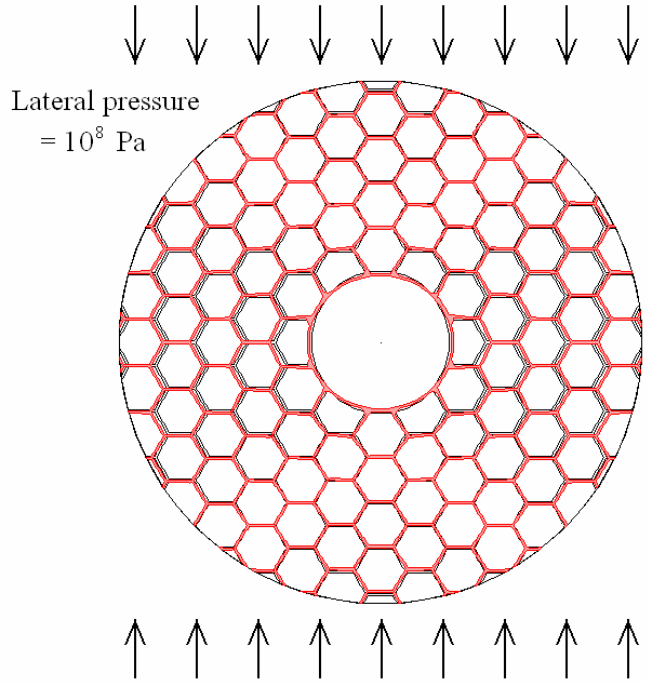

Fig. 3.21 Deformed profile (red) of the hollow-core PBF, when the fibre is under the lateral pressure of $LP = 10^8$ (Pa). For comparison, the original profile is shown in black.

With the elasticity model, the deformations of the HC-1550-02 fibre under different lateral pressures were obtained. The deformed profiles were then imported into the finite element analysis solver to compute the birefringence and the mode field profile of the orthogonal polarization of the fundamental mode. We calculated the pressure-induced birefringence of the HC-1550-02 fibre as the function of the applied lateral pressure at the wavelength of 1550 nm, and the results are shown as the blue (▼) curve in Fig. 3.22. The results for the hollow-core PBFs, which have the same core and air-silica inner cladding but different thickness of the silica outer cladding (*c*-*b*)

with the HC-1550-02 fibre, are also calculated and shown in Fig. 3.22. It can be seen in Fig. 3.22 that the pressure-induced birefringence increases with the applied lateral pressure, and the hollow-core PBF with thinner silica outer cladding has higher birefringence sensitivity to lateral pressure.

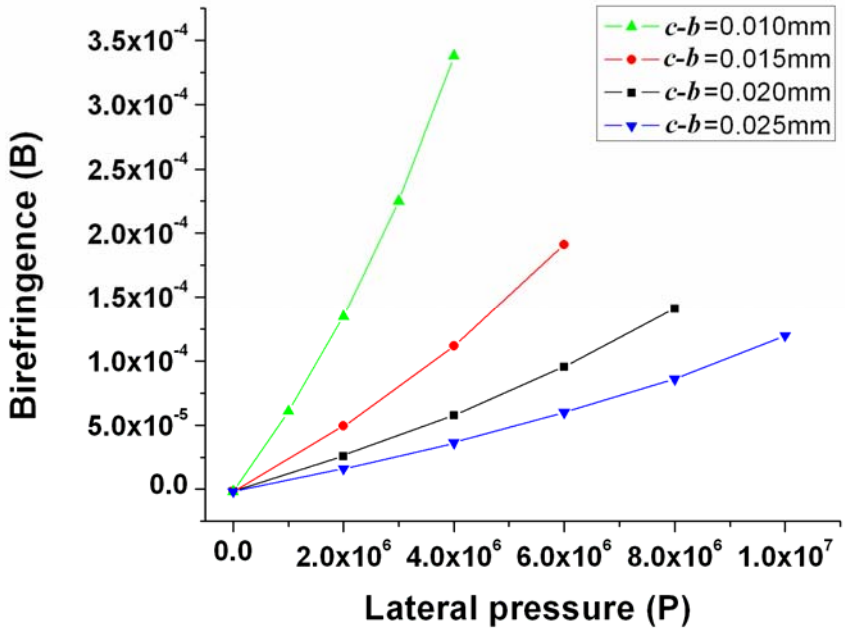

Fig. 3.22 Induced birefringence of the hollow-core PBF as the function of the applied lateral pressure for different thickness of the outer silica cladding (*c*-*b*).

3.5 Summary

We have constructed the theoretical model for the hollow-core PBF. This model can be used to simulate the physical deformations and the effective index changes of the hollow-core PBF, when the fibre is subjected to different measurands. One type of hollow-core PBF (HC-1550-02 fibre) is simulated by using this general model for the hollow-core PBF, and the phase sensitivities of the HC-1550-2 fibre to axial strain, temperature and acoustic pressure, and its birefringence sensitivity to lateral pressure are predicted respectively. The simulations results show that the normalized

phase sensitivity of the HC-1550-02 fibre to axial strain is ~0.9797 (ε^{-1}); its normalized phase sensitivity to temperature is ~-2.89*10^{-6} (K^{-1}); and its normalized phase sensitivity to acoustic pressure is ~-333.1 (dB re μPa^{-1}), which is about 15 dB higher than that of conventional silica fibre.

Chapter 4

Theoretical Modelling for Hybrid PCFs

One type of PCF - hybrid PCF guiding light by both index-guiding and bandgap-guiding simultaneously was demonstrated [39]. The hybrid PCF was composed of air-holes (arranged in a hexagonal pattern) and Ge-doped silica rods (replaced a single row of air holes along one of the hybrid PCF axes). The SEM photograph of the hybrid PCF is shown in Fig. 4.1. Because the guiding mechanisms of the hybrid PCF are different in two orthogonal directions, high birefringence is expected [40]. However, to our knowledge, the birefringence responses of the hybrid PCF to axial strain and temperature were not investigated.

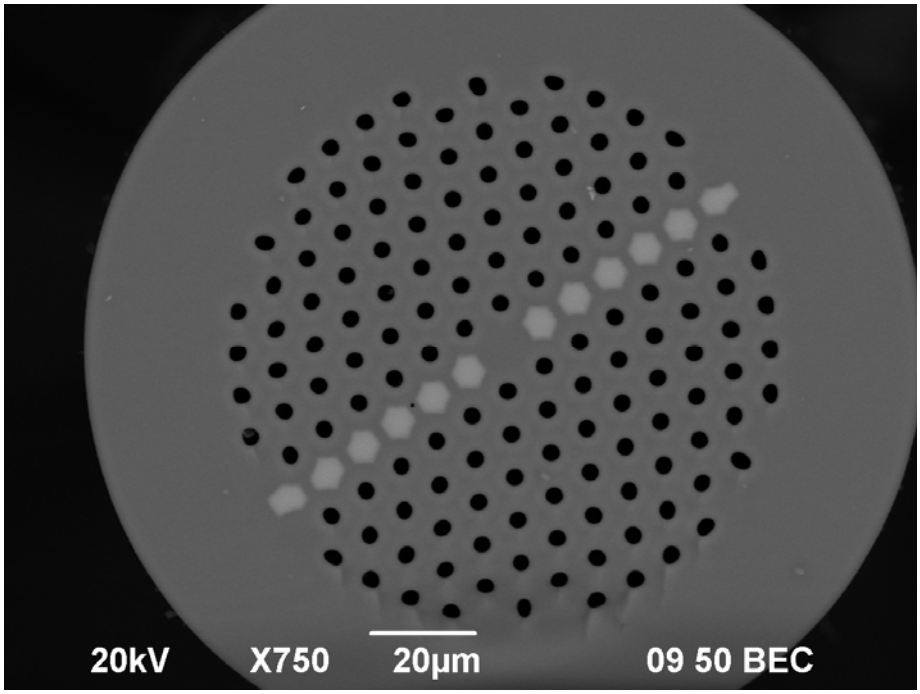

Fig. 4.1 SEM photograph of the hybrid PCF.

4.1 Elastic Model of hybrid PCFs

The structure of the hybrid PCF, as shown in Fig. 4.2, is a modified PCF structure which is obtained by replacing one longitudinal set of air holes of an air-silica index-guiding PCF by high index Ge-doped silica rods. The PCF has 7 rings of holes with a pitch of Λ; the diameters of the fibre's silica cladding, air holes and Ge-doped rods are D, d_0 and d_1 respectively. Thus we can make an assumption that the light can be confined in the core by index-guiding in one direction and bandgap-guiding in the other transverse direction, even if the bandgap structure is not a full two dimensional photonic crystal structure [39 and 40].

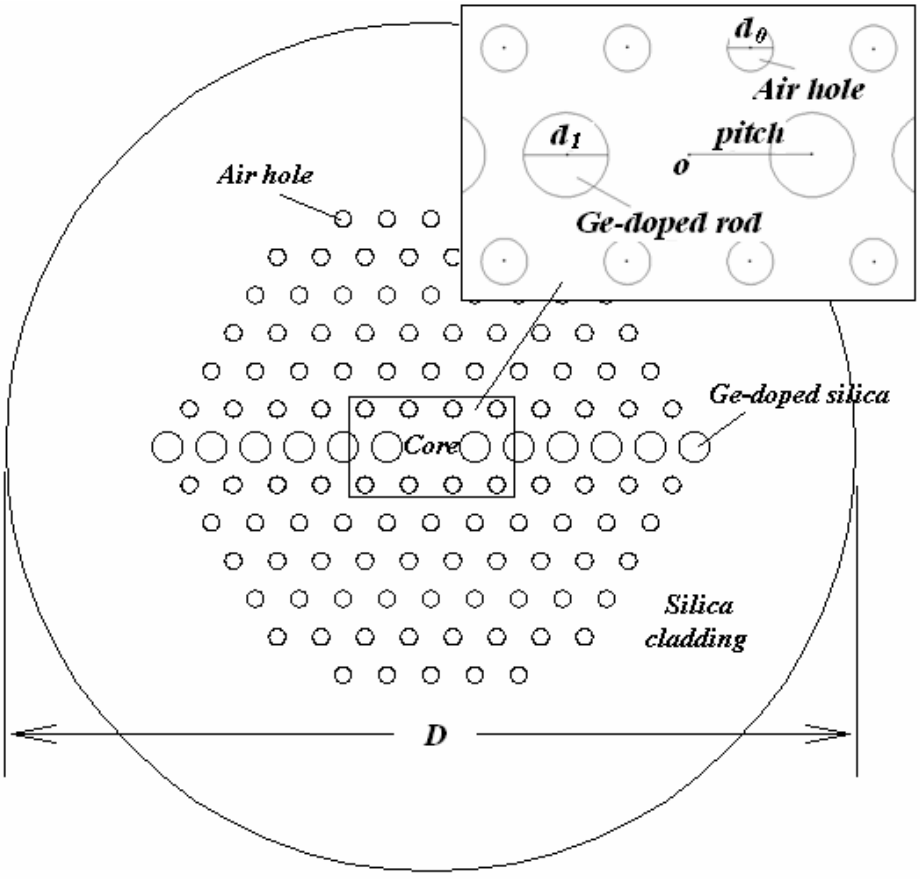

Fig. 4.2 Schematics of cross-section of the hybrid PCF.

4.2 Birefringence of hybrid PCFs

4.2.1 Model for A Single Rod

The model for a single doped rod in a hybrid PCF is shown in Fig. 4.3. Region 0 is the pure silica background with the refractive index of n_0; Region 1 is a Ge-doped rod with the molar concentration of η. The relationship between the rod's molar concentration (η) and its refractive index (n_1) can be written as Eq. (4.1) [95].

$$n_1 = n_0 + 6.63\times10^{-4}\times\frac{104.6\eta}{104.6\eta + 60(1-\eta)} \tag{4.1}$$

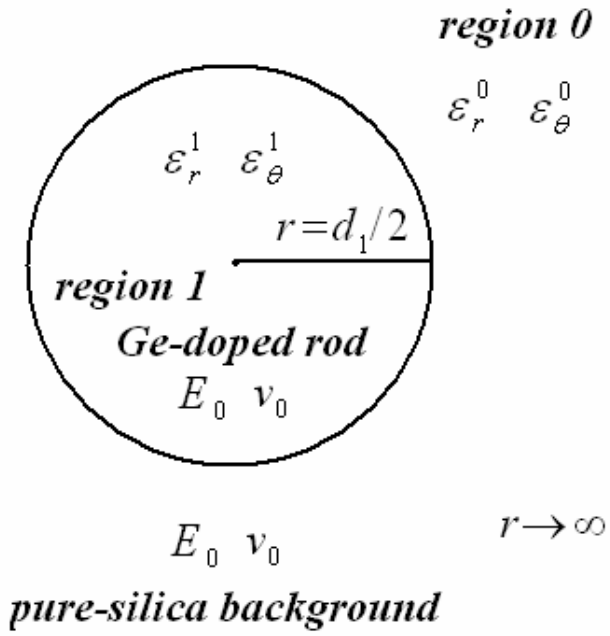

Fig. 4.3 Model for a single doped rod in a hybrid PCF.

The thermal expansion coefficient of pure silica background is α_0. The thermal expansion coefficient of the doped rod (α_1) is the function of its doped molar concentration, and can be expressed as Eq. (4.2), where α_g is the thermal coefficient of GeO_2 material [96].

$$\alpha_1 = \alpha_0(1-\eta) + \alpha_g\eta \tag{4.2}$$

Because of the difference between α_1 and α_0, built-in strains are introduced when the hybrid PCF is drawn and cooled in the manufacturing process [96]. The elastic properties for silica glass do not depend strongly on its doped composition, so the Young's modulus and Poisson's ratios of both regions 0 and 1 can be approximately expressed as E_0 and v_0. Because the pure silica background has much larger area than the doped rod, the doped rod in the axial direction will be strained to match the length of pure silica background [96]. Hence, for the plane approximation the strain in axial (z) directions of the doped rods and silica background can be written as Eq. (4.3), where T_f is the final room temperature and T_i is the high initial temperature in the fibre manufacture process. For GeO_2 doped silica, $T_f - T_i$ is approximately regarded as -1000 ºC [96].

$$\begin{aligned} \varepsilon_z^0 &= 0 \\ \varepsilon_z^1 &= (\alpha_0 - \alpha_1)(T_f - T_i) \end{aligned} \tag{4.3}$$

Assuming the pure silica background has infinite area for simplicity, using the theory of elasticity the in-profile stress expressions of region 0 and 1 may be expressed as Eq. (4.4) [85], where A and C are constants. Using Hooke's law, we obtain the strain tensors of regions 0 and 1 shown as Eq. (4.5).

$$\begin{cases} \sigma_r^0 = \dfrac{A}{r^2} \\ \sigma_\theta^0 = -\dfrac{A}{r^2} \end{cases} \qquad \begin{cases} \sigma_r^1 = 2C \\ \sigma_\theta^1 = -2C \end{cases} \tag{4.4}$$

$$\begin{cases} \varepsilon_r^0 = \dfrac{1}{E_0}(1+v_0)\dfrac{A}{r^2} + \alpha_0(T_f - T_i) \\ \varepsilon_\theta^0 = -\dfrac{1}{E_0}(1+v_0)\dfrac{A}{r^2} + \alpha_0(T_f - T_i) \end{cases} \qquad \begin{cases} \varepsilon_r^1 = \dfrac{2}{E_0}(1-v_0)C + \alpha_1(T_f - T_i) \\ \varepsilon_\theta^1 = \dfrac{2}{E_0}(1-v_0)C + \alpha_1(T_f - T_i) \end{cases} \tag{4.5}$$

To determine the constants, the boundary condition of this model can be written as Eq. (4.6), where μ_r^i is the radial displacement in the region *i*, which is related to radial strain by Eq. (4.7). Eqs. (4.6a) and (4.6b) describe radial stress and displacement continuities across the boundary of regions, respectively.

$$\begin{cases} \sigma_r^0 \mid_{r=d_1/2} = \sigma_r^1 \mid_{r=d_1/2} & (a) \\ \mu_r^0 \mid_{r=d_1/2} = \mu_r^1 \mid_{r=d_1/2} & (b) \end{cases} \tag{4.6}$$

$$\mu_r^i = \int \varepsilon_r^i dr \tag{4.7}$$

Substituting Eqs. (4.4), (4.5) and (4.7) into the boundary conditions, the constants *A* and *C* can be determined. Hence the stress, strain and displacement distributions of the doped rod can be obtained. According to the theory of elasticity [88], the stress distributions of doped rods in the rectangular and polar coordinates can be written as Eq. (4.8).

$$\sigma_x^1 = \sigma_y^1 = \sigma_r^1 = \sigma_\theta^1 = \frac{1}{2} E_0(\alpha_0 - \alpha_1)(T_f - T_i) \tag{4.8}$$

The index distributions of the doped rods will be modified through strain-optic effect and this effect appears as a change in the optical indicatrix of the silica material [91]. Silica material is a homogeneous isotropic medium and only two elements of the strain-optic tensor, p_{11} and p_{12}, have their values, thus the changes in the optical indices can be written as Eq. (4.9).

$$\begin{aligned} \Delta n_x^1 &= -\frac{1}{2} n_1^3 (p_{11}\varepsilon_x^1 + p_{12}\varepsilon_y^1 + p_{12}\varepsilon_z^1) \\ \Delta n_y^1 &= -\frac{1}{2} n_1^3 (p_{12}\varepsilon_x^1 + p_{11}\varepsilon_y^1 + p_{12}\varepsilon_z^1) \\ \Delta n_z^1 &= -\frac{1}{2} n_1^3 (p_{12}\varepsilon_x^1 + p_{12}\varepsilon_y^1 + p_{11}\varepsilon_z^1) \end{aligned} \tag{4.9}$$

4.2.2 Build-in Stress in Hybrid PCF Core

Because the distribution of the doped rods in the profile of the hybrid PCF is asymmetric as shown in Fig. 4.1, the stresses of the doped rods, introduced in the manufacturing process of the fibre, induce asymmetric built-in strain distribution in the fibre core, which induces high birefringence of the hybrid PCF. So when calculating the birefringence property of the hybrid PCF, it is necessary to take these asymmetric strain distributions of the fibre core into consideration as follows:

A. *x*-direction built-in stress distribution of the fibre core area

As Fig. 4.4 shows, assuming the fibre core has the diameter of $d_{core}=2*\Lambda-d_1$, for simplicity we assume that the *x*-direction stress of the core (σ_x^{core}) is uniform along the *x*-direction and can be written as Eq. (4.10), where *I* is constant. Using the theory of elasticity [85], we sum up forces of element *FF'G'H'MHG* in the *x*-direction as shown in Fig. 4.4, and obtain the equation of equilibrium shown as Eq. (11).

$$\sigma_x^{core} = I\cos(\frac{\pi y}{d_{core}}) \tag{4.10}$$

$$\sigma_x^1 d_1 = \int_{-d_{core}/2}^{d_{core}/2} \sigma_x^{core} dy \tag{4.11}$$

Substituting Eq. (4.10) into Eq. (4.11), we obtain the constant $I = \pi d_1 \sigma_x^1/(2d_{core})$.

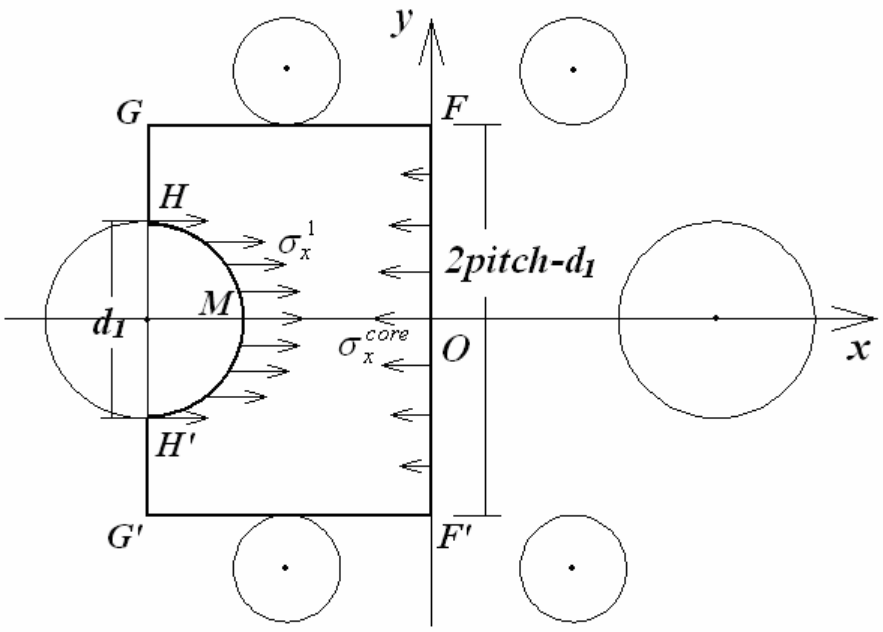

Fig. 4.4 *x*-direction built-in stress distributions of the hybrid PCF core area.

B. *y*-direction built-in stress distribution of the fibre core area

As shown in Fig.4.5, we assume that the *y*-direction stress distribution of fibre's core area (σ_y^{core}) is uniform along the *x*-direction and is only the function of *y*. In Fig. 4.5, a line (*JJ'*) parallel with *x* coordinate is used to cut element *JKJ'* out from the hybrid PCF's profile. The equilibrium equation of element *JKJ'* in *y* direction may be derived as Eq. (4.12), where the term *12* is due to the fact that there are twelve doped rods in the profile of hybrid PCF. Thus the stress distribution of fibre core in the *y*-direction can be written as Eq. (4.13).

$$\sigma_y^1 \times 12 \times 2\sqrt{(\frac{d_1}{2})^2 - y^2} + \sigma_y^{core} \times (D - 12 \times 2\sqrt{(\frac{d_1}{2})^2 - y^2}) = 0 \qquad (4.12)$$

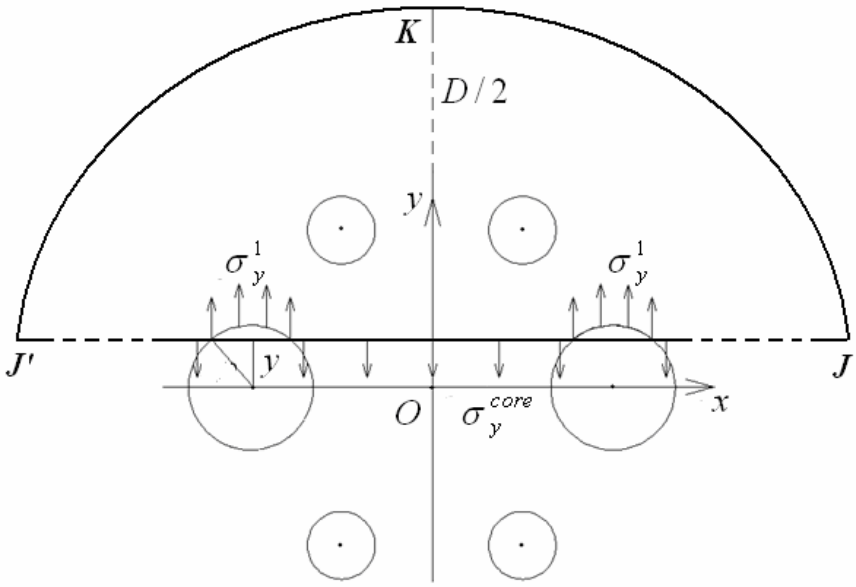

Fig. 4.5 *y*-direction built-in stress distributions of the hybrid PCF core area.

$$\begin{cases} \sigma_y^{core} = -\dfrac{24\sigma_y^1\sqrt{(\frac{d_1}{2})^2 - y^2}}{D - 24\sqrt{(\frac{d_1}{2})^2 - y^2}} & |y| \le \dfrac{d_1}{2} \\ \sigma_y^{core} = 0 & |y| > \dfrac{d_1}{2} \end{cases} \tag{4.13}$$

Using Hooke's law, the asymmetric strain distributions induced by built-in stress can be written as Eq. (4.14).

$$\begin{cases} \varepsilon_x^{core} = \dfrac{1}{E_0}(\sigma_x^{core} - v_0\sigma_y^{core}) \\ \varepsilon_y^{core} = \dfrac{1}{E_0}(\sigma_y^{core} - v_0\sigma_x^{core}) \\ \varepsilon_z^{core} = 0 \end{cases} \tag{4.14}$$

Now using the strain-optic effect of the silica material, the asymmetric index modulation in the core of the hybrid PCF due to the built-in stress can be obtained as Eq. (4.15).

$$\begin{aligned}\Delta n_x^{core} &= -\frac{1}{2}n_1^3(p_{11}\varepsilon_x^{core} + p_{12}\varepsilon_y^{core}) \\ \Delta n_y^{core} &= -\frac{1}{2}n_1^3(p_{12}\varepsilon_x^{core} + p_{11}\varepsilon_y^{core}) \\ \Delta n_z^{core} &= -\frac{1}{2}n_1^3(p_{12}\varepsilon_x^{core} + p_{12}\varepsilon_y^{core})\end{aligned} \tag{4.15}$$

4.2.3 Simulation Results

We applied the theoretical mode for the hybrid PCF to calculate the birefringence property of the hybrid PCF. Table 4.1 shows the physical parameters of the HYBRID2007_2PBG_OD151 fibre manufactured by University of Bath [39]. The SEM photograph of this fibre is shown in Fig. 4.1.

Table 4.1 Physical parameters of HYBRID2007_2PBG_OD151

	D	Λ	d_0	d_1	v_0	E_0
Fibre	*160 (μm)*	*8 (μm)*	*3(μm)*	*5.58(μm)*	*0.17*	*72(GPa)*
HYBRID 2007_2P BG	α_0	α_g	η	n_0	p_{11}	p_{12}
	$5.5*10^{-7}$ (K^{-1})	$7*10^{-6}$ (K^{-1})	*0.35*	*1.444*	*0.121*	*0.27*

Using parameters shown in Table 4.1, we can obtain the in-profile structure of the hybrid PCF. And by using Eq. (4.9) and Eq. (4.15), the index distributions of the fibre's doped rods, silica background and core are also obtained respectively. All of them are then imported into the finite element analysis solver to compute the fundamental mode profiles and birefringence of the hybrid PCF. Fig. 4.6 shows the calculated intensity profiles of HYBRID2007_2PBG fibre and its effective indices (N_{eff}) of the fundamental modes in the two orthogonal polarization directions. The

simulation results show that the hybrid PCF has the birefringence of B = ~2.374*10^{-4} at the wavelength of 1550 nm.

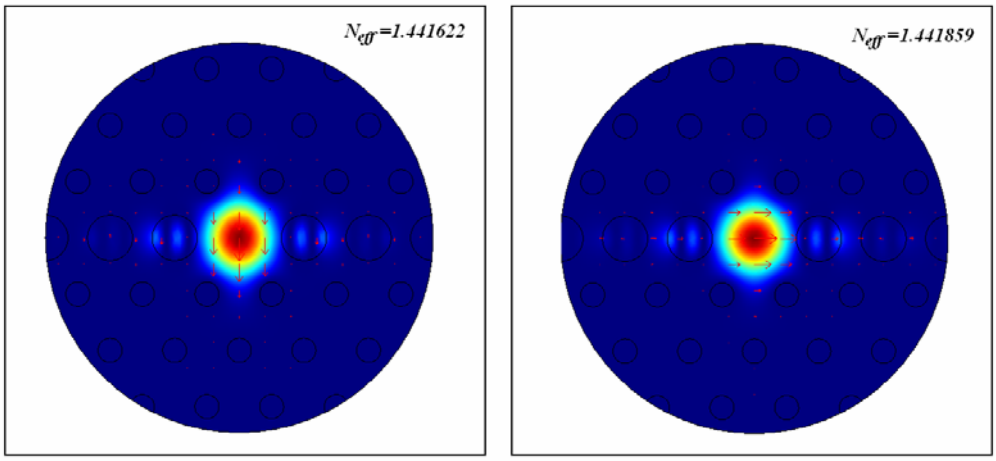

Fig. 4.6 Calculated intensity profile and effective refractive indices of the fundamental mode of the hybrid PCF in two orthogonal polarization directions.

We further calculated the birefringence of the hybrid PCF as the function of the molar concentration and diameter of the doped rods at the wavelength of 1550 nm, when other parameters are fixed as Table 4.1. The simulation results are shown in Fig. 4.7 and Fig. 4.8 respectively. As Fig. 4.7 shows, when the diameter of the doped rods is fixed at 5.58 (μm), the birefringence of the hybrid PCF increases as the molar concentration of doped rods increases from 0.23 to 0.4. This is because that the higher molar concentration will cause larger difference of the thermal expansion coefficient between pure silica background and doped rods, and thus larger built-in stress of the fibre core. As shown in Fig. 4.8, the birefringence of the hybrid PCF can also be improved by increasing the diameter of the doped rods in the range of 4.4 to 5.8 (μm), when its molar concentration is fixed at 0.35. This is because the larger doped rods can enhance the built-in stress of the fibre core.

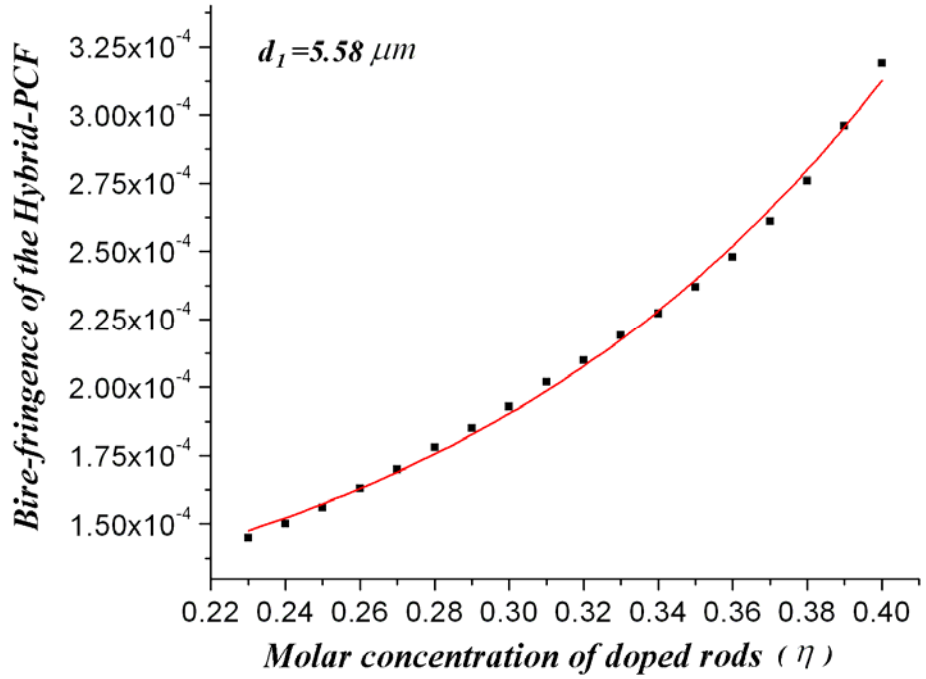

Fig. 4.7 Birefringence of the hybrid PCF as the function of the molar concentration of the doped rods.

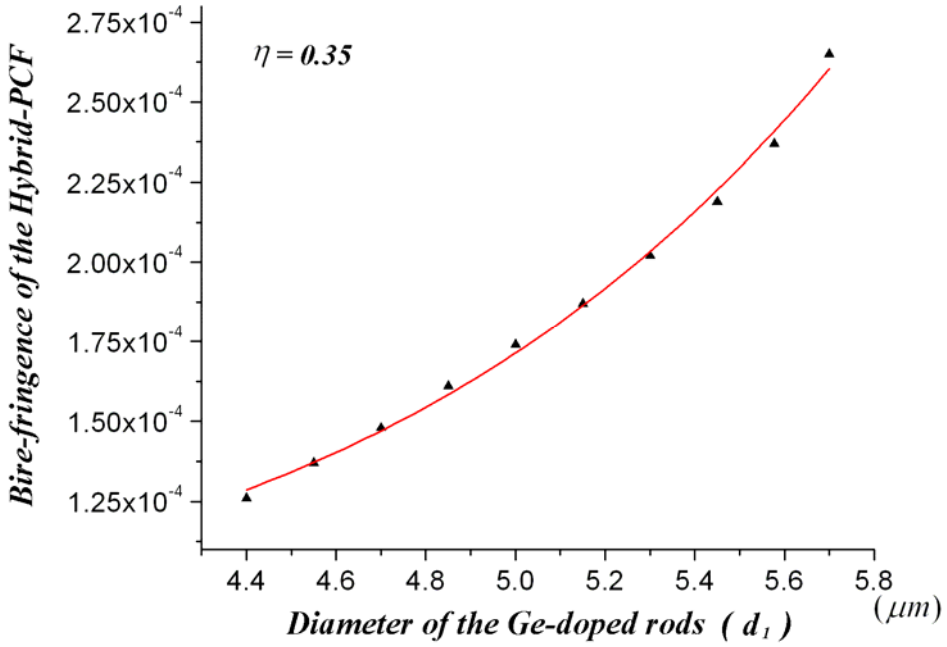

Fig. 4.8 Birefringence of the hybrid PCF as the function of the diameter of the doped rods at the wavelength of 1550 nm.

4.3 Birefringence responses of Hybrid PCFs to Different Measurands

4.3.1 Axial Strain

When the hybrid PCF is subjected to axial stress of ε, the induced changing of birefringence is due to two factors: 1) the axial stress will cause the deformation of the fibre's profile by changing the dimensions of the hybrid fibre; 2) the axial stress will modulate the silica material index by strain-optic effect. For the first factor, because the hybrid PCF is composed of two silica materials which have the same elasticity property of E_0 and v_0, for simplicity, the change of fibre dimensions can be written as Eq. (4.16), where $\Delta\Lambda|_\varepsilon$, $\Delta D|_\varepsilon$, $\Delta d_0|_\varepsilon$ and $\Delta d_1|_\varepsilon$ are the change of the fibre's pitch, diameter changes of the fibre's silica cladding, air holes and doped rods respectively, when the fibre is subjected to axial strain.

$$\begin{cases} \Delta D\,|_\varepsilon = -v_0 \varepsilon D \\ \Delta\Lambda\,|_\varepsilon = -v_0 \varepsilon \Lambda \\ \Delta d_0\,|_\varepsilon = -v_0 \varepsilon d_0 \\ \Delta d_1\,|_\varepsilon = -v_0 \varepsilon d_1 \end{cases} \tag{4.16}$$

For the index modulation due to axial strain, the pure silica background and doped rods of the hybrid PCF have the same index variations shown as Eq. (4.17).

$$\begin{aligned} \Delta n_x^0\,|_\varepsilon &= \Delta n_x^1\,|_\varepsilon = -\frac{1}{2} n_0^3 [\varepsilon(1-v_0) p_{12} - \varepsilon v_0 p_{11}] \\ \Delta n_y^0\,|_\varepsilon &= \Delta n_y^1\,|_\varepsilon = -\frac{1}{2} n_0^3 [\varepsilon(1-v_0) p_{12} - \varepsilon v_0 p_{11}] \\ \Delta n_z^0\,|_\varepsilon &= \Delta n_z^1\,|_\varepsilon = -\frac{1}{2} n_0^3 [\varepsilon p_{11} - 2\varepsilon v_0 p_{12}] \end{aligned} \tag{4.17}$$

In Eq. (4.17), $\Delta n_x^0|_\varepsilon$, $\Delta n_y^0|_\varepsilon$, $\Delta n_z^0|_\varepsilon$, $\Delta n_x^1|_\varepsilon$, $\Delta n_y^1|_\varepsilon$ and $\Delta n_z^1|_\varepsilon$ are index variations of the

fibre's silica background and doped rods due to axial strain in three directions respectively.

The birefringence response of the hybrid PCF to axial strain is simulated by using this theoretical model. Table 4.1 shows the physical parameters of the HYBRID2007_2PBG_OD151 fibre manufactured by University of Bath [39]. The SEM photograph of this fibre is shown in Fig. 4.1. When the hybrid PCF is subjected to axial strain, two factors of the fibre are changed: 1) the physical dimensions of the fibre shown as Eq. (4.16); 2) the material indices of silica by strain-optic effect shown as Eq. (4.17). Importing both of them into the finite element solver, the variations of the birefringence of the HYBRID2007_2PBG fibre as the function of axial strain can be obtained. The results are shown in Fig. 4.9 and the slopes of the curve ($\Delta B/\varepsilon$) is calculated to be ~$5.663*10^{-4}$ (ε^{-1}).

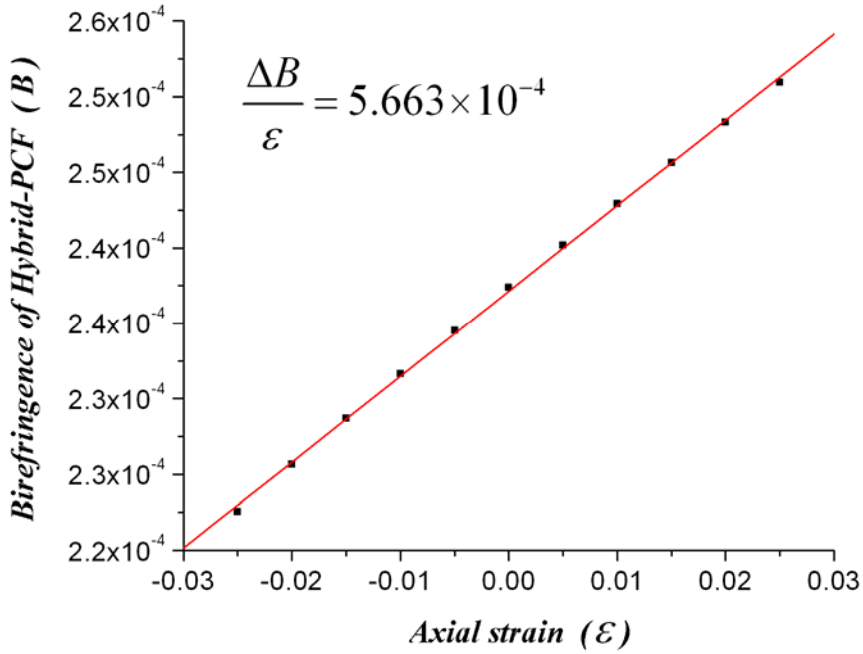

Fig. 4.9 Birefringence of the HYBRID2007_2PBG fibre as the function of the axial strain.

Further we calculated the responses of the hybrid PCF's birefringence to axial strain ($\Delta B/\varepsilon$), as the function of the molar concentration and the diameter of Ge-doped rods. The results are shown in Fig. 4.10 and 4.11 respectively. It is shown that the curves of $\Delta B/\varepsilon$ as the molar concentration and the diameter of the doped rods have a similar pattern. When the molar concentration of the doped rods is more than 0.28 and its diameter is more than 4.9μm, $\Delta B/\varepsilon$ of the hybrid PCF increases with the increasing of η and d_1. This is because that both higher molar concentration and larger diameter of the doped rods can induce more asymmetry for the hybrid fibre's profile. The $\Delta B/\varepsilon$ of hybrid PCF reaches its minimum at the molar concentration of ~0.28 and the diameter of ~4.9μm, and as the η and d_1 decrease further, the $\Delta B/\varepsilon$ increases. This is because that when η and d_1 decrease to some extent, the effective mode area of the hybrid PCF's fundamental modes will increase and thus more light of the fundamental mode will travel in the doped rods. This will induce the increasing of the fibre's $\Delta B/\varepsilon$.

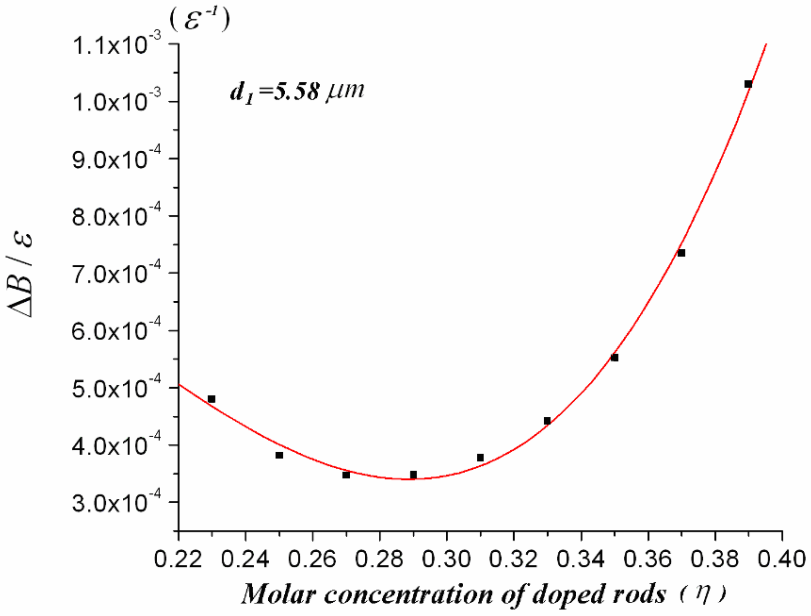

Fig. 4.10 Responses of the hybrid PCF's birefringence to axial strain ($\Delta B/\varepsilon$) as the function of the molar concentration of the doped rods

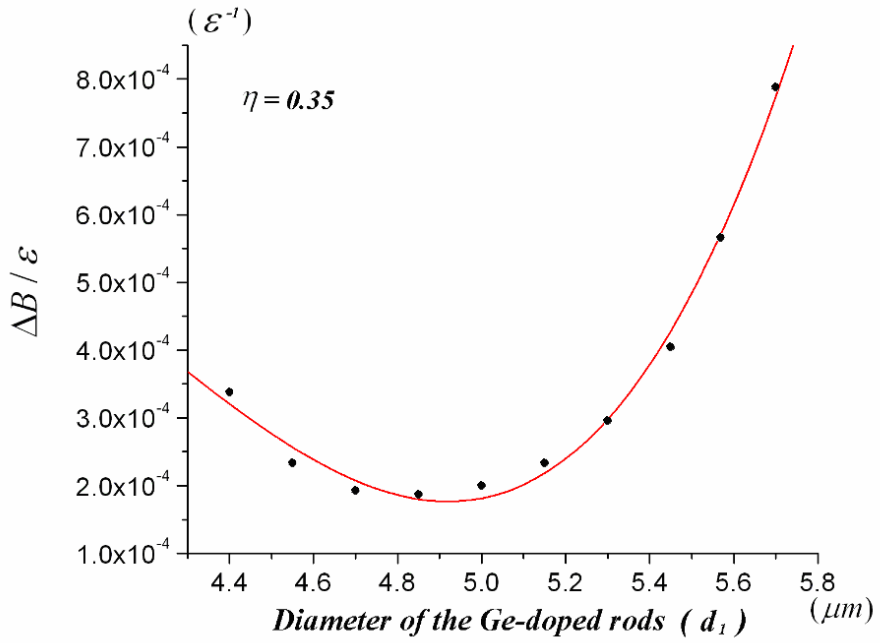

Fig. 4.11 Responses of the hybrid PCF's birefringence to axial strain ($\Delta B/\varepsilon$) as the function of the diameter of the doped rods.

4.3.2 Temperature

When the hybrid PCF is subjected to temperature variations of ΔT, the induced changes of the fibre's birefringence are the sum of three effects. The first one is the thermal expansion of the fibre, which modifies the fibre's dimensions. The second effect is the changes in material index induced by thermo-optic effect. The third effect is the changes of the built-in stresses in the fibre core due to temperature variations.

For the first effect, it can be approximately assumed that the doped rods will be strained to match the deformation of the silica background, because the doped rod area in the fibre's profile is much smaller than the area of the pure silica background. Hence the dimension changes of the fibre due to temperature variations can be

approximately written as Eq. (4.18), where $\Delta\Lambda|_{\Delta T}$, $\Delta D|_{\Delta T}$, $\Delta d_0|_{\Delta T}$ and $\Delta d_1|_{\Delta T}$ are the change of the fibre's pitch, diameter changes of the fibre's silica cladding, air holes and doped rods respectively, when the hybrid PCF is subjected to temperature variations.

$$\begin{cases} \Delta D|_{\Delta T} = \alpha_0 \Delta T D \\ \Delta \Lambda|_{\Delta T} = \alpha_0 \Delta T \Lambda \\ \Delta d_0|_{\Delta T} = \alpha_0 \Delta T d_0 \\ \Delta d_1|_{\Delta T} = \alpha_0 \Delta T d_1 \end{cases} \tag{4.18}$$

For the second effect, the thermo-optic coefficient of silica is $\gamma=7.8*10^{-6}$ (K^{-1}), hence the index changes of silica background and doped rods ($\Delta n^0|_{\Delta T}$, $\Delta n^1|_{\Delta T}$) due to thermo-optic effect can be written as Eq. (4.19).

$$\Delta n^0|_{\Delta T} = \Delta n^1|_{\Delta T} = \gamma \Delta T \tag{4.19}$$

For the third effect, the asymmetric index modulation of fibre's core due to the built-in stress can be calculated by using the same method described in Section 4.2.2 and 4.2.3, with different final temperatures (T_f). The new index distributions of fibre core can be calculated by replacing the T_f with ($T_f+\Delta T$).

The birefringence responses of the hybrid PCF to temperature variations are simulated by using this theoretical model. Table 4.1 shows the physical parameters of the HYBRID2007_2PBG_OD151 fibre manufactured by University of Bath. The SEM photograph of this fibre is shown in Fig. 4.1. A change of temperature (ΔT) to the hybrid PCF can modify the fibre's dimensions and material indices by thermal expansion effect and thermal-optic effect respectively. And temperature variations can further modify the built-in stress in the fibre core. All of them will induce the birefringence variations of the hybrid PCF. In Fig. 4.12, we plotted the predicted

birefringence of the HYBRID2007_2PBG fibre as the function of temperature change. The results show that the slope of the curve ($\Delta B/\Delta T$) is ~-1.844*10^{-7} (K^{-1}).

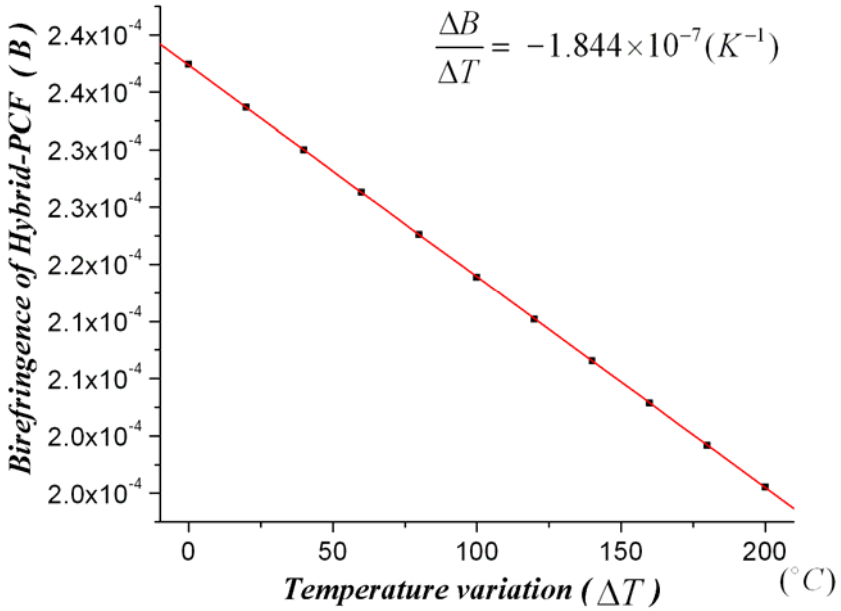

Fig. 4.12 Birefringence of the HYBRID2007_2PBG fibre as the function of the temperature variation.

We further calculated the response of the hybrid PCF's birefringence to temperature variations, when the molar concentration of its doped rods varied from 0.23 to 0.35 shown in Fig. 4.13 and the diameter of the doped rods varied from 4.55 to 5.5 shown in Fig. 4.14. The results show that the responses of hybrid PCF's birefringence to temperature variations ($|\Delta B/\Delta T|$) increase as the molar concentration or diameter of the doped rods increases. This is because that higher molar concentration and larger diameter of the rods will induce higher built-in stress of the fibre core, which will induce higher birefringence responses of the hybrid PCF to temperature variations.

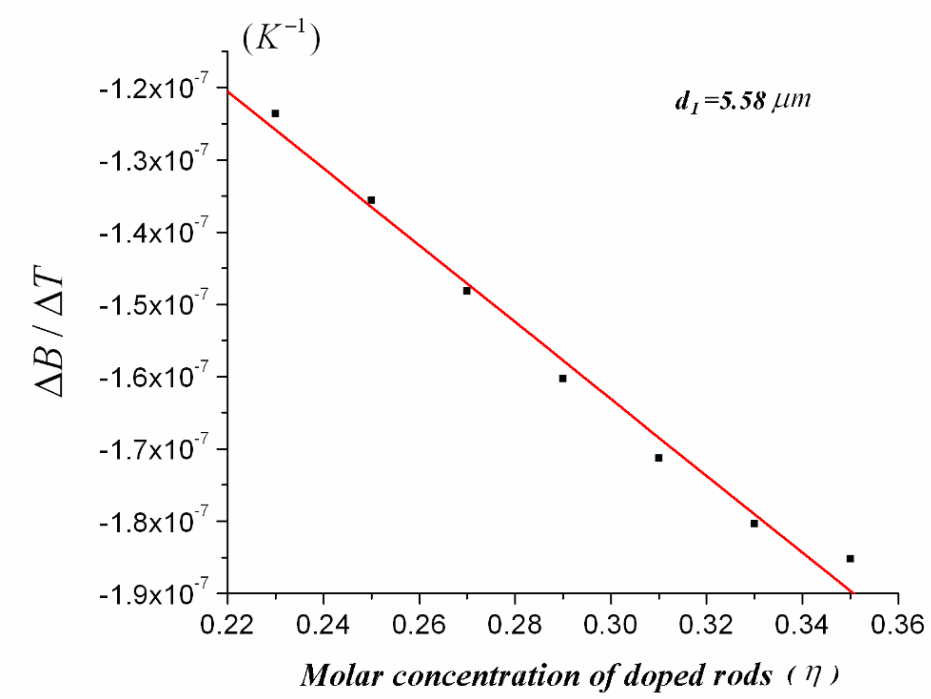

Fig. 4.13 Responses of the hybrid PCF's birefringence to temperature variations ($\Delta B/\Delta T$) as the function of the molar concentration of the doped rods.

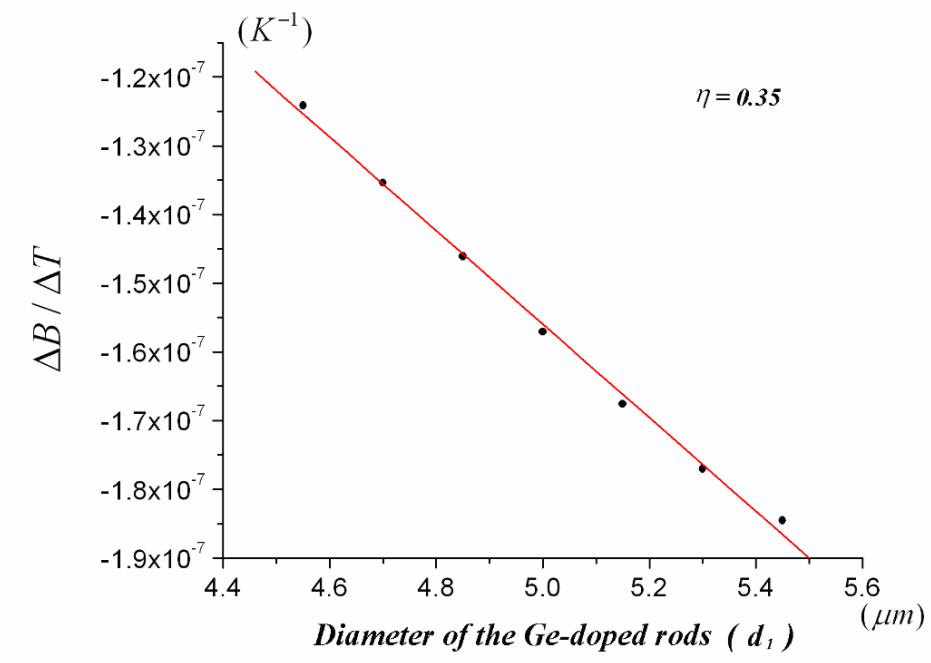

Fig. 4.14 Responses of the hybrid PCF's birefringence to temperature variations ($\Delta B/\Delta T$) as the function of the diameter of the doped rods.

4.4 Summary

We have constructed the theoretical model for the hybrid PCF. This model can be used to simulate the birefringence property of the hybrid PCF, as well as the birefringence responses of the hybrid PCF to axial strain and temperature. The simulation results show that the predicted birefringence of the HYBIRD2007_2PBF_OD151 fibre is ~$2.374*10^{-4}$ at the wavelength of 1550nm, and its birefringence sensitivities to axial strain and temperature are $5.663*10^{-4}$ (ε^{-1}) and ~$-1.844*10^{-7}$ (K^{-1}) respectively. Those values can be modified by varying the design parameters of the hybrid fibre.

Chapter 5

Measurements of PCFs to Different Measurands

1.1 Phase Sensitivities of PCFs to Axial Strain

The phase sensitivities of both the solid-core PCF and the hollow-core PBF to axial strain were experimentally measured. The experimental setup is shown in Fig. 5.1. A fibre-optic Michelson interferometer comprising of a 3-dB single mode fibre coupler, a sensing and a reference arm, was employed. Faraday rotation mirrors (FRMs) were used at the distal ends of both arms to avoid polarization induced signal fading. The interferometer was illuminated by an external cavity laser with a center wavelength of 1550 (nm) and a line width of ~100 (kHz). The HC-1550-02/NL-3.3 fibre was incorporated into the sensing arm of the interferometer, with one end spliced to one port of the 3-dB coupler and the other end to the pigtail of the FRM; the reference arm of the interferometer consisted of a similar length of SMF28 fibre was spliced to the second FRM.

For the axial strain sensitivities measurement, a standard strain test-rail was used to provide the axial strain to the sensing fibre. The sensing PCFs were fixed on the test-rail. The length of the sensing fibre is L. To measure phase sensitivity (S) to axial strain, one end of the rail was fixed, while the other end was computer controlled to move within a known distance (ΔL). The output power variation of the interferometer and the moving distance of the test-rail were simultaneously recorded by the computer. The axial strain acting on the sensing fibre can be calculated by

using $\varepsilon=\Delta L/L$.

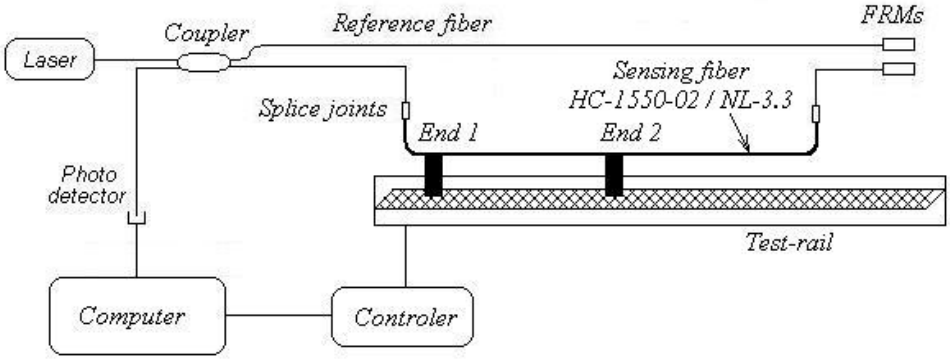

Fig. 5.1 Experimental setup for the axial strain measurements.

Table 5.1 Measured S and predicted S, S_L, S_n of the HC-1550-02/NL-3.3 fibre to axial strain.

fibre	Parameters	
HC-1550-02	Predicted S_L	1 (ε^{-1})
	Predicted S_n	-0.0203 (ε^{-1})
	Predicted S	0.9797 (ε^{-1})
	Measured S	0.9815±0.004 (ε^{-1})
NL-3.3	Predicted S_L	1 (ε^{-1})
	Predicted S_n	-0.2227 (ε^{-1})
	Predicted S	0.7773 (ε^{-1})
	Measured S	0.7813±0.006 (ε^{-1})

The phase sensitivity of the sensing PCF to axial strain was then calculated from the measured number of fringes (N_f) for a given ΔL as shown in Eq. (5.1). The term ($1/2$) in Eq. (5.1) is due to the measurement which was taken with a Michelson interferometer, in which the light went through the sensing fibre twice. The experimental results agree well to the predicted values as summarized in Table 5.1. For sensitivity measurements of HC-1550-02 and NL-3.3 fibres, 258 and 129 fringes were respectively recorded with experimental inaccuracy of smaller than ±1 fringes,

corresponding to inaccuracy in *S* of ~ ±0.004 for HC-1550-02 fibre and ~ ±0.006 for NL-3.3 fibre.

$$S = \frac{1}{\varphi}\frac{\Delta\varphi}{\varepsilon} = (\frac{1}{2})\frac{\lambda N_f}{n_{eff}\Delta L} \tag{5.1}$$

1.2 NR of Hollow-core PBF to Acoustic Pressure

In general, the phase sensitivity of fibre to acoustic pressure is written in term of normalized responsivity (NR) to acoustic pressure. The relationship between NR and S can be expressed as Eq. (5.2).

$$NR = 20Log(|S|) \tag{5.2}$$

The acoustic NRs of the conventional silica fibre (HNSM-155 fibre from Fasten Fiberoptics) and the hollow-core PBF (HC-1550-02 from Crystal Fiber) were measured experimentally. Measurements were carried out using a Michelson fibre interferometer made of conventional single mode fibres with Faraday rotation mirrors (FRM) employed at the distal ends of both the sensing fibre and reference fibre to avoid polarization induced signal fading. The interferometer was illuminated with a laser with the center wavelength of 1550 (nm) and the line width of 10 (kHz). The HC-1550-02 fibre was incorporated into the sensing arm of the interferometer, with one end spliced to one part of the 3-dB coupler and the other end to the pigtail of the FRM, as shown in Fig. 5.2.

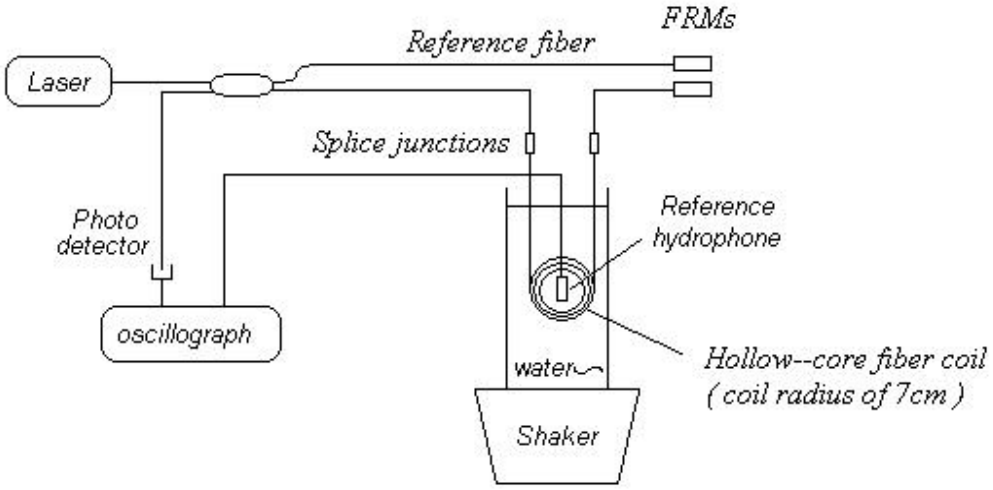

Fig. 5.2 Experimental setup for the acoustic pressure measurements.

A standard hydrophone test tank was used to provide a low-frequency 40~1000 (Hz) test environment. Due to calibrator geometry, the fibre was coiled to a radius of 7 (cm) to fit within the calibrator acoustic field. A standard piezoelectrical hydrophone with the acoustic sensitivity (S_r) of -178 (dB re v/μPa) in the range of 10~10000 (Hz) was used as a reference to calibrate the fibre-optic hydrophone.

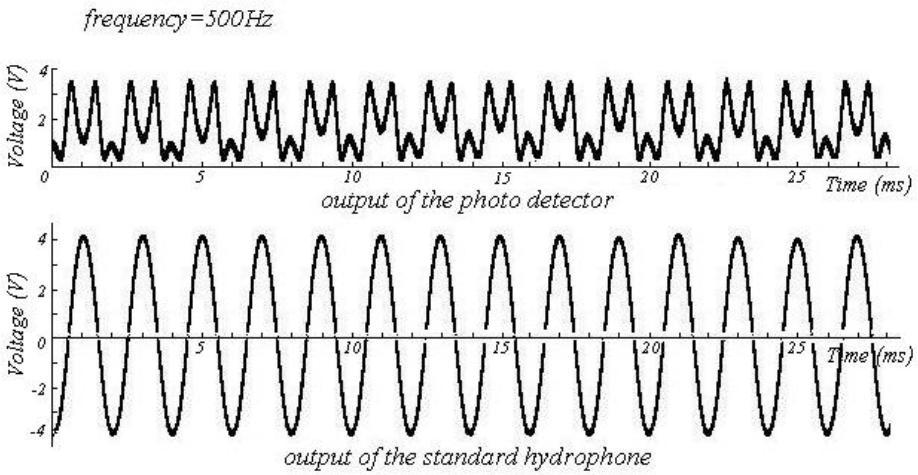

Fig. 5.3 A typical experimental result (f=500Hz), the upper trace is the output from the fibre hydrophone for a peak-peak phase change of 2π; the lower is the standard piezoelectrical hydrophone corresponding to the 2π phase change.

For phase sensitivity measurement at a particular acoustic frequency, the applied acoustic pressure was increased until the induced peak-peak phase shift of the interferometer reached 2π, a value easily determined from waveform displaced in the oscilloscope. When the response of the interferometer reached 2π, the values of the standard reference hydrophone outputs (V_r) were recorded. Fig. 5.3 shows the typical results obtained from a sensing HC-1550-02 fibre of ~5.7 (m) at the acoustic frequency of 500 (Hz).

$$S_m = S_r + 20\log(2\pi / V_r) \tag{5.3}$$

The fibre's acoustic phase sensitivity (S_m) was then calculated as Eq. (5.3). From Eq. (5.2) and (5.3) the acoustic NR of the fibre can thus be determined by Eq. (5.4), where the -6dB is due to the measurement which was taken with a Michelson interferometer, in which the light went through the sensing fibre twice.

$$NR = S_m - 20\log(\frac{2\pi n_{eff} L}{\lambda}) - 6 \tag{5.4}$$

The experiment was repeated for different acoustic frequencies and the measured frequency responses for the hollow-core PBF is shown in Fig. 5.4. For comparison, the frequency response of the conventional silica fibre was also measured with a similar experimental setup and was also shown in Fig. 5.4. The average value of NR over 200~1000 (Hz) for the HC-1550-02 fibre is -334.4 (dB re μPa^{-1}), which is about 15dB higher than that of the HNSM-155 fibre. These experimental results agree well to the theoretical ones as summarized in Table. 5.2.

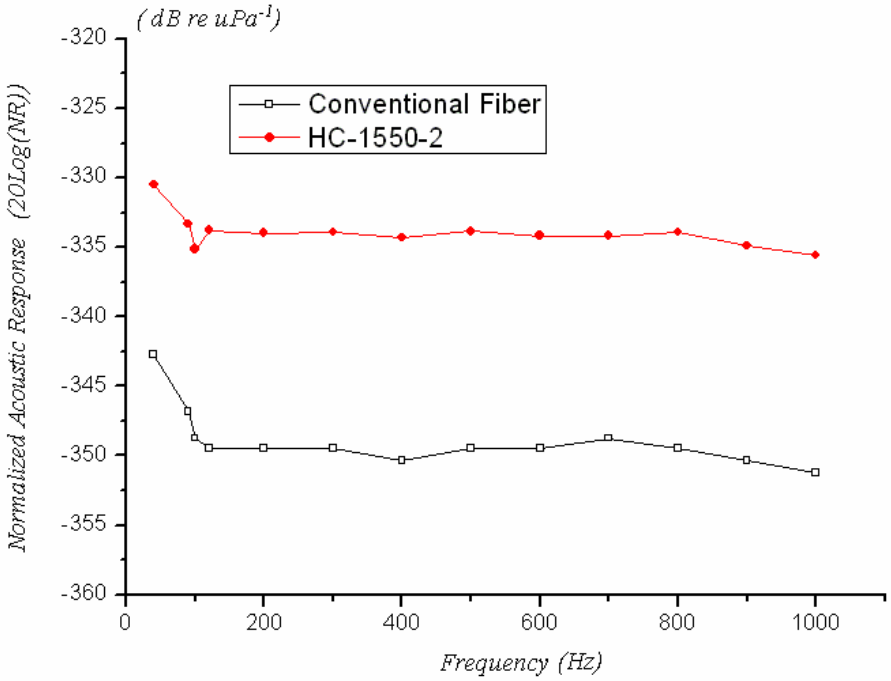

Fig. 5.4 Measured NRs of conventional HNSM fibre and HC-1550-02 fibre as the function of frequency.

Table 5.2 Measured NRs and predicted NRs of the conventional fibre and the hollow-core PBF

	Conventional Fibre (HNSM-155)	Hollow-core PBF (HC-1550-02)
Predicted NRs (dB re 1/ μPa)	-348.5	-333.1
L (m)	9.5	5.7
n_{eff}	1.46	0.997
Measured NRs (dB re 1/ μPa)	-349.4	-334.4

1.3 Summary

We measured the phase sensitivities of the NL-3.3 fibre and the HC-1550-02 fibre to

axial strain, and the normalized responsivity (NR) of the HC-1550-02 fibre to acoustic pressure in experiment. The experimental results show that the normalized phase sensitivities of HC-1550-02 and NL-3.3 fibre to axial strain are 0.9815±0.004 (ε^{-1}) and 0.7813±0.006 (ε^{-1}) respectively, and the NR of HC-1550-02 fibre to acoustic pressure is -334.4 (dB re μPa^{-1}). Those values agree well to the predicted values as shown in Chapter 2 and 3.

Chapter 6

Hollow-core PBF Polarization Controller

In this chapter, we demonstrate a polarization controller (PC) made by applying pressures laterally to three segments of a hollow-core PBF. As discussed in Section 3.4 of Chapter 3, the lateral pressures result in the asymmetric deformations of the fibre's hollow core and air-silica cladding, and generate variable linear birefringence along the hollow-core PBF, which is adjustable by controlling the magnitude of the applied pressure.

6.1 Experimental Setup and Principle of Hollow-core PBF PC

The experimental setup of the hollow-core PBF polarization controller is shown in Fig. 6.1. Light from a distributed feedback laser emitting at the wavelength of 1550 (nm) was launched into a polarizer. The output from the polarizer was coupled into the hollow-core PC and the output end of the hollow-core PBF was spliced to a section of conventional SMF-28 fibre, which was further connected to a commercial polarization analyzer that allows the state of polarization (SOP) of output light to be traced on the Poincare sphere.

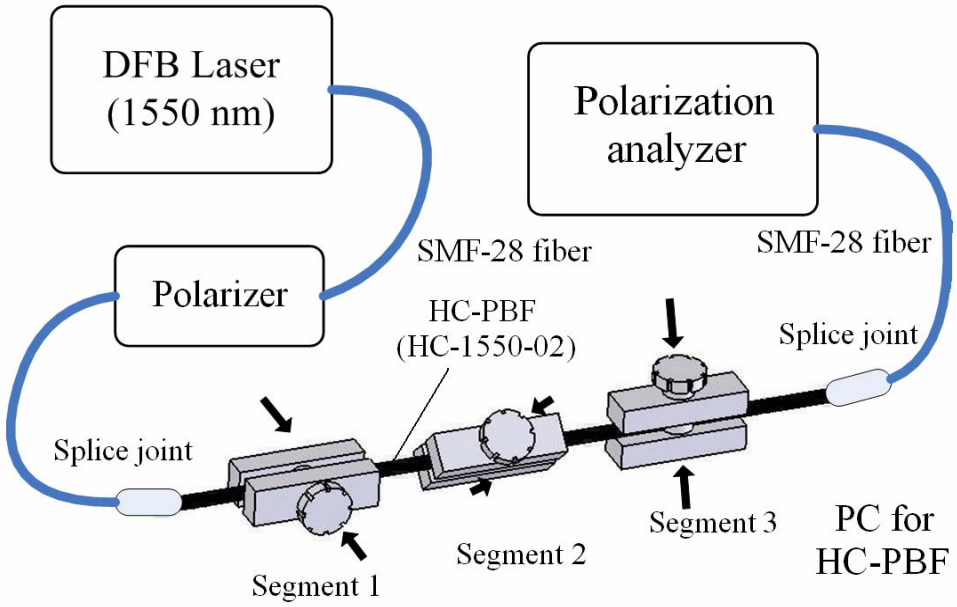

Fig. 6.1 Experimental setup of the hollow-core PBF PC.

The PC was made on a section of hollow-core PBF (HC-1550-02 fibre) by applying lateral pressures to three segments of fibre, and the directions of pressurization change by 45º from one segment to another as shown in Fig. 6.1. Each pressurized segment had a length of ~20 (mm) and was fixed between two plates to which variable pressure could be applied.

As discussed in Section 3.4, the lateral pressure can result in deformations of the hollow-core PBF's hollow core as well as the cells in the fibre's air-silica cladding, both of which induce linear birefringence to the hollow-core PBF. Using the results shown in Fig. 3.22, it can be calculated that: for a pressurized segment length of ~20 (mm), a phase delay ($\Delta\varphi$) of 2π between two orthogonal linear polarization can be achieved with an applied lateral pressure of ~$7.5*10^6$ (Pa) for the HC-1550-02 fibre and the required pressure will be reduced to ~$1.25*10^6$ (Pa) when the thickness of the outer silica cladding is reduced to 10 (μm).

Discussion of the light SOP out of the hollow-core PBF PC may be facilitated by a representation of the SOP on the surface of a Poincare sphere. As shown in Fig. 6.2, points *P* and *Q* on the Poincare sphere represent horizontal and vertical states of a fixed laboratory reference system, while points *H* and *V* represent ±45º states. *R* and *L* represent right- and left-handed circular states. The action of a variable linear birefringence segment is to rotate the SOP on the sphere surface about an axis of *OA*, where *OA* is in the equatorial plane and the angle between *OA* and *PQ* represents the direction of the applied lateral pressure in the reference system [42].

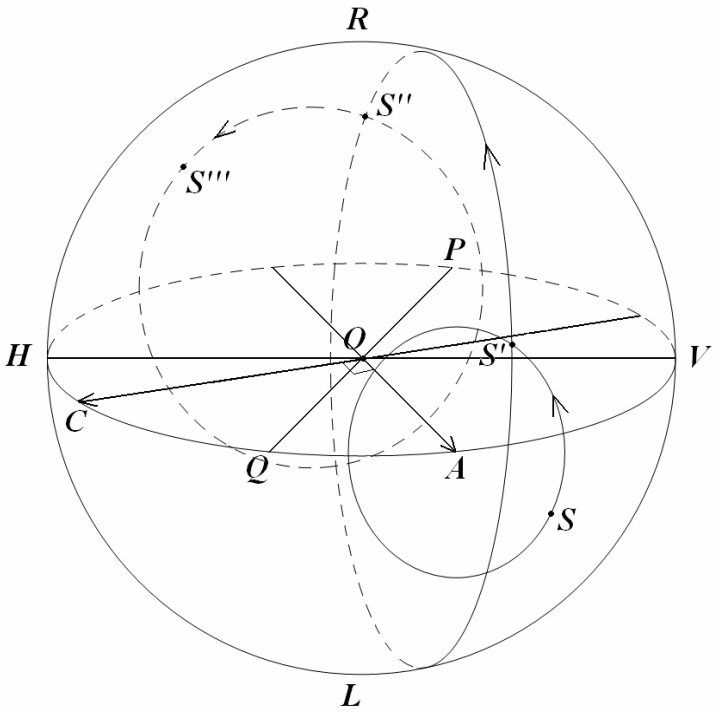

Fig. 6.2 Evolution of the state of polarization on the Poincare sphere surface.

For an arbitrary input SOP (*S*) on the surface of Poincare sphere shown in Fig. 6.2, the first pressure segment rotates *S* along the circle *SS'*, where *S'* is the SOP of the output light from the first segment and it can be modified by the lateral pressure to any point in the circle. Then light *S'* enters Segment 2, where another lateral pressure is applied with the direction of 45º differing from Segment 1. Thus the SOP (*S''*) of

the light out of Segment 2 rotates on the sphere surface about the axis of *OC*, where *OC* is also in the equatorial plane of the sphere and vertical to *OA*. The third segment, again, rotates the *S''* on the sphere surface about the axis of *OA*. Fig. 6.2 gives a visualization of the evolution of the SOP through the three lateral pressure segments of the PC. It can be seen that the PC can transform a general input state *S* into any output state *S'''*.

6.2 Measurement and Results

In experiment, a hollow-core PBF PC was constructed and tested. Fig. 6.3 shows the photograph of the PC based on HC-1550-02 fibre.

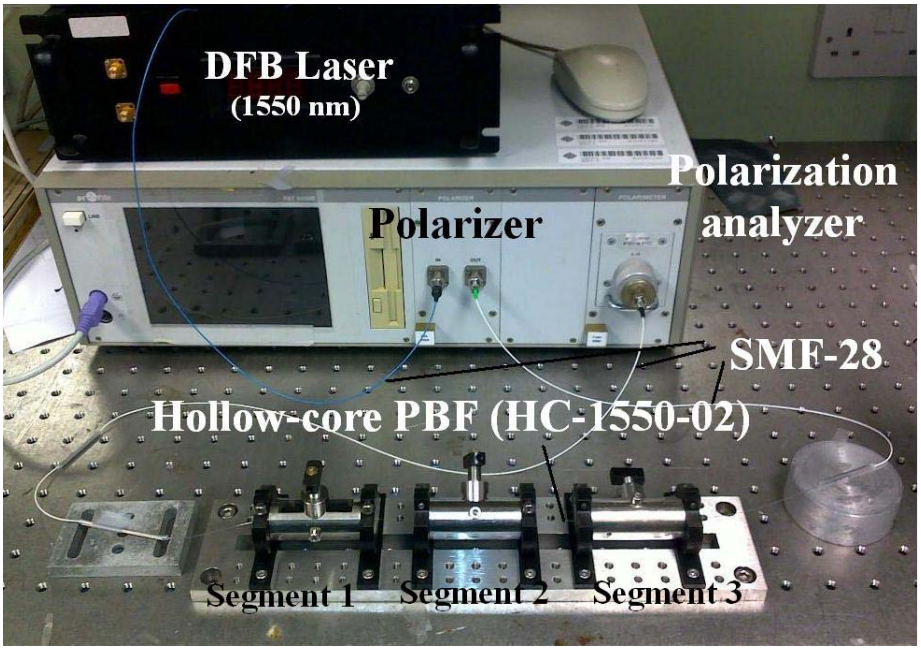

Fig. 6.3 Photograph of the hollow-core PBF PC.

To test the performance of the hollow-core PBF PC, the pressure applied to segment 1 was firstly increased gradually, while the pressures to other two segments were kept constant. The output SOPs from the PC were plotted in Fig. 6.4 and the

evolution of the output SOP follows approximately a circle, which is in agreement with the theoretical predictions. The deviation from the ideal circular trajectory may be due to the inherent birefringence of the HC-PBF [41], which would be reduced largely by the advanced fibre manufacturing technology.

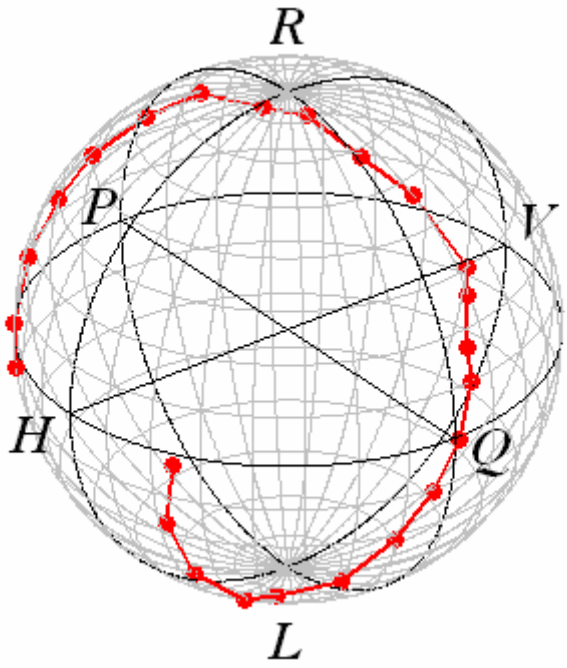

Fig. 6.4 Test results of the hollow-core PBF PC when the pressure applied to the first segment was varied gradually.

Furthermore, the deviation in Fig. 6.4 would have no detrimental effects on the performance of the hollow-core PC. This was verified by varying randomly the pressures applied to all the three segments, when the input light was kept at a fixed linearly polarized state. The output polarization states from the PC illustrated a good coverage of all the possible polarization states as shown in Fig. 6.5. Similar results were obtained for other input SOPs

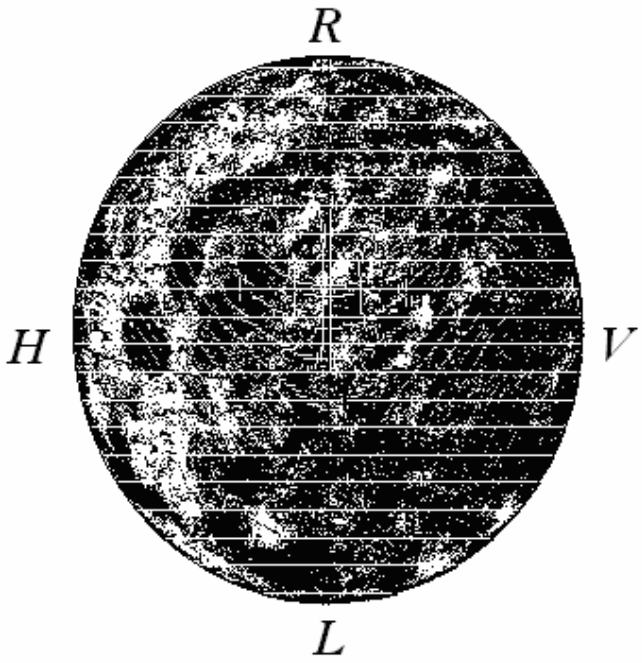

Fig. 6.5 Test results of the hollow-core PBF PC the pressures applied to all the three segments were varying randomly.

6.3 Summary

In this chapter, we have demonstrated a hollow-core PBF polarization controller by pressurizing three segments of the fibre. This polarization controller was tested experimentally, and the polarization states of its output show a good coverage of all the possible states of polarization on the surface of the Poincare sphere, indicating that a universal control of the polarization state may be obtained. This scheme may be applicable to hollow-core PBF with little or no inherent birefringence.

Chapter 7

Hybrid PCF Sensors and Possible Applications

7.1 Experimental Setup

In experiments, an optic fibre Sagnac interferometer (OFSI) was constructed to measure the birefringence of the hybrid PCF and its birefringence responses to axial strain and temperature variation. As shown in Fig. 7.1, a section of HYBRID2007_2PBG_OD151 fibre manufactured by University of Bath was used as the sensing element in OFSI. The two ends of the hybrid PCF were spliced to two ports of a 3-dB single mode fibre coupler.

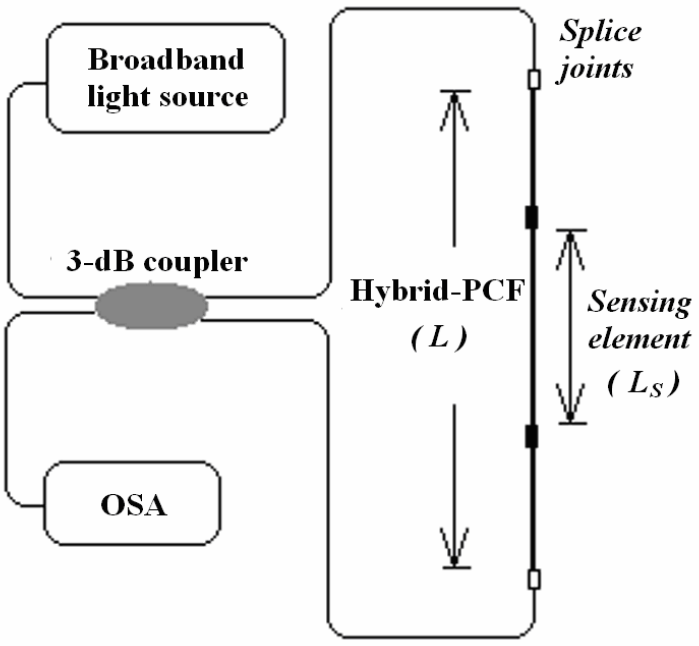

Fig. 7.1 Experimental setup for birefringence measurement.

Total insertion loss and fibre attenuation are about 10 dB and the extinction ratio of system nearly 20 dB. The Sagnac interferometer is illuminated by a broadband light source with the wavelength range from 600 - 1700 (nm), and the transmission spectrum of the OFSI, as shown in Fig. 7.2, is measured by an optical spectrum analyzer (OSA), which has the wavelength resolution of 10 (pm).

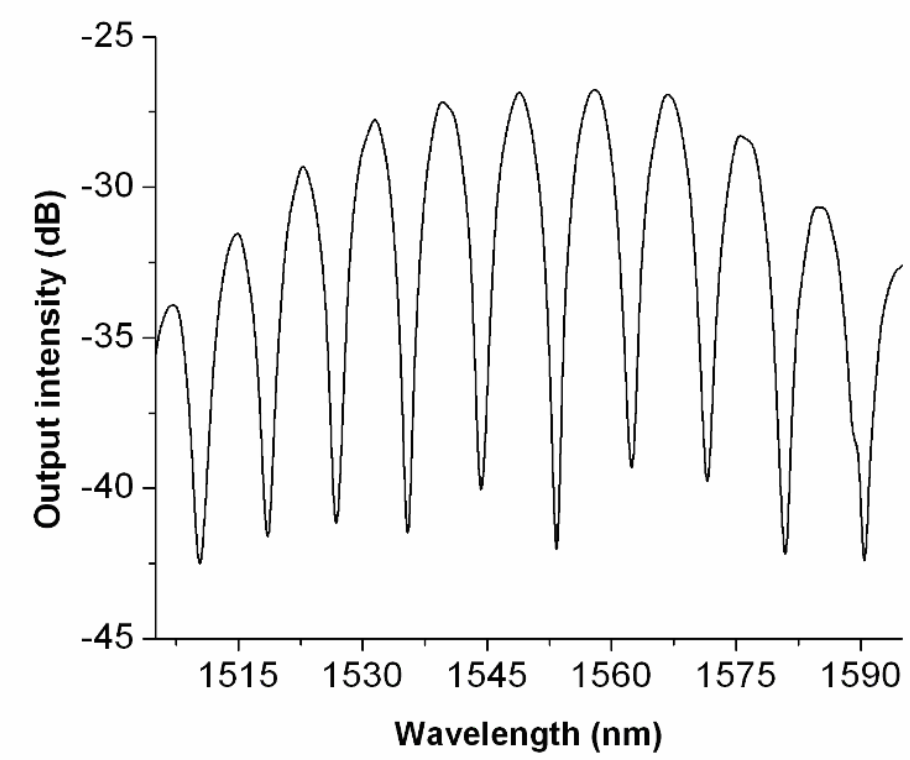

Fig. 7.2 Transmission spectrum of the hybrid PCF Sagnac interferometer.

The principle of operation of the OFSI has been described in Ref. [97] and [98]. The interference of the counter-propagating waves will happen in the coupler, and its interferometric fringe depends on the birefringence of the fibre loop. Thus the system transmission spectrum is wavelength dependent as shown in Fig. 7.2. Ignoring the insertion losses and attenuation of the fibre, the transmission spectrum of the Sagnac interferometer can be written as Eq. (7.1), where $\varphi=2\pi LB/\lambda$ is the

phase difference between the fast and slow beams, L is the total length of the hybrid PCF, λ is the wavelength of light. Then the minimum of the transmission wavelength (λ_{min}) can be written as Eq. (7.2), where k is an integer.

$$T = [1 - \cos(\varphi)] / 2 \tag{7.1}$$

$$\lambda_{\min} = BL / k \tag{7.2}$$

It can be seen that the transmission spectrum is a periodic function of wavelength, and the distance (*Dis*) between the adjacent transmission minimums can be written as Eq. (7.3).

$$Dis = \lambda_{\min}^2 / (BL) \tag{7.3}$$

In the experiments, the sensing element of hybrid PCF used for strain and temperature measurements has the length of L_s. The shift of minimum transmission wavelength ($\Delta\lambda_{min}$) induced by the measureand "*X*" may be generally expressed as Eq. (7.4).

$$\Delta\lambda_{\min} = (\Delta LB + \Delta BL_s) / k \tag{7.4}$$

In Eq. (7.4), ΔL is the variation of the fibre length, and ΔB is the change of birefringence of the hybrid PCF due to "*X*". Substituting Eq. (7.2) into Eq. (7.4), the sensitivity of the hybrid PCF Sagnac interferometer to axial strain ($\varepsilon=\Delta L/L_s$) and temperature variation can be written as equations (7.5) and (7.6) respectively.

$$S_\varepsilon = \frac{\Delta\lambda_{\min}}{\varepsilon} = \frac{\lambda_{\min} L_s}{BL}(B + \frac{\Delta B}{\varepsilon}) \tag{7.5}$$

$$S_T = \frac{\Delta\lambda_{\min}}{\Delta T} = \frac{\lambda_{\min} L_s}{L}(\alpha_0 + \frac{1}{B}\frac{\Delta B}{\Delta T}) \tag{7.6}$$

7.2 Responses to Axial Strain

In our experiments, we used a piece of hybrid PCF (HYBRID2007_2PBG_OD15) with the total length of L=1093 (mm) and sensing length of L_s=419 (mm). The parameters of this hybrid PCF is listed in Table 4.1. The transmission spectrum of this hybrid PCF OFSI is shown in Fig. 7.2, and the distance between the adjacent transmission minimums at the wavelength of ~1550 (nm) is measured to be ~8.79 (nm). Using Eq. (7.2), the birefringence of this hybrid PCF at the wavelength of 1550nm can be calculated to be ~$2.498*10^{-4}$. This value agrees well with the predicted birefringence shown in Section 4.2.

For the strain-sensitivity measurement, a standard strain test-rail was used to provide the axial strain to the hybrid PCF. One end of the sensing fibre was fixed on the rail, while the other end was computer controlled to move a known distance (ΔL), so the axial strain acting on the sensing fibre can be calculated as $\varepsilon=\Delta L/L_s$. Fig. 7.3 shows several measured transmission spectrum around the minimum wavelength of 1550 (nm). It can be seen that as the applied axial strain increases, the spectrum shifts to the longer wavelength.

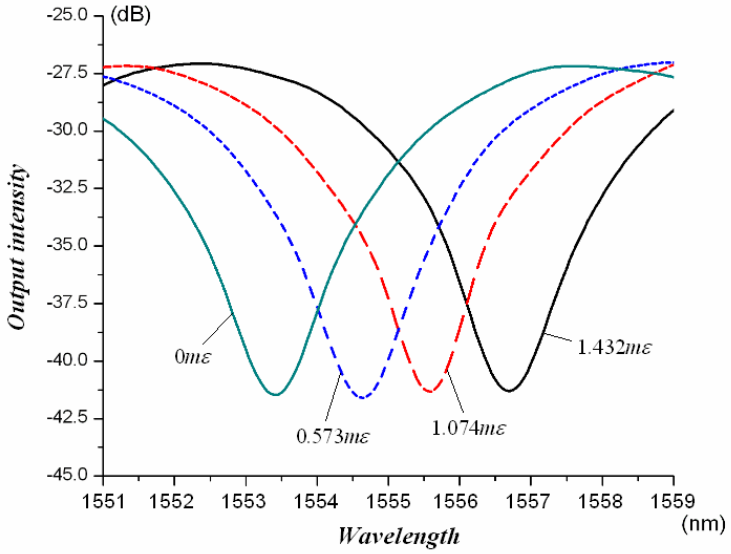

Fig. 7.3 Measured transmission spectrum due to different applied axial strains.

The measured spectrum minimums and their linear fitting are shown in Fig. 7.4. The experimental data show the hybrid PCF OFSI has the strain sensitivity of ~2.01 (nm/mε). Substituting this value as well as the birefringence of this hybrid PCF into Eq. (7.5), $\Delta B/\varepsilon$ of such hybrid fibre can be calculated to be ~$6.04*10^{-4}$ (ε^{-1}) which agrees well with the predicted value of $5.663*10^{-4}$ (ε^{-1}) discussed in Section 4.3.1.

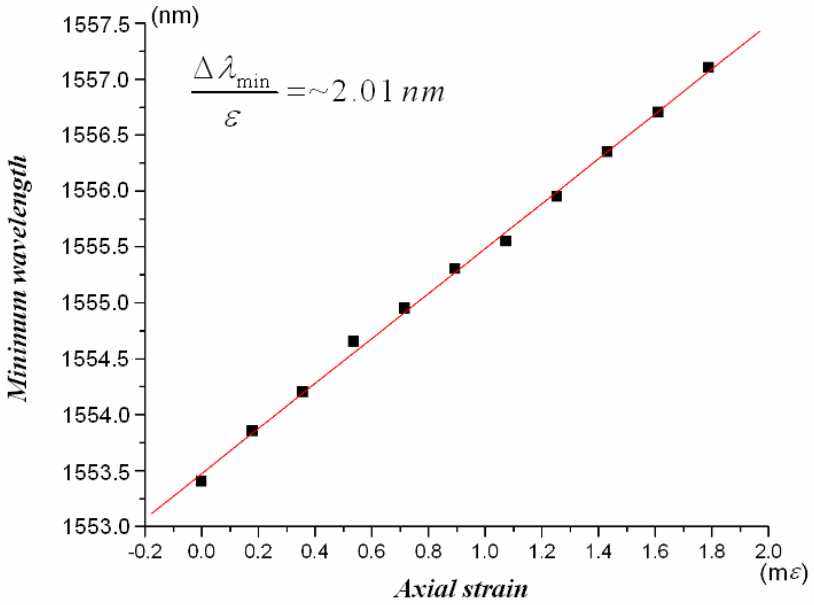

Fig. 7.4 Spectrum minimums of the OFSI as the function of the applied axial strain.

7.3 Responses to Temperature

In the temperature-sensitivity measurement of such hybrid PCF OFSI, the sensing hybrid PCF was fitted within a temperature controlled container and the temperature was controlled and recorded by a digital thermograph. It shows when the temperature increased from 30 ºC to 90 ºC, the spectrum minimum wavelength (around 1550 nm) of the OFSI moved to a shorter wavelength. The measured shifts of the spectrum minimum wavelength as the function of the test temperature are shown in Fig. 7.5. The linear fitting of the experimental data gives a temperature sensitivity of ~-0.334 (nm/K). Using Eq. (7.6), $\Delta B/\Delta T$ of this hybrid PCF can be calculated to be ~-1.406*10^{-7} (K^{-1}), which agrees well with the predicted temperature-sensitivity of -1.844*10^{-7} (K^{-1}) discussed in Section 4.3.2.

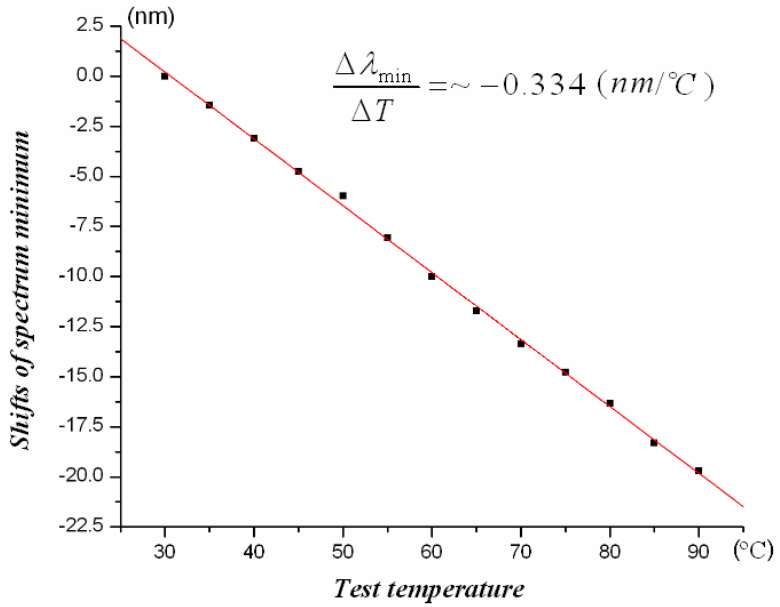

Fig. 7.5 Shifts of the spectrum minimum as the function of test temperature.

7.4 A Design of Hybrid PCF and its Applications

In this section we show a proposed design for the hybrid PCF, which can generate

high birefringence sensitivity to temperature as well as low birefringence sensitivity to axial strain. Such proposed hybrid PCF may be used to replace the conventional HB-fibre in fibre-optic temperature sensors [37] or temperature modulated devices [43] to enhance the system performances.

In the hybrid PCF, the response of birefringence to temperature is induced by three effects as shown in Section 4.2: 1) the temperature-induced geometry term, 2) material index term and 3) built-in stress term, while the birefringence response of this hybrid fibre to axial strain can only be induced by the geometry term and material index term. Thus a hybrid PCF design is proposed as Fig. 7.6, which has one row of its air holes Ge-doped, and another two rows of B-doped rods. The Ge-doped and B-doped regions have the same diameters and high-indexes, and thus the profile of the hybrid PCF can be designed to be symmetric in both geometry and material index distribution. The birefringence of the hybrid PCF is mainly induced by the built-in stress, which is induced in the fibre manufacture process because of the difference of expansion coefficients between the Ge-doped and B-doped rods.

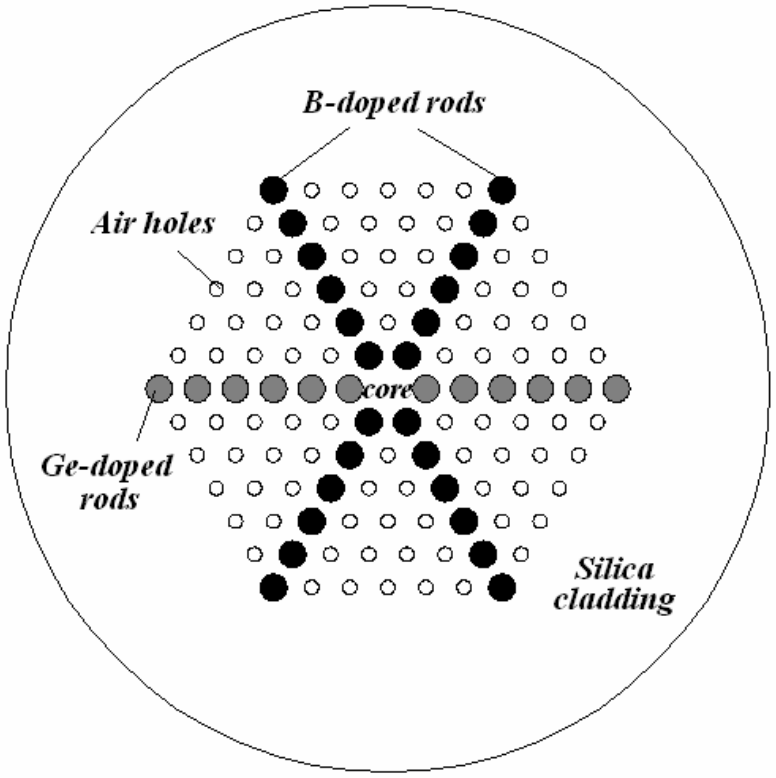

Fig. 7.6 Schematics of designed hybrid PCF.

When the proposed hybrid PCF is subject to axial strain, the geometric deformation of the fibre is symmetric because the elastic properties of silica do not depend strongly on its doped composition, and the stain-induced index change of fibre materials is also symmetric because both the Ge-doped and B-doped rods have similar strain-optic coefficients with the pure silica background. Thus for this hybrid PCF, both of the two factors of the birefringence response to axial strain would be small and the proposed hybrid PCF would have low birefringence sensitivity to axial strain. When the fibre is subject to temperature variation, although the geometry and material index factor are small for the same reasons, the built-in stress factor for the birefringence response of this hybrid PCF has high value because of the difference of expansion coefficients between the Ge-doped and B-doped rods. So the proposed hybrid PCF will keep its high sensitivity to temperature.

7.5 Summary

In this chapter, we have investigated experimentally the birefringence properties of hybrid PCF and the birefringence responses of this hybrid PCF to axial strain and temperature variations. The experimentally measured birefringence and birefringence responses to axial strain and temperature variation are: ~$2.498*10^{-4}$, ~$6.04*10^{-4}$ (ε^{-1}) and ~$-1.406*10^{-7}$ (K^{-1}) respectively. These values agree well with our theoretical predictions shown in Chapter 4. Using the flexibility of a novel hybrid PCF design, the proposed hybrid fibre may achieve high birefringence response to temperature as well as low response to axial strain, which make it have some applications in the fibre-optic sensors and devices.

Chapter 8

Conclusion and Further Work

8.1 Conclusion

In this dissertation, we have investigated theoretically and experimentally the responses of PCFs to external measurands, including axial strain, acoustic pressure, temperature, and lateral pressure.

We constructed three theoretical models for solid-core PCFs, hollow-core PBFs and hybrid PCFs respectively. The theoretical models can be used to simulate the physical deformations and optical responses of exiting PCFs due to strain, pressure and temperature as well as to predict the deformations/responses of PCFs with proposed fibre designs. Therefore, they are very useful for the designs of PCF-based fibre sensors or devices.

Using these theoretical models, we investigated the phase sensitivities of both solid-core PCFs and hollow-core PBFs to axial strain. The simulation shows that: 1) the length term for both of these two types of PCFs can be normalized to unit; 2) the index term for solid-core PCFs is mostly determined by the strain-optic effect of the fibre silica core, while for hollow-core PBFs, the index term is much smaller because the core of the hollow-core PBF is air. The experimental measurements show the NL-3.3 fibre (one type of solid-core PCF) has the phase sensitivity of 0.7813±0.006 (ε^{-1}) to axial strain, whereas phase sensitivity of the HC-1550-02 fibre (one type of hollow-core PBF) is 0.9815±0.004 (ε^{-1}). These experimental results agree well with the predictions, and are useful to guide the design of PCF-based strain sensors.

We studied the normalized responsivity (NR) of hollow-core PBFs to acoustic pressure. In experiment, measured NR of the HC-1550-02 fibre shows a ~15dB improvement as compared with conventional silica fibres. This NR improvement is because the air core and air-silica cladding of the hollow-core PBF decrease the silica percentage of the fibre's profile, which makes the hollow-core PBF much more flexible than conventional silica fibres. The simulation results predicted that NR of hollow-core PBF can be enhanced further by decreasing the silica percentage of the fibre's profile. To achieve this, two methods can be applied: one method is to decrease the thickness of the silica outer cladding of the hollow-core fibre, and the other is to increase the air-filling ratio of its air-silica inner cladding. By using these two methods, hollow-core PBF with high acoustic NR of ~280 (dB re μPa^{-1}) is predicted. This great enhancement NR of hollow-core PBF can simplify the sensor configuration of fibre hydrophones, and also benefit hydrophone multiplexing.

We investigated the birefringence of hollow-core PBFs due to lateral pressure. The simulation shows that the pressure-induced birefringence of hollow-core PBFs can be modified by the magnitude of the applied lateral pressure. Using this phenomenon, a new scheme for hollow-core PBF polarization controller (PC) is constructed by applying three segments of lateral pressures to a section of HC-1550-02 fibre. This new scheme for hollow-core PBF PC is verified by the experiments, and the hollow-core PBF PC shows good performance of a universal PC. The difference between this new scheme and the former scheme for hollow-core PBF PC is that the new scheme is applicable to hollow-core PBF with little or no inherent birefringence, which may broaden the bandwidth of hollow-core PBF PCs.

We constructed a theoretical model for hybrid PCFs, which can be used to simulate

the birefringence properties of hybrid PCFs, and their responses to external measurands, including axial strain and temperature. The measurement results from one type of hybrid PCF show good agreement with the simulation results. The theoretical model is useful for analyzing the birefringence properties of hybrid PCFs, and can be used to guide the design of strain or temperature sensors which use hybrid PCFs as the sensing elements.

8.2 Further Work

The NR of hollow-core PBF may be improved further by coating the fibre with air-included polymer material. Air-included polymer material has much smaller Young's modulus and Poisson's ratio than silica material, which make the coated hollow-core PBF more flexible. According to the theoretical predictions, the NR of the hollow-core PBF coated with air-included polymer is determined by the thickness of air-included polymer coating and its air-included ratio. Predictions show that the NR of such coated hollow-core PBF can reach as high as ~280 (dB re μPa^{-1}), which is about 60 dB higher than conventional silica fibres. Such high NR may be useful for the simplicity and multiplexing of the fibre-optic hydrophone transducers.

Other hollow-core PBF sensors and devices based on lateral pressures may be investigated further. For example, when a section of hollow-core PBF is subjected to a periodical lateral pressure, a pressure-induced long period grating (LPG) may be realized on the hollow-core PBF. This pressure-induced LPG may be used as strain or temperature sensor. And because the LPG can be modulated by the magnitude of the applied lateral pressure, an in-fibre hollow-core PBF switch may be constructed based on the pressure-induced LPG.

References:

[1] A. D. Kersey, “A review of recent developments in fiber optic sensor technology,” Optical Fiber Technology, 2, 291-317 (1996)

[2] B. Lee, “Review of the present status of optical fiber sensors,” Optical Fiber Technology, 9, 57-79 (2003)

[3] Culshaw B and Dakin J, Optical Fiber Sensors, Artech House, Boston, (1988)

[4] K. T. V. Grattan, B. T. Meggitt, Optical Fiber Sensor Technology, Kluwer Academic publisher, Boston (1999)

[5] F. T. S. Yu, S. Yin, Fiber Optic Sensors, Dekker, New York (2002)

[6] A. Othonos, K. Kalli, Fiber Brag Gratings-Fundamentals and Applications in Telecommunications and Sensing, Artech House, Boston (1999)

[7] M. D. Marazuela, M. C. Moreno-Bondi, Fiber-optic biosensors-an overview, Anal. Bioanal, Chem. 372, 664-682 (2002)

[8] R. A. Bergh, H. C. Lefevre, and H. J. Shaw, “An overview of fiber-optic gyroscopes,” J. Lightwave Technol. 2, 91-107 (1984)

[9] T. G. Giallorenzi, J. A. Bucaro, A. Dandridge, G. H. Sigel, J. H. Cole, S. C. Rashleigh, and R. G. Priest, “Optical fiber sensor technology,” IEEE J. Quantum Electron. 18, 626-65 (1982)

[10] W. Jin, H. F. Xuan, and H. L. Ho, “Sensing with hollow-core photonic bandgap fibers,” Meas. Sci. Technol. 21, 094014 (2010)

[11] R. H. Stolen and R. P. D. Paula, “Single-mode fiber components,” Proceedings of the IEEE, 75, 1498-1511 (1987)

[12] A. W. Snyder and J. D. Love, Optical Waveguide Theory. Chapman and Hall, London (1983)

[13] W. Eickhoff, “In-line fiber-optic polarizer,” Electron. Lett. 16, 762-764 (1980)

[14] R. A. Bergh, H. C. Lefevre, and H. J. Shaw, “Single-mode fiber optic polarizer,”

Opt. Lett. 5, 479-481 (1980)

[15] R. A. Bergh, G. Kotler, and H. J. Shaw, “Single-mode fiber-optic directional coupler,” Electron. Lett. 16, 260-261 (1980)

[16] M. S. Whalen and K. L. Walker, “In-line optical fiber filter for wavelength multiplexing,” Electron. Lett. 21, 724-725 (1985)

[17] R. H. Stolen, A. Ashkin, W. Pleihel, and J. M. Dziedzic, “In-line fiber-polarization-rocking rotator and filter”, Opt. Lett. 9, 300-302 (1984)

[18] E. H. Turner and R. H. Stolen, “Fiber Faraday circulator or isolator,” Opt. Lett. 6, 322-323 (1981)

[19] K. Nosu, S. C. Rashleigh, H. F. Taylor, and J. F. Weller, “Acousto-optic frequency shifter for single-mode fibers,” Electron. Lett. 19, 816-818 (1983)

[20] L. Reekie, R. J. Mears, S. B. Poole, and D. N. Payne, “Tunable single-mode fiber lasers,” J. Lightwave Technol. 4, 956-960 (1986)

[21] C. K. Kirkendall and A. Dandridge, “Overview of high performance fiber-optic sensing,” J. Phys. D 37, 197-216 (2004)

[22] J. A. Bucaro, H. D. Dardy, and E. F. Carome, “Fiberoptic hydrophone,” J. Acoustic. Soc. Am. 62, 1302-1304 (1997)

[23] J. A. Bucaro, Fiber Optic Acoustic Transduction, Academic, New York (1982)

[24] G. F. McDearmon, “Analysis of a push-pull fiber optic hydrophone,” J. lightwave Technol. 5, 647-652 (1987)

[25] S. S. Patrick et al. “Responsivity and stability of air-backed, polycarbonate mandrel based fiber optic hydrophones,” Naval Research Laboratory

[26] J. H. Cole, R. L. Johnson, and P. G. Bhuta, “Fiber topic detection of sound,” J. Acoust. Soc. Am. 62, 1136-1138 (1977)

[27] G. B. Hocker, “Fiber optic acoustic sensors with composite structure: an analysis,” Appl. Opt. 18, 3679-3683 (1979)

[28] N. Lagakos, E. U. Schnaus, J. H. Cole, J. Jarzynski, and J. A. Bucaro,

"Optimizing fiber coatings for interferometric acoustic sensors," IEEE J. Quantum Electron. 18, 683-689 (1982)

[29] B. Budiansky, D. C. Drucke, G. S. Kino, and J. R. Rice, "Pressure sensitivity of a clad optical fiber," Appl. Opt. 18, 4085-4088 (1979)

[30] R. Hughes and J. Jarzynski, "Static pressure sensitivity amplification in intererometric fiber-optic hydrophones," Appl. Opt. 19, 98-107 (1980)

[31] J. H. Cole, C. Sunderman, A. B. Tveten, C. Kirkendall, and A. Dandridge, "Preliminary investigation of air-included polymer coating for enhanced sensitivity of fiber-optic acoustic sensors," 15th Optical Fiber Sensors Conference (2002)

[32] J. H. Cole, S. Motley, J. Jarzynski, A. B. Tveten, C. Kirkendall, and A. Dandridge, "Air-included polymer coating for enhanced sensitivity of fiber-optic acoustic sensors," 16th Optical Fiber Sensors Conference (2003)

[33] J. Noda, K. Okamoto, and Y. Sasaki, "Polarization-maintaining fibers and their applications," IEEE J. of Lightwave Technol. 4, 1071-1089 (1986)

[34] F. Zhang, and J. W. Y. Lit, "Polarization characteristics of double-clad elliptical fibers" Appl. Opt. 29, 5336-5342 (1990)

[35] K. Suzuki, H. Kubota, S. Kawanishi, M. Tanaka and M. Fujita, "Optical properties of a low-loss polarization-maintaining photonic crystal fiber," J. Lightwave Technol. 19, 495-503 (2001)

[36] Y. Liu, B. Liu, X. Feng, W. Zhang, G. Zhou, S. Yuan, G. Kai and X. Dong, "High-birefringence fiber loop mirrors and their applications as sensors," Appl. Opt. 44, 2382-2390 (2005)

[37] F. Zhang and J. W. Y. Lit, "Temperature and strain sensitivities of high-birefringence elliptical fibers," Appl. Opt. 31, 1239-1243 (1992)

[38] X. Dong and H. Y. Tam, "Temperature-insensitive strain sensor with polarization-maintaining photonic crystal fiber based Sagnac interferometer," Appl. Phys. Lett. 90 151113 (2007)

[39] A. C. S. Jr., F. Luan, C. M. B. Cordeiro, A. K. George and J. C. Knight, “Hybrid photonic crystal fiber,” Opt. Express, 14, 926-931 (2006)

[40] L. Xiao, W. Jin and M. S. Demokan, “Photonic crystal fibers confining light by both index-guiding and bandgap-guiding: hybrid PCFs,” Opt. Express, 15, 15637-15647 (2007)

[41] R. Ulrich and A. Simon, “Polarization optics of twisted single-mode fibers,” Appl. Opt. 18, 2241 (1979)

[42] M. Johnson, “In-line fiber-optical polarization transformer,” Appl. Opt. 18, 1288 (1979)

[43] E. R. Lyons and H. P. Lee, “An electrically tunable all-fiber polarization controller based on deposited thin-film microheaters,” IEEE Photon. Technol. Lett. 14, 1318 (2002)

[44] R. F. Cregan, B. J. Mangan, J. C. Knight, T. A. Birks, P. S. J. Russell, P. J. Roberts and D. C. Allan, “Single-mode photonic band gap guidance of light in air,” Science 285, 1537-1539 (1999)

[45] L. Xiao, M. S. Demokan, W. Jin, Y. Wang and C. L. Zhao, “Fusion splicing photonic crystal fibers and conventional single-mode fibers: micro-hole collapse effect,” J. Lightwave Technol. 25 3563 (2007)

[46] L. Xiao, W. Jin, and M. S. Demonkan, “Fusion splicing small-core photonic crystal fibers and single mode fibers by repeated arc discharges,” Opt. Lett. 32, 115-117 (2007)

[47] B. Bourliaguet, C. Pare, F. Emond, A. Croteau, A. Proulx, R. Vallee, “Microstructured fiber splicing, ” Opt. Express 11, 3412-3417 (2003)

[48] H. F. Xuan, W. Jin, J. Ju, Y. P. Wang, M. Zhang, Y. B. Liao, and M. H. Chen, “Hollow-core photonic bandgap fiber polarizer,” Opt. Lett. 33 845 (2008)

[49] Y. P. Wang, W. Jin, J. Ju, H. F. Xuan, H. L. Ho, L. M. Xiao, and D. N. Wang, “Long period gratings in air-core photonic bandgap fibers,” Opt. Express, 16, 2784

(2008)

[50] Z. Wang, G. Kai, Y. Liu, J. Liu, C. Zhang, T. Sun, C. Wang, W. Zhang, S. Yuan, and X. Dong, “Coupling and decoupling of dual-core photonic bandgap fibers,” Opt. Lett. 30, 2542 (2005)

[51] M. Skorobogatiy, “Transverse light wave circuits in microstructured optical fibers: waveguides,” Opt. Express, 13, 7506 (2005)

[52] M. Terrel, M. J. F. Digonnet, and S. Fan, “Polarization controller for hollow-core fiber,” Opt. lett. 32, 1524 (2007)

[53] J. C. Knight, T. A. Birks, P. S. J. Russell, and D. M. Atkin, “Pure silica single-mode fiber with hexagonal photonic crystal cladding,” Optical Fiber Communication Conference, San Jose (1996)

[54] J. C. Knight, T. A. Birks, P. S. J. Russell, and D. M. Atkin, “All-silica single-mode fiber with photonic crystal cladding,” Opt. Lett. 21, 1547-1549 (1996)

[55] T. A. Birks, J. C. Knight, and P. S. J. Russell, “Endlessly single-mode photonic crystal fiber,” Opt. Lett. 22, 961-963 (1997)

[56] J. C. Knight, T. A. Birks, R. F. Cregan, P. S. J. Russell, and J. P. Sandro, “Large mode are photonic crystal fiber,” Electron. Lett. 34, 1347-1348 (1998)

[57] D. Mogilevtsev, T. A. Birks, and P. S. J. Russell, “Group-velocity dispersion in photonic crystal fibers,” Opt. Lett. 23, 1662-1664 (1998)

[58] R. F. Cregan, B. J. Mangan, J. C. Knight, T. A. Birks, P. S. J. Russell, P. J. Roberts, and D. C. Allan, “Single-mode photonic band gap guidance of light in air,” Science, 285, 1537-1539 (1999)

[59] A. O. Blanch, J. C. Knight, W. J. Wadsworth, J. Arriaga, B. J. Mangan, T. A. Birks, and P. S. J. Russell, “Highly birefringent photonic crystal fibers,” Opt. Lett. 25, 1325-1327 (2000)

[60] B. J. Mangan, J. C. Knight, T. A. Birks, P. S. J. Russell, and A. H. Greenaway, “Experimental study of dual-core photonic crystal fiber,” Electron. Lett. 36, 1358-

1359 (2000)

[61] P. S. Russell, “Photonic-crystal fibers,” IEEE J. Lightwave Technol. 24, 4729 (2006)

[62] H. K. Kim, M. J. F. Digonnet, and G. S. Kino, “Air-core photonic-bandgap fiber-optic gyroscope,” IEEE J. Lightwave Technol. 24, 3169 (2006)

[63] K. Koch, “Photonic crystal fiber technology: a comparison with conventional optical fiber,” Photonic Applications Systems Technologies Conference, San Francisco (2004)

[64] L. Michaille, C. R. Bennet, D. M. Taylor, T. J. Shepherd, J. Broeng, H. R. Simonsen, and A. Petersson, “Phase locking and supermode selection in multicore photonic crystal fiber lasers with a large doped area,” Opt. Lett. 30, 1668-1670 (2005)

[65] W. J. Wadsworth, R. M. Percival, G. Bouwmans, J. C. Knight, T. A. Birks, T. D. Hedley, and P. S. J. Russell, “Very high numerical aperture fibers,” IEEE Photon. Technol. Lett. 16, 843-845 (2004)

[66] W. J. Wadsworth, R. M. Pericival. G. Bouwmans, J. C. Knight, and P. S. J. Russell, “High power air-clad photonic crystal fiber laser,” Opt. Express 11, 48-53 (2003)

[67] F. Benabid, F. Couny, J. C. Knight, T. A. Birks, and P. S. J. Russell, “Compact, stable and efficient all-fiber gas cells using hollow-core photonic crystal fibers,” Nature, 434, 488-491 (2005)

[68] S. G. Leon-Saval, T. A. Birks, N. Y. Joly, A. K. George, W. J. Wadsworth, G. Kakarantzas, and P. S. J. Russell, “Splice-free interfacing of photonic crystal fibers,” Opt. Lett. 30, 1629-1631 (2005)

[69] W. J. Wadsworth, A. Witkowska, S. G. Leon-Saval, and T. A. Birks, “Hole inflation and tapering of stock photonic crystal fibers,” Opt. Express, 13, 6541-6549 (2005)

[70] Y. P. Wang, L. M. Xiao, D. N. Wang, and W. Jin, “In-fiber polarizer based on a

long-period fiber grating written on photonic crystal fiber," Opt. Lett. 32, 1035-1037 (2007)

[71] H. F. Xuan, W. Jin, J. Ju, Y. P. Wang, M. Zhang, Y. B. Liao, and M. H. Chen, "Hollow-core photonic bandgap fiber polarizer," Opt. Lett. 33, 845-847 (2008)

[72] Y. P. Wang, W. Jin, J. Ju, H. F. Xuan, H. L. Ho, L. M. Xiao, and D. N. Wang, "Long period gratings in air-core photonic bandgap fibers," Opt. Express, 16, 2784 (2008)

[73] G. Kakarantzas, T. A. Birks, and P. S. J. Russell, "Structural long-period gratings in photonic crystal fibers," Opt. Lett. 27, 1013-1015 (2002)

[74] J. H. Lim, K. S. Lee, J. C. Kim, and B. H. Lee, "Tunable fiber gratings fabricated in photonic crystal fiber by use of mechanical pressure," Opt. Lett. 29, 331-333 (2004)

[75] M. J. Renn, R. Pastel, and H. J. Lewandowski, "Laser guidance and trapping of mesoscale particles in hollow-core optical fibers," Phys. Rev. Lett. 82, 1574-1577 (1999)

[76] M. J. Renn, D. Montgomery, O. Vdovin, D. Z. Anderson, C. E. Wieman, and E. A. Cornell, "Laser-guided atoms in hollow-core optical fiber," Phys. Rev. Lett. 75, 3253-3256 (1995)

[77] F. Benabid, J. C. Knight, and P. S. J. Russell, "Particle levitation and guidance in hollow-core photonic crystal fiber," Opt. Express, 10, 1195-1203 (2002)

[78] T. M. Monro, W. Belardi, K. Furusawa, J. C. Baggett, N. G. R. Broderick, and D. J. Richardson, "Sensing with microstructured optical fibres," Meas. Sci. Technol. 12, 854-858 (2001)

[79] W. N. MacPherson, M. J. Gander, R. Mcbride, J. D. C. Jones, P. M. Blanchard, J. G. Burnett, A. H. Greenaway, "Remotely addressed optical fiber curvature sensor using multicore photonic crystal fiber," Opt. Commun. 193, 97-104 (2001)

[80] W. N. Macpherson, J. D. C. Jones, B. J. Mangan, J. C. Knight, and P. S. J.

Russell, “Two-core photonic crystal fiber for Doppler difference velocimetry, ” Opt. Commun. 223, 375-380 (2003)

[81] W. N. Macpherson, E. J. Rigg, J. D. C. Jones, V. V. Ravi Kanth Kumar, J. C. Knight, and P. S. J. Russell, “Finite-element analysis and experimental results for a microstructured fiber with enhanced hydrostatic pressure sensitivity,” J. Lightwave Technol. 23, 1227-1231 (2005)

[82] H. K. Kim, V. Dangui, M. Digonment, and G. S. Kino, “Fiber-optic gyroscope using an air-core photonic-bandgap fiber,” 17th International conference on Optical Fiber Sensors, 5855, 198-201 (2005)

[83] H. K. Kim, M. J. F. Digonnet, and G. S. Kino, “Air-core photonic-bandgap fiber-optic Gyroscope,” J. Lightwave Technol. 24, 3169-3174 (2006)

[84] M. Pang and W. Jin, “Detection of acoustic pressure with hollow-core photonic bandgap fiber,” Opt. Express, 17, 11088 (2009)

[85] Lorna J. Gibson and Michael F. Ashby, Cellular solids: structure and properties, second edition, (1997)

[86] R. M. Christensen, “Mechanics of cellular and other low-density materials,” Int. J. of Solids and Struct. 37, 93-104 (2000)

[87] V. Dangui, H. K. Kim, Michel J. F. Digonnet, and Gordon S. Kino, “Phase sensitivity to temperature of the fundamental mode in air-guiding photonic-bandgap fibers,” Opt. Express, 13, 6669-6684 (2005)

[88] S. P. Timoshenko and J. Goodier, Theory of Elasticity, McGraw-Hill, New York (1970)

[89] Crystal Fiber website, http://www.nktphotonics.com/

[90] K. Saitoh, “Air-core photonic band-gap fibers: the impact of surface modes”, Opt. Express, 12, 394-400 (2004)

[91] C. D. Butter and G. B. Hocker, “Fiber optics strain gauge”, Appl. Opt. 17, 2867-2869, (1978)

[92] J. D. Shephard, P. J. Roberts, J. D. C. Jones, J. C. Knight, and D. P. Hand, “Measuring Beam Quality of Hollow Core Photonic Crystal Fibers”, IEEE J. of Lightwave Technol. 24, 3761-3769 (2006)

[93] A. Cucnotta, S. Selleri, L. Vincetti, and M. Zoboli, “Holey fiber analysis through the finite element method,” IEEE Photon. Technol. Lett. 14, 1530-1532 (2002)

[94] J. Ju, W. Jin, and M. S. Demokan, “Properties of a Highly Birefringent Photonic Crystal Fiber”, IEEE Photon. Technol. Lett. 15, 1375-1377 (2003)

[95] S. Herstrom, L. G. Nielsen and B. Palsdottir, “Acoustic index of Ge-doped optical fibers”, Opt. Lett. 34, 3689-3691 (2009)

[96] I. P. Kaminow and V. Ramaswamy, “Single-polarization optical fibers: Slad model”, Appl. Phys. Lett. 34(4), 268-270 (1979)

[97] X. Fang and R. O. Claus, “Polarization-independent all-fiber wavelength-division multiplexer based on a Sagnac interferometer”, Opt. Lett. 20, 2146-2148 (1995)

[98] B. Dong, and D. Zhou, “Space division multiplexing high-birefringence-fiber loop mirrors for discriminative measurement of temperature and strain”, Appl. Opt. 48, 3994-3997 (2009)